Extraction d'informations de changement à partir des séries temporelles d'images radar à synthèse d'ouverture

Thu Trang Lê

UNIVERSITÉ GRENOBLE ALPES

THÈSE

Pour obtenir le grade de

DOCTEUR DE L'UNIVERSITÉ GRENOBLE ALPES

Spécialité : **STIC Traitement de l'Information**

Arrêté ministériel : 7 août 2006

Présentée par

Thu Trang LÊ

Thèse dirigée par **Emmanuel TROUVÉ**

et co-encadrée par **Abdourrahmane M. ATTO**

préparée au sein **du laboratoire LISTIC**
et de **l'École Doctorale SISEO**

Extraction d'Informations de changement à partir des Séries Temporelles d'Images Radar à Synthèse d'Ouverture

Change Information Extraction from Synthetic Aperture Radar Image Time Series

Thèse soutenue publiquement le **15, Octobre 2015**,
devant le jury composé de :

M. Christian GERMAIN
Professeur, Université Bordeaux 1, Président
M. Jean-Paul RUDANT
Professeur, Université Paris-Est Marne la Vallée, Rapporteur
M. Laurent FERRO-FAMIL
Professeur, Université de Rennes 1, Rapporteur
Mme. Thuy LE TOAN
Directeur de Recherche, Centre d'Études Spatiales de la Biosphère (CESBIO), Examinatrice
M. Loïc DENIS
Maître de Conférences, Université de Saint-Étienne, Examinateur
M. Emmanuel TROUVÉ
Professeur, Université Savoie Mont Blanc, Directeur de thèse
M. Abdourrahmane M. ATTO
Maître de Conférences, Université Savoie Mont Blanc, Co-Encadrant de thèse

Acknowledgments

I am grateful to all those who have helped and inspired me during my PhD research activities.

First of all, I would like to express my deep gratitude and sincere thanks to my two supervisors Emmanuel and Abdou. Their continuous mentorship, suggestions, patience and encouragement helped me to progress and complete my works. From them, I have learned the professional knowledge, the necessary skills to conduct research, from formulating a problem to publishing the results. I thank them for making my PhD experience a very pleasant one.

I would also like to thank the LISTIC laboratory for the warm greeting and the support during my PhD student life here. Special thanks go to Jöelle, Assia, Florent and Jean-Claude for their support.

I wish to thank all members of the dissertation committee for their interest in my work, their time spent on my manuscript and on the thesis defense. Their comments, suggestions, and discussions helped me to improve my knowledge as well as my implemented works. I would like to take this opportunity to particularly thank Prof. Christian Germain for accepting to be the president of the committee, and the two reviewers of my thesis Prof. Jean-Paul Rudant and Prof. Laurent Ferro-Famil for their rigorous readings and precious remarks. I am also grateful to Dr. Thuy Le Toan and Dr. Loïc Denis for their examinations of my thesis and their suggestions.

I would like to acknowledge Dr. Virginie Pinel and Dr. Akhmad Solikhin from ISTerre laboratory for the ALOS-PALSAR dataset they provided and for their collaboration in the interesting issue of Merapi volcano. I would also like to thank Prof. Jean-Marie Nicolas for the excellent quality of the TerraSAR-X dataset used in this thesis that he implemented the coregistration.

I would like to thank the VIED (Vietnam International Education Development - Ministry of Education and Training) for the PhD scholarship award and the LISTIC laboratory - Savoie Mont Blanc University for the supplementary scholarship to support my research.

I also wish to thank my teachers, my colleagues and my friends from the Photogrammetry and Remote Sensing department - Hanoi University of Mining and Geology for their support during my PhD study.

I thank all my friends in LISTIC, with whom I shared my great moments of the PhD student life. I give special thanks to Yajing for sharing her work experience and also her stories with me. Many thanks go to my two office-roommates Bastien and Quentin for their answers to my questions about french culture and language, for our daily discussions and funny conversations... I am also thankful to Liviu, Hakam, Amaury, Nicolas, Ge, Zhangyun, Long, Meriem, Tuan, Mathias..., with whom I had nice memories with bowling, skiing, paragliding and other activities at

Annecy lakeside.

Last, but not least, my wholehearted thanks go to my family: my grandmothers, my parents, my parents-in-law, my sister-in-law, my husband and my little superboy for their everlasting trust, encouragement and unconditional support offered to me on this long journey. Without their support, I would not have completed my works.

Annecy, October 2015,

Thu Trang LÊ

Abstract

A large number of successfully launched and operated Synthetic Aperture Radar (SAR) satellites has regularly provided multitemporal SAR and polarimetric SAR (PolSAR) images with high and very high spatial resolution over immense areas of the Earth surface. SAR system is appropriate for monitoring tasks thanks to the advantage of operating in all-time and all-weather conditions. With multitemporal data, both spatial and temporal information can simultaneously be exploited to improve the results of research works. Change detection of specific features within a certain time interval has to deal with a complex processing of SAR data and the so-called speckle which affects the backscattered signal as multiplicative noise.

The objective of this thesis is to provide a general methodology for simplifying the change analysis of multitemporal SAR data. Such methodology takes advantage of repetitive SAR acquisitions and can be applied to different kinds of SAR data (i.e. single, multipolarization SAR, etc.) for various applications. In this thesis, we first propose a general framework based on a spatio-temporal information matrix called *Change Detection Matrix* (CDM). This matrix reveals temporal neighborhoods which are adaptive to changed and unchanged areas thanks to similarity cross tests. Then, the proposed approach is used to perform three different tasks:

1) multitemporal change detection with different kinds of changes, which allows the combination of multitemporal pair-wise change maps to improve the performance of change detection result;

2) analysis of change dynamics in the observed area, which allows the investigation of temporal evolution of objects of interest;

3) nonlocal temporal filtering of SAR/PolSAR image time series, which allows us to avoid smoothing change information in the time series during the filtering process.

In order to illustrate the relevancy of the proposed approach, the experimental works of this thesis is implemented over two test-sites: Chamonix Mont-Blanc, France and Merapi volcano, Indonesia, with different types of change (i.e., seasonal evolution, glaciers, volcanic eruption, etc.). Observations of these test-sites are performed on four SAR image time series from single polarization to full polarization, from medium to high and very high spatial resolution: Sentinel-1, ALOS-PALSAR, RADARSAT-2 and TerraSAR-X time series.

Keywords:
SAR image time series; Change detection matrix; Multitemporal filtering; Change analysis; Index of change dynamics; Similarity cross test.

Résumé

La réussite du lancement d'un grand nombre des satellites Radar à Synthèse d'Ouverture (RSO - SAR) de nouvelle génération a fourni régulièrement des images SAR et SAR polarimétrique (PolSAR) multitemporelles à haute et très haute résolution spatiale sur de larges régions de la surface de la Terre. Le système SAR est approprié pour des tâches de surveillance continue ou il offre l'avantage d'être indépendant de l'éclairement solaire et de la couverture nuageuse. Avec des données multitemporelles, l'information spatiale et temporelle peut être exploitée simultanément pour rendre plus concise, l'extraction d'information à partir des données. La détection de changement de structures spécifiques dans un certain intervalle de temps nécessite un traitement complexe des données SAR et la présence du chatoiement (speckle) qui affecte la rétrodiffusion comme un bruit multiplicatif.

L'objectif de cette thèse est de fournir une méthodologie générale pour simplifier l'analyse de changement des données multitemporelles SAR. Cette méthodologie permet de bénéficier des avantages d'acquisitions SAR répétitives et de traiter différents types de données SAR (images SAR mono-, multi- composantes, etc.) pour diverses applications. Au cours de cette thèse, nous proposons tout d'abord un cadre méthodologique basée sur une matrice d'information spatio-temporelle appelée *Matrice de détection de changement* (CDM). Cette matrice contient des informations de changements obtenus à partir de tests croisés de similarité sur des voisinages adaptatifs. La méthode proposée est ensuite exploitée pour réaliser trois tâches différentes :

1) la détection de changement multitemporel avec différents types de changements, ce qui permet la combinaison des cartes de changement entre des paires d'images pour améliorer la performance de résultat de détection de changement ;

2) l'analyse de la dynamicité de changement de la zone observée, ce qui permet l'étude de l'évolution temporelle des objets d'intérêt ;

3) le filtrage nonlocal temporel des séries temporelles d'images SAR/PolSAR, ce qui permet d'éviter le lissage des informations de changement dans des séries pendant le processus de filtrage.

Afin d'illustrer la pertinance de la méthode proposée, la partie expérimentale de cette thèse est effectuée sur deux sites d'étude : Chamonix Mont-Blanc, France et le volcan Merapi, Indonésie, avec différents types de changement (i.e. évolution saisonnière, glaciers, éruption volcanique, etc.). Les observations de ces sites d'étude sont réalisées sur quatre séries temporelles d'images SAR monocomposantes et multicomposantes de moyenne à haute et très haute résolution : des séries temporelles d'images Sentinel-1, ALOS-PALSAR, RADARSAT-2 et TerraSAR-X.

Mots clés :
Série temporelle d'images SAR ; Matrice de détection de changement ; Filtrage multitemporel; Analyse de changement ; Indice de dynamicité de changement ; Test croisé de similarité.

Acronyms and Notations

Acronyms

ALOS: Advanced Land Observing Satellite
BNL: Bayesian NonLocal
BPT: Binary Partition Tree
BRISQUE: Blind/Referenceless Image Spatial Quality Evaluator
CFAR: Constant False Alarm Rate
DCT: Discrete Cosine Transform
DEM: Digital Elevation Model
DSM: Discriminative Similarity Measure
CDM: Change Detection Matrix
CDMF: CDM-based Filter
CSA: Canadian Space Agency
CV: Coefficient of Variation
DLR: German Aerospace Center
DWT: Discrete Wavelet Transform
EFIDIR : Extraction et Fusion d'Informations pour la mesure de Déplacements par Imagerie Radar
ENL: Equivalent Number of Look
ENVISAT : ENVIronement SATellite
ERS-1/2 : European Remote Sensing - satellites of ESA
ESA: European Space Agency
FDCT: Fast Discrete Curvelet Transform
GΓD: Generalized Gamma distribution
GG: Generalized Gaussian
GLR: Generalized Likelihood Ratio
IDAN: Intensity Driven Adaptive Neighborhood
InSAR: Interferometric Synthetic Aperture Radar
JERS : Japan and Earth Observation Systems
KI: Kittler-Illingworth
KL: Kullback-Leibler
KLD: Kullback-Leibler Distance
LLMMSE: Locally Linear Minimum Mean Square Error
LOS: Line Of Sight
MAP: Maximum A Posteriori
MDA: MacDonald Dettwiler Associates Ltd.
MDDM: Multi-Date Divergence Matrix
MLE: Maximum-Likelihood Estimation
MMSE: Minimum Mean Square Error
MoLC: Method of Log-Cumulant

MoM: Method of Moments
NASDA: National Space Development Agency of Japan
PALSAR: Phased Array L-band Synthetic Aperture Radar
PDF: Probability Density Function
PPB: Probabilistic Patch-Based
Pol-InSAR: Polarimetric Interferometric Synthetic Aperture Radar
PolSAR: Polarimetric Synthetic Aperture Radar
PWF: Polarimetric Whitening Filter
QF: Quegan's Filter
RADARSAT-1, -2: Canadian Earth observation satellites
RAR: Real Aperture Radar
RCS: Radar Cross-Section
SAR: Synthetic Aperture Radar
SAR ITS: SAR Image Time Series
SCM: Sample Covariance Matrix
Sentinel-1: Constellation of two satellites for Land and Ocean monitoring
SIRV: Spherically Invariant Random Vector
SLAR: Side-Looking Airborne Radar
SLC: Single Look Complex
SWT: Stationary Wavelet Transform
TerraSAR-X : German Earth observation satellite
WD: Wishart distance
WMLE: Weighted Maximum Likelihood Estimator

Notations

C: Covariance matrix of SAR data
C_{pq}: Element pq of C
$C_{pq}^{\mathcal{W}[J,\varepsilon]}$: a wavelet coefficient of C_{pq}
$C^{\mathcal{W}}$: SWT decomposed covariance matrix
$\langle \mathcal{C}^{\mathcal{W}} \rangle_t$: SWT decomposed SCM of image $\mathcal{I}_t$
$\mathcal{CM}_{t,\ell}$: Change map between date t and date ℓ
$\mathcal{CM}_t^{(d)}$: d-length change map corresponding to the reference date t
$\mathfrak{D}$: Similarity measure
$\dagger$: The complex conjugate transpose
$\ddagger$: Vectorization of a matrix
$\mathcal{I}$: A SAR image time series
$\mathcal{I}_t$: Image acquired at time t
$\mathcal{I}_t(i,j)$: Pixel (i,j) on image $\mathcal{I}_t$
$\mathcal{I}_t^w(i,j)$: Spatial neighborhood of $\mathcal{I}_t(i,j)$
$\{\mathcal{I}_t(i,j)\}_{1 \leqslant t \leqslant N}$: Pixel pile
$\hat{I}_t$: Filtered image $\mathcal{I}_t$
k_l: Lexicographic target vector

k_p: Pauli target vector
$K^w_{t,\ell}(i,j)$: Similarity degree between $\mathcal{I}_t(i,j)$ and $\mathcal{I}_\ell(i,j)$.
$\hat{K}^w_{t,\ell}(i,j)$: Similarity degree between $\Psi\left(\mathcal{I}^w_t(i,j)\right)$ and $\Psi\left(\mathcal{I}^w_\ell(i,j)\right)$
L: Number of looks
λ: Threshold value for similarity test
M: Step 1 Change Detection Matrix (CDM 1)
$\hat{M}$: Step 2 Change Detection Matrix (CDM 2)
N: Number of images in the time series $\mathcal{I}$
N_c: Number of columns of image $\mathcal{I}_t$
N_l: Number of lines of image $\mathcal{I}_t$
$N_{\Psi_t(i,j)}$: Number of elements in $\Psi\left(\mathcal{I}_t(i,j)\right)$
$\Psi\left(\mathcal{I}^w_t(i,j)\right)$: Temporal neighborhood of pixel $\mathcal{I}_t(i,j)$
$\rho(i,j)$: Index of change dynamics of pixel pile $\{\mathcal{I}_t(i,j)\}_{1\leqslant t\leqslant N}$
ρ_1: Index of change dynamics after the Median filtering
ρ_2: Index of change dynamics after the Mod filtering
S_{HH}, S_{VV}: Scattering elements of co-polarization
S_{HV}: Scattering element of cross-polarization
Σ: the complex covariance (C) or coherency (T) matrix
T: Coherency matrix of SAR data
$\varrho(i,j)$: The speckle-free image
$\mathcal{W}[J,\varepsilon]$: Operator computes the stationary wavelet decomposition at levels $J \in \{1,2,3\}$ into four coefficients $\varepsilon \in \{a,h,v,d\}$
Z: L-look complex covariance/coherency matrix

Contents

List of Figures

List of Tables

Chapter 1

Introduction

Contents

1.1 Context and motivation

The success of launching Synthetic Aperture Radar (SAR) satellites since the late 1970's has provided an interesting tool to regularly map the Earth's surface and acquire information about its physical properties. SAR is an active microwave imaging method, which operates in all-time and all-weather conditions, hence constituting a significant advantage over traditional optical imaging techniques. Consequently, these systems are appropriate for operational monitoring tasks. Nowadays, spaceborne SAR systems are able to provide long time series of high quality SAR images over immense portions of the Earth's surface. Many applications employing information of SAR image time series have been addressed in the literature such as land cover classification, crop mapping and monitoring, natural feature mapping and analysis: forest, wet snow cover, glacier motion, natural disaster monitoring like flood, tsunami damage, etc.

At the early 1990s, the launch of the first generation satellites ensured the availability of SAR and interferometric SAR (InSAR), i.e., ERS-1 in 1991 and ERS-2 in 1995 of the European Space Agency (ESA), JERS in 1992 of the National Space Development Agency of Japan (NASDA), and RADARSAT-1 in 1995 of the Canadian Space Agency (CSA), then ENVISAT (ESA) later in 2002. The use of polarimetric SAR (PolSAR) imagery has been studied increasingly and extensively since the launch of new generation SAR satellites. These sensors such as ALOS in 2006 (NASDA), RADASAT-2 (CSA) and TerraSAR-X of the German aerospace center (DLR) in 2007, in L-band, C-band and X-band, respectively, offer both dual and full polarization. The polarimetry (PolSAR) exploits different polarimetric configurations to measure the electromagnetic field backscattered by the ground surface in order to characterize the information related to the nature of the interaction between the radar wave and the backscattering. Then the combination of the two techniques, InSAR and PolSAR, generates the multivariate imagery of polarimetric and interferometric SAR (POL-InSAR). These data offer both the advantages of

interferometry and polarimetry. Along with the incessant development of applied sciences and sensor technologies, future generation SAR satellites are expected to continue to provide SAR imagery with higher quality, enhanced spatial and temporal resolutions, multiple frequency and polarization images, etc.

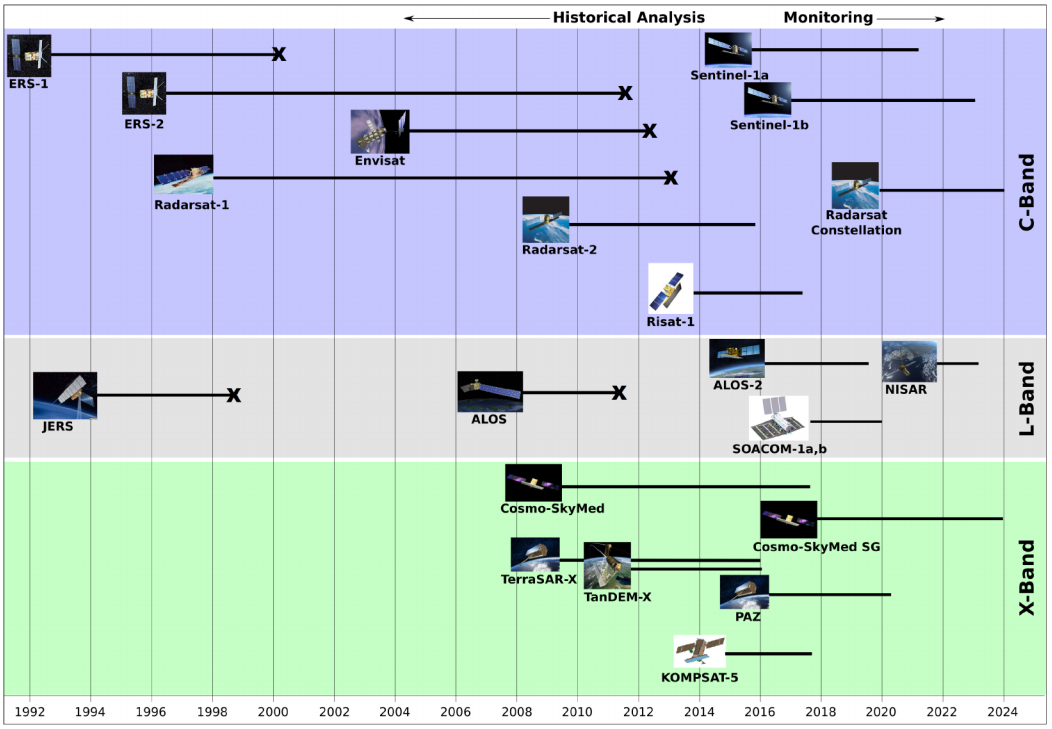

Figure 1.1: Most common past, present and future SAR satellite missions (©UNAVCO).

The current available SAR sensors offer different imaging modes with different characteristics. With the ScanSAR mode (RADARSAT-2, TerraSAR-X, Sentinel-1), acquired data can cover over very large areas possible (up to 400 x 400 km), however, the spatial resolution is decreased and making it complex in handling and processing the data. On the contrary, the Spotlight acquisition mode (TerraSAR-X, Cosmo-Skymed, RADARSAT-2) offers data at less than 1 m resolution and 10 km coverage. These sensors also frequently produce images over a scene with short repeat cycles, for instance, 11 days for TerraSAR-X images and even 6 days for the constellation of Sentinel-1A (launched in 2014) together with Sentinel-1B (to be launched in 2016). SAR imagery can meet the need of monitoring the Earth's surface from a large scale (tectonics, earthquakes, glaciers motion, etc.) to a fine scale that requires high resolution data (for instance, in pure urban applications where the density and the complexity of single targets are very high). In general, analysts have to address the problem that the SAR image database is diverse and large-dimensional:

- in terms of acquisition systems, such as amplitude/intensity SAR, InSAR, PolSAR, Pol-InSAR, multifrequencies X-, C-, L- bands, etc.,
- in terms of the acquisition conditions, such as ascending and descending orbits, different viewing angles, etc.,
- in addition, each image in the database is with large sample size.

The large amount of such data makes information processing complicated.

In this context, how to exploit effectively the large information provided by SAR image to benefit from the advantages of these data is an attractive question for analysts. In this thesis, we are interested in the use of multitemporal SAR images in order to extract both spatial and temporal change information provided by these data. We focus on the development of processing methods (change detection, multitemporal filtering) and the analysis of multitemporal changes occurring in SAR/PolSAR image time series.

1.2 Thesis outline

The thesis is organized as follows. In Chapter 2, we review the principles of SAR imagery, including an introduction of the main concepts of the formation, the geometric distortion and speckle statistics of SAR and PolSAR images. We also present the results of tests performed to assess the statistical model fit of some given distributions (Gamma, Rayleigh, Nakagami, Log-normal and Weibull distributions) to SAR data (TerraSAR-X, Sentinel-1, ERS-1 data).

Chapter 3 presents an overview of the previous works on SAR image filtering and change detection. The chapter recalls filtering approaches for both spatial and multitemporal filters for SAR and PolSAR data as well as change detection techniques and similarity measures between multitemporal images.

Chapter 4 introduces the study areas and datasets used in the experimental works. The two test-sites: Chamonix Mont-Blanc, France and Merapi volcano, Indonesia, with different types of change are observed by four datasets: 25 images of HH TerraSAR-X, 7 images of quad-pol RADARSAT-2, 11 image of VV and dual-pol Sentinel-1 and 11 images of dual-pol ALOS-PALSAR. Some preprocessing steps executed before extracting information from these data are also presented.

Chapter 5 is dedicated to the problem of exploiting multitemporal SAR images and presents the framework proposed to build *change detection matrix* (CDM) for SAR image time series' analysis. The chapter presents the original two step strategy, the implementation of the proposed approach and then analyzes its properties and potentials in multitemporal change detection and other applications.

In Chapter 6, we propose two approaches for the change analysis of SAR image time series:

1) the combination of multitemporal pair-wise change maps to improve the performance of change detection result,

2) an index of change dynamics for the investigation of temporal evolution over the observed areas.

Chapter 7 addresses the problem of multitemporal filtering of SAR images. In this chapter, we describe how the proposed change detection matrix provides temporal samples for the nonlocal temporal filtering process of both single- and multi-polarization SAR images.

Finally, the conclusions and perspectives are drawn in Chapter 8.

Chapter 2

Synthetic aperture radar imaging

Contents

A SAR system coherently transmits and receives electromagnetic signals. For every sample of SAR data, amplitude and phase of the echo signal is represented in a complex value consisting of a real (in-phase) and imaginary (quadrature) part. The purpose of this chapter is to introduce the basic properties of remote sensing SAR imagery. The details of SAR and polarimetric SAR (PolSAR) can be found in [Oliver & Quegan 2004], [Elachi & vanZyl 2006], [Massonnet & Souyris 2008], [Lee & Pottier 2009], etc. The principles of SAR geometry, the formation of the complex image and statistical models commonly used for single polarization as well as multipolarization SAR images are described below.

2.1 Principles of SAR

SAR is an active microwave, coherent imaging system operating independently of the Sun illumination and cloud coverage. This system is carried on a moving platform and has side-looking at the ground. SAR remote sensing uses microwave portion of the electromagnetic spectrum, from a frequency of 0.3 GHz to 300 GHz, between P and Ka band (Table 2.1) with different penetration capabilities. As an active imaging sensor, SAR system transmits successive pulses of radio waves to illuminate a target scene and then receives and records the echo of each transmitted pulse. The recorded backscattered electromagnetic signal after demodulation is called raw data. To obtain SAR image, raw data need to be handled by a complex processing

which allows us to coherently combine all recordings associated with the same target received from the multiple antenna locations.

Table 2.1: Frequency and wavelength of SAR remote sensing bands.

Band	Wavelength (cm)	Frequency (GHz)	Characteristics
Ka	0.75 - 1.1	40 - 26.5	Used mainly for military purposes in canopy top layer, surface, or high resolution target applications
K	1.1 - 1.67	26.5 - 18	
Ku	1.67 - 2.4	18 - 12.5	
X	2.4 - 3.75	12.5 - 8	High resolution monitoring capabilities
C	3.75 - 7.5	8 - 4	Penetration capability of vegetation or solids is restricted to the top layer. Useful for sea-ice surveillance.
S	7.5 - 15	4 - 2	Used for medium-range meteorological applications (rainfall measurement, airport surveillance)[HandBooks].
L	15 - 30	2 - 1	Capable of penetrating vegetation, forests. Useful for monitoring vegetated surfaces, ice sheet, glacier dynamics.
P	30 - 100	1 - 0.3	Significant penetrations capabilities relating vegetation canopy, sea ice, soil, glaciers. Useful for biomass estimation.

2.1.1 SAR image formation

The configuration of an imaging radar system is described in Fig. 2.1. At position t_1, the antenna beam first illuminates the target through a beam width under a look angle (or off-nadir angle) θ. It continues moving for a distance L_S until the last illumination of this target at the position t_n. L_S is the synthetic aperture length, also called the integration length.

The ground is mapped on SAR image in a coordinate system composed of the azimuth axis (the trajectory direction) and the range axis (wave propagation direction). When moving on the trajectory direction, the antenna beam scans an area on the ground called swath. The swath width [Elachi & vanZyl 2006] is:

$$W \simeq R\Psi = \frac{\lambda h}{L_R \cos^2\theta_c} \tag{2.1}$$

where R is the slant range, h is the antenna altitude, L_R is the antenna width and Ψ is the beam width in range direction, and θ_c is the off-nadir angle of middle range.

The time difference between the transmitted pulse and the received echo of a scatter target allows the determination of the distance between the antenna and the target (slant range R). The spatial resolution is the minimum distance enabling to distinguish two scatter points. In SAR image plane, the spatial resolution of a pixel

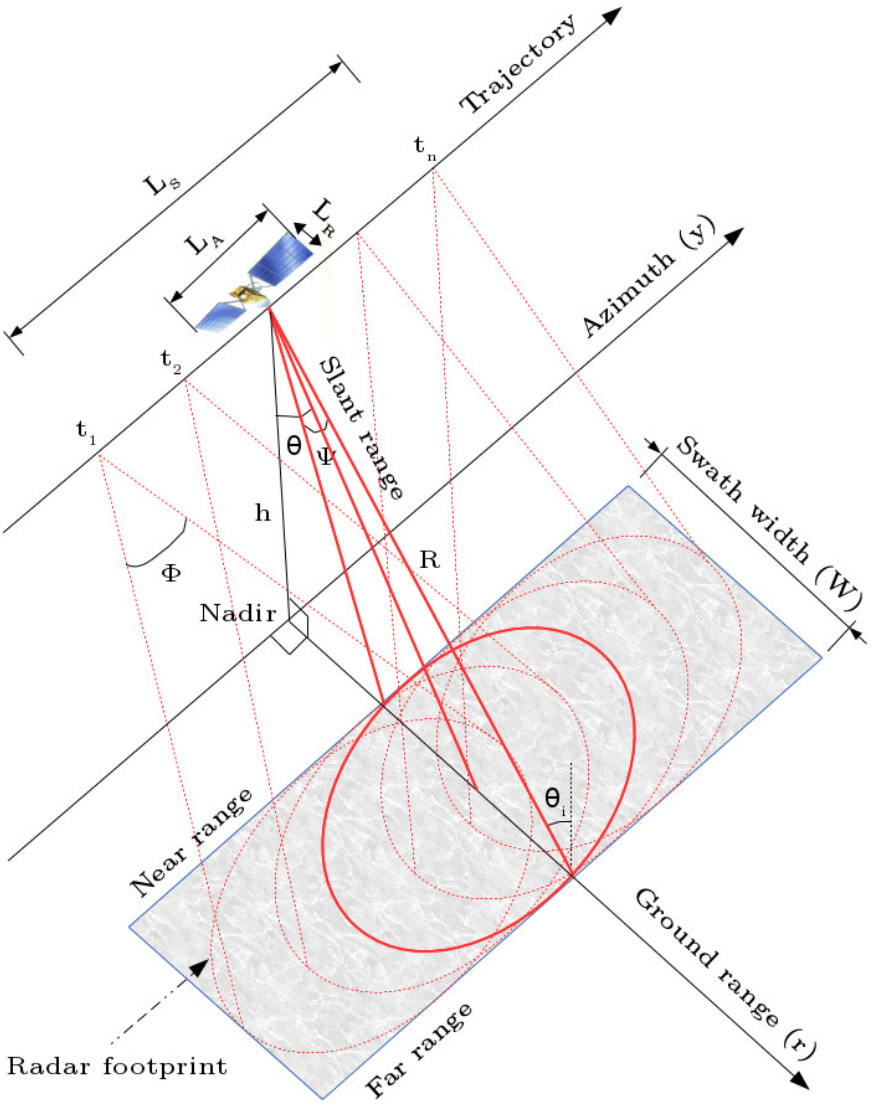

Figure 2.1: SAR acquisition.

is defined on both range and azimuth directions.

2.1.1.1 Range resolution

The slant range resolution of the raw data is a function of the pulse duration and the wave propagation velocity (c):

$$\delta_{sr_{raw}} = \frac{\tau c}{2}. \tag{2.2}$$

From Eqs. (2.2), we can see that, a short pulse duration is necessary to obtain a high range resolution. However, Signal-to-Noise Ratio (SNR) is proportional to the

pulse duration, therefore the reduced pulse length results in a low SNR. To solve this problem, radar systems transmit a linear frequency modulated pulse called chirp which enables a high energy signal to be transmitted with a long enough duration. The transmitted signal is:

$$s_e(t) = e^{j2\pi\left(f_c t + \frac{Pt^2}{2}\right)} \quad \text{with} \quad \mid t \mid < \frac{\tau}{2}. \tag{2.3}$$

where f_c is the radar carrier frequency of the chirp with a modulation rate P.
The received signal is then correlated with the emitted pulse in the so-called "range compression" step (matched filtering), resulting in the following range focused signal:

$$s_r\left(t - \frac{2}{c}R\right) \approx \tau \text{sinc}\left(P\tau\left(t - \frac{2}{c}R\right)\right) e^{j2\pi\left(f_c(t-2R/c) + \frac{P(t-2R/c)^2}{2}\right)}, \tag{2.4}$$

where $\text{sinc}(u) = \frac{\sin(u)}{u}$.
With this technique, the slant range resolution is gained thanks to the bandwidth B:

$$\delta_{sr} \approx \frac{c}{2P\tau} = \frac{c}{2B}. \tag{2.5}$$

Both Side-Looking Airborne Radar (SLAR) or Real Aperture Radar (RAR) and SAR achieve their range resolution in this way [McCandless & Jackson 2004].

The ground range resolution representing the projection of the pulse on the surface with the incidence angle (θ_i) can be defined from the slant range resolution as:

$$\delta_{gr} = \frac{c}{2B\sin\theta_i}. \tag{2.6}$$

2.1.1.2 Azimuth resolution

The RAR azimuth resolution or RAR cross-range resolution is defined as:

$$\delta_{a_{RAR}} = R\Phi = R\frac{\lambda}{L_A} \tag{2.7}$$

where Φ is the beam width in azimuth direction, λ is the radar wavelength and L_A is the antenna length.

In spaceborne radar, the RAR range resolution issue can be solved as mentioned above but the RAR azimuth resolution is very low (several km). According to Eq. (2.7), in order to derive a high azimuth resolution, the antenna length is required to be large (100 m up to certain km) or the aperture size is increased. Rather than manufacturing and launching such a too large instrument, synthetic aperture radar is used to improve azimuth resolution. Due to the sensor motion, the apparent "Doppler bandwidth" [Wiley 1954] of the received signal can be used instead of reducing radar's antenna beam width on azimuth direction [McCandless 1989]. Indeed, when moving from t_1 to t_n on synthetic aperture length (integration length) (Fig. 2.1), the antenna receives n radar echoes in the response of a scatterer. There-

fore, a given scatter point on the ground is illuminated by a series of pulses from different positions of the antenna along the satellite trajectory. The distance R in Eq. (2.4) varies, creating a frequency modulation which is used to focus the image in azimuth direction. The integration length $L_S = R\Phi = R\frac{\lambda}{L_A}$ can be seen as the length of a large synthetic antenna that has the synthetic beam width $\Phi_S = \frac{\lambda}{2L_S}$. Then, the SAR azimuth resolution is:

$$\delta_{a_{SAR}} \approx R\Phi_S \approx R\frac{\lambda}{2L_S} \approx \frac{L_A}{2} \tag{2.8}$$

Eq. (2.8) explains why a SAR satellite with a small size of antenna operating at a very high altitude (long slant range) can provide high azimuth resolution images.

2.1.2 SAR geometric distortion

The SAR image formation process induces a very different observation geometry of scenes compared to optical sensors. Geometric distortions of SAR data in range direction are large and even more important at regions where the altitude strongly varies while they are much smaller in azimuth direction. Fig. 2.2 shows the main geometric effects (foreshortening, layover and shadowing) when the ground is imaged on the image plane (containing the trajectory direction of the antenna and the line of sight (LOS) direction), so-called slant range - azimuth plane.

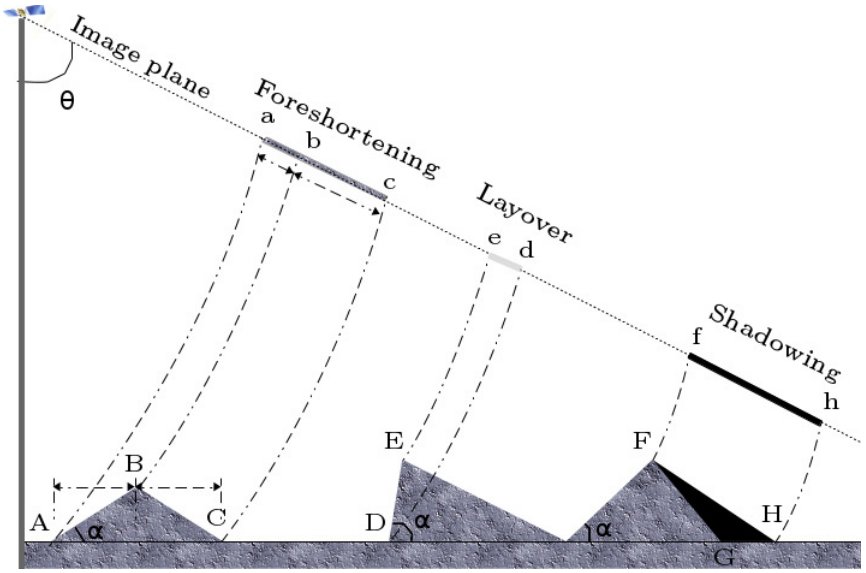

Figure 2.2: SAR geometric distortions: foreshortening, layover and shadowing effects.

At regions with high relief, mountain slopes facing the SAR (foreslopes) are shortened on the image plane. This distorted appearance on SAR image is called foreshortening effect which compresses the slopes on the facing side (facing radar

incoming beam) of the mountain. In Fig. 2.2, points on the ground have their corresponding imaged points on the image plane. On the ground, the distance A-B equals to the distance B-C but on image plane, a-b (foreslope) is smaller than b-c. This makes the top of the mountain (b) tilts toward the platform [Bamler 2000]. The steeper the terrains or the smaller the look angles (θ), the worse the foreshortening effects.

If the terrain slope angle (α) becomes bigger than the look angle (θ), scatter points are imaged in reverse order. This phenomenon is called layover (foldover) effect, it is an extreme case of foreshortening. In Fig. 2.2, the beam reaches the top E of the mountain before it reaches the bottom D, the antenna thus receives the echo of E before the one of D. Therefore, the segment D-E on the ground is imaged reversely on the image plane as e-d.

At the backfacing side of the mountain, if the backslope is stronger than the LOS, SAR will not be able to reach this area due to the side-looking configuration. There is no returned echo from this ground area and it leads to a black zone on SAR image like shadow, and this phenomenon is called shadowing effect. In Fig. 2.2, the region F-G-H is the unreachable region of the radar beam.

2.1.3 Speckle properties

A scatterer can be characterized by the Radar Cross-Section (RCS) σ or the backscattering coefficient ("sigma-nought") σ^0. RCS is the cross-sectional area with units of m^2 of an equivalent sphere that ideally reflects all the incident radar energy on the target. The backscattering coefficient is the normalized RCS of all scatterers considered to have a constant phase in a unit area [Le-Toan 2007].

The response of a single point scatterer is defined by a complex value $s_a(r', y')$ [Bamler & Hartl 1998]:

$$a(r', y') = \sqrt{\sigma}\delta(r - r', y - y')e^{j\phi_{scat}}, \tag{2.9}$$

where (r', y') is the scatterer position in range and azimuth, ϕ_{scat} is the phase shift introduced by the scattering mechanism and $\delta(r, y)$ is the 2D Dirac function.

According to the SAR processing recalled in Section 2.1.1, the 2D range and azimuth impulse response function is given by:

$$h(r, y) = \text{sinc}\left(\frac{2Br}{c}\right)\text{sinc}\left(\frac{2y}{L_S}\right) = \text{sinc}\left(\frac{r}{\delta_{sr}}\right)\text{sinc}\left(\frac{y}{\delta_{a_{SAR}}}\right) \tag{2.10}$$

From (2.9) and (2.10), the focused response of the scatterer is:

$$s(r, y) = \sqrt{\sigma}e^{j(\frac{4\pi}{\lambda}(r-r')+\phi_{scat})}\text{sinc}\left(\frac{r - r'}{\delta_{sr}}\right)\text{sinc}\left(\frac{y - y'}{\delta_{a_{SAR}}}\right) \tag{2.11}$$

The response of a resolution cell containing a large number of point scatterers is the result of the multiple backscattering combination which can be represented as a distributed scatterer. The physical and geometrical properties of a distributed scat-

terer of the scene results in a random behavior of the backscattered signal. Under the assumption of linearity of the scene, the SAR imaging process is a geometric projection of distributed scatterers from 3D space into the 2D cylindrical zero-Doppler radar coordinates (r, y) followed by a 2D convolution with the point response in (2.10) [Bamler & Hartl 1998]:

$$s(r,y) = \iint a(r',y')e^{-j2lr'}h(r-r',y-y')\mathrm{d}r'\mathrm{d}y' \tag{2.12}$$

with $l = 2\pi/\lambda$, the wavenumber.

Speckle refers to a noise-like characteristic involved in all coherent systems. The response of a resolution cell is the sum of n responses of random scatterers distributed in the cell. This summation can create either high or low amplitude, depending on random constructive or destructive interference (Fig. 2.3).

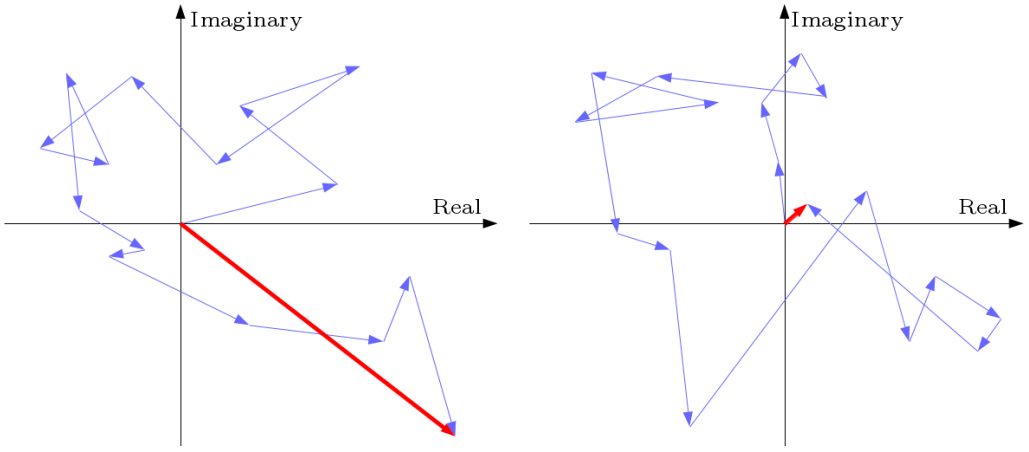

(a) Constructive speckle (b) Destructive speckle

Figure 2.3: Speckle formation: coherent integration of many scatterer responses in a resolution cell.

Given $s_i = \varrho_i e^{j\varphi_i}$ the response of the target i, the response of the cell is:

$$\mathcal{S} = I_p + jQ = \sum_{i=1}^{n} \varrho_i e^{j\varphi_i}; \qquad j = \sqrt{-1} \tag{2.13}$$

where, I_p is in-phase and Q is quadrature, and the magnitude ϱ and the phase φ are independent random variables. $\mathcal{S}$ is the single look complex image. In single channel SAR image, the useful information is the amplitude or intensity/power while the phase is not exploited.

According to the central limit theorem, under the assumption that ϱ and φ are independent random variables, phases are uniformly distributed in $[0, 2\pi]$ and the number of target points in the cell is quite large. The real and imaginary parts of

complex data $\mathcal{S}$ form complex circular Gaussian centered vectors of the variance σ^2 proportional to the backscattering coefficient σ_0 [Leberl 1990]. Consequently, the real and imaginary parts are independent, zero-mean Gaussian random variables and the amplitude $A = |\mathcal{S}| = \sqrt{I_p^2 + Q^2}$ follows a Rayleigh distribution with a parameter $\nu = 2\sigma$:

$$P_A(x) = \frac{2x}{\nu}\exp\left(\frac{-x^2}{\nu}\right) \tag{2.14}$$

with the mean $\mu_A = \pi\sqrt{\nu}/2$ and the standard deviation proportional to $\sigma_A = \sqrt{4/\pi - 1}\mu_A$.

The intensity or power $I = A^2$ has an exponential distribution:

$$P_I(x) = \frac{1}{\nu}\exp\left(\frac{-x}{\nu}\right) \tag{2.15}$$

for which the 1st and 2nd moments are: $\mu_I = \sigma_I = \nu$.

With L-look intensity data, the probability density of I becomes a Gamma law:

$$P_{I_L}(x) = \frac{L^L x^{L-1}}{\nu^L \Gamma(L)}\exp\left(-\frac{Lx}{\nu}\right) \tag{2.16}$$

The coefficient of variation $CV = \sigma_{I_L}/\mu_{I_L}$ equals 1 for the single look images and equals $1/\sqrt{L}$ for L-look images. This parameter may be estimated directly on the image and provides also an important local measure of speckle.

The corresponding L-look amplitude $A_L = \sqrt{I_L}$ follows the Nakagami distribution [Tison *et al.* 2004]

$$P_{A_L}(x) = \frac{2L^L x^{2L-1}}{\nu^L \Gamma(L)}\exp\left(-\frac{Lx}{\nu}\right) \tag{2.17}$$

with mean and variance proportional to $\sigma_{A_L} = \sqrt{(4/\pi - 1)/L}\mu_{A_L}$.

The proportionality between the mean and the variance of the amplitude or intensity allows to describe the speckle as a multiplicative noise (the fluctuations are even more important with the strong radiometry) fully developed [Goodman 1976] when:

- the number of scatterers is large ($n \gg 5$), and the responses of each scatterer are independent of the others,
- the amplitude and the phase are decorrelated,
- the probability density function (PDF) of the amplitude is unchanged,
- and the phase has a uniform distribution.

The assumption of the central limit theorem is not always obeyed for real SAR data. It only can be locally applied in stationary zones like fields, meadows, etc. When one of these above conditions cannot be guaranteed or the underlying grounds

are non-stationary, the distributions previously described are not valid, and other distributions should be considered for speckle modeling. For this issue, two approaches are generally used, i. e. texture approach and empirical approach [Tison *et al.* 2004].

The texture approach considers that the intensity I is represented by a multiplicative model including two random variables, one for the presence of texture of the ground z and the other expresses the speckle s:

$$I = z.s \tag{2.18}$$

The random variable z follows certain distributions:

- $z = \nu$ (constant), this case is strictly validated for homogeneous regions, no texture of an image characterized by fully developed speckle, the intensity I then follows a Gamma distribution of mean ν (see above) [Nicolas 2002].

- z follows a Gamma distribution, the intensity I is $\mathcal{K}-$distributed. This distribution corresponding to a "birth-death-migration" process [Oliver 1984] of the variation of the scatterer number within a resolution cell. This distribution is well adapted to vegetation areas.

$$P_I(x) = \frac{1}{\Gamma(L)\Gamma(\alpha)} \frac{2L\alpha}{\mu} \left(\frac{L\alpha}{\mu} x\right)^{\frac{\alpha+L}{2}-1} K_{\alpha-L}\left(2\sqrt{\frac{L\alpha}{\mu} x}\right); \quad \alpha > 0 \tag{2.19}$$

  where α is the shape parameter, and $K_{\alpha-L}$ is the second-kind modified Bessel function.

- z follows an Inverse Gamma distribution, the intensity I then follows a Fisher distribution:

$$P_I(x) = \frac{\Gamma(L+\alpha)}{\Gamma(L)\Gamma(\alpha)} \frac{L}{\alpha\mu} \frac{\left(\frac{Lx}{\alpha\mu}\right)^{L-1}}{\left(1+\frac{Lx}{\alpha\mu}\right)^{L+\alpha}}; \quad \alpha > 0 \tag{2.20}$$

  This distribution has a general characteristic that is suitable for modeling urban areas.

The empirical approach considers that speckle is not fully developed and distribution functions are empirically defined. Several models have been proposed such as:

- Log-normal distribution:

$$P_X(x) = \frac{1}{x\sqrt{2\pi\mu}} \exp\left(-\frac{(\ln x - \sigma^2)^2}{2\mu}\right), \tag{2.21}$$

X can be either amplitude (A) or intensity (I) images and this distribution is dedicated to very heterogeneous areas.

- Weibull distribution:

$$P_X(x) = \frac{\alpha x^{\alpha-1}}{\kappa^\alpha} \exp\left[-\left(\frac{x}{\kappa}\right)^\alpha\right], \tag{2.22}$$

with α and κ representing a shape parameter and a scaling parameter. This distribution can well model single look data but not precisely multilook data, it is and suitable for low heterogeneous areas.

- Generalized Gamma distribution (GΓD) [Li *et al.* 2011]:

$$P_X(x) = \frac{\mid \eta \mid \alpha^\alpha}{\kappa\Gamma(\alpha)} \left(\frac{x}{\kappa}\right)^{\alpha\eta-1} \exp\left(-\alpha\left(\frac{x}{\kappa}\right)^\eta\right); \quad x \in \mathbb{R}^+ \tag{2.23}$$

with η, a power parameter. GΓD is a general case which contains a large number of other distributions, in particular, including the well-known distributions, e.g., Rayleigh ($\eta = 2, \alpha = 1$), Exponential ($\eta = 1, \alpha = 1$), Gamma ($\eta = 1$), Nakagami ($\eta = 1$), Log-normal ($\alpha \to \infty$), and Weibull ($\alpha = 1$) distributions.

2.1.4 Examples of speckle SAR statistical model fit

Many approaches for detection, classification, segmentation, etc., from SAR data are based on statistical models. Therefore, the selection of an appropriate speckle model which can highly fit the real SAR data is essential. In this section, we illustrate the fit of several standard probabilistic distributions usually used for modeling SAR data (i.e., Rayleigh, Gamma, Nakagami) and the Log-normal and Weibull distributions to three examples of SAR amplitude data: ERS 1 (3 looks), TerraSAR X (single look) and Sentinel-1 (single look) images.

For this purpose, each image is divided into subimages, then parameters of given distributions are estimated by Maximum-Likelihood estimation (MLE) for each subimage. The major rules for assessing the fitting accuracy includes the χ^2 matching test [Plackett 1983], Akaike Information Criteria (AIC) rule [Akaike 1974], Kolmogorov-Smirnov (KS) test [Justel *et al.* 1997], D'Agostino-Pearson test [Pearson 1931], Kuiper test [Kuiper 1960], etc. Among these tests, the χ^2 test is an approximate test based on the number of random observations in each category. It effectively tests whether the histogram of sample data is reasonable under the assumed distribution [DeVore & O'Sullivan 2001]. In our experimental work, the fit quality of given probabilistic distributions to SAR data is quantitatively evaluated by the χ^2 test[1].

[1]The details of χ^2 test is given in the appendix A

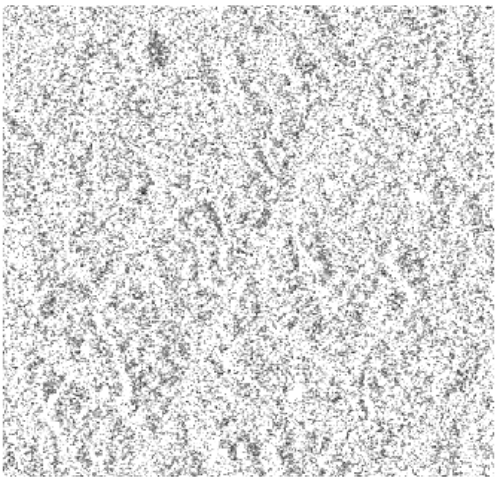

(a) Subimage n^o 6

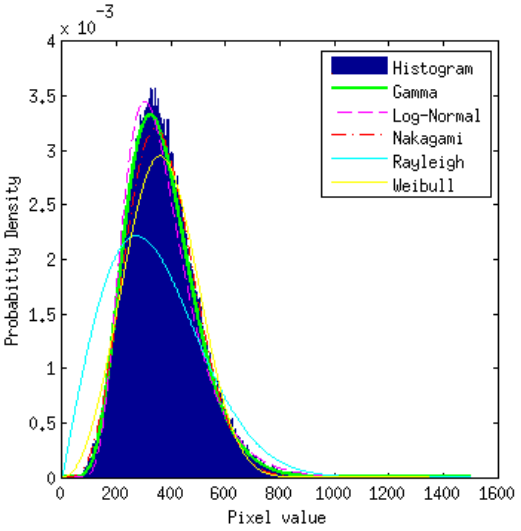

(b) Histogram fitting PDFs of subimage n^o 6

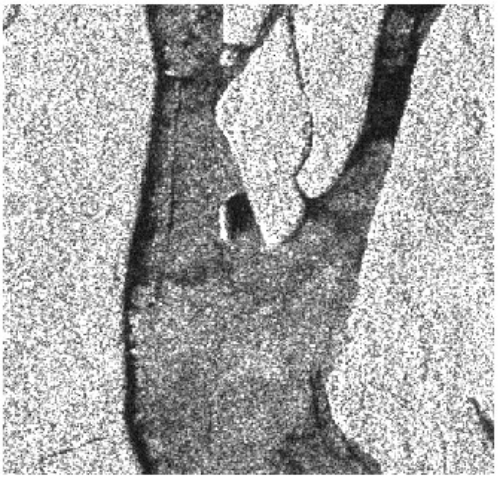

(c) Subimage n^o 22

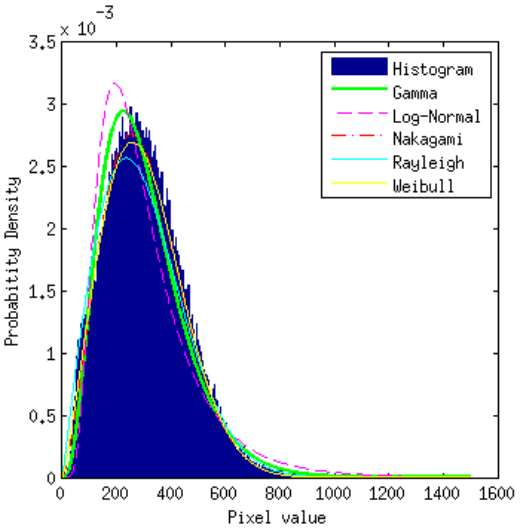

(d) Histogram fitting PDFs of subimage n^o 22

Figure 2.4: The fit of several PDFs to the histogram of ERS 1 image.

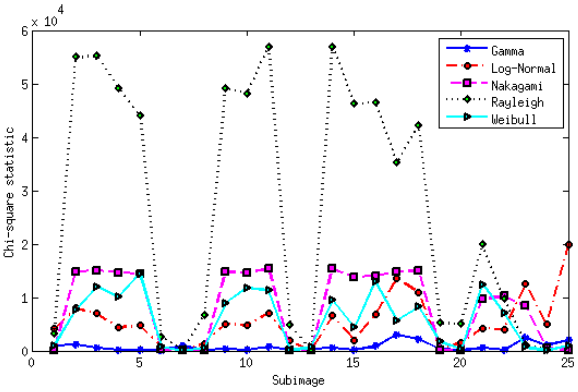

(a) χ^2 test of ERS 1 image

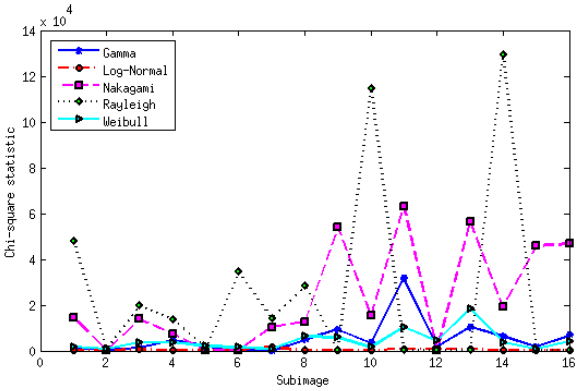

(b) χ^2 test of TerraSAR-X image

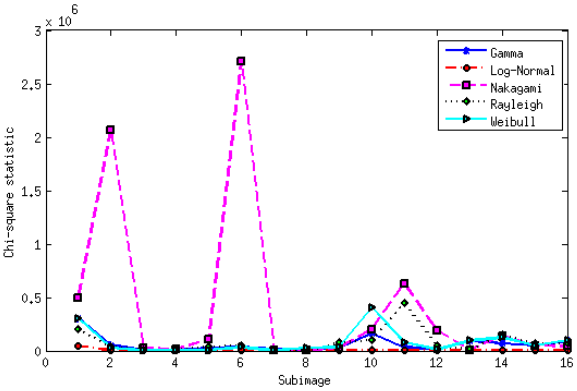

(c) χ^2 test of Sentinel-1 image

Figure 2.5: χ^2 statistics of all sub images. Lower χ^2 indicates a better fit.

With ERS 1 data, Fig. 2.4 shows that the Gamma distribution fits well the histogram, in particular at the heavy-tail and the Log-normal also seems to be appropriate for this data. Fig. 2.5 (a) indicates that the Gamma distribution is the best fit to 3-look ERS 1 data. With the whole set of sub-images, the Gamma and the Log-normal can be selected as suitable distributions to model the observed SAR images. The Log-normal and Weibull distributions have the χ^2 statistics which are quite similar, but the Log-normal's performance is better than the one of Weibull on modeling this data.

In the case of TerraSAR-X data, Fig. 2.6 shows that the Gamma distribution fits well the histogram of homogeneous area but at the heterogeneous area, the Log-normal distribution is more appropriate. The observed test-site is Chamonix Mont-Blanc which is a heterogeneous region with mountainous terrain and glaciers, therefore, χ^2 statistics of the whole set of subimages (Fig. 2.5 (b)) demonstrates that the Log-normal is the most appropriate one for the data.

For the lower resolution data Sentinel-1, also over Chamonix Mont-Blanc test-

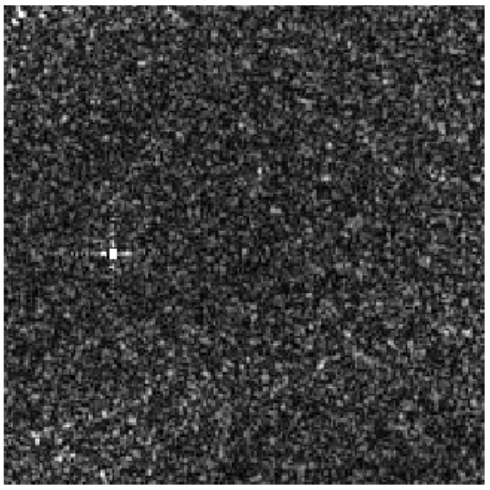

(a) Subimage n^o 12

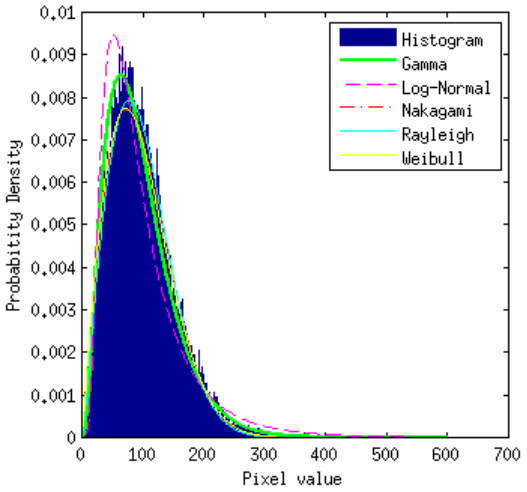

(b) Histogram fitting PDFs of subimage n^o 12

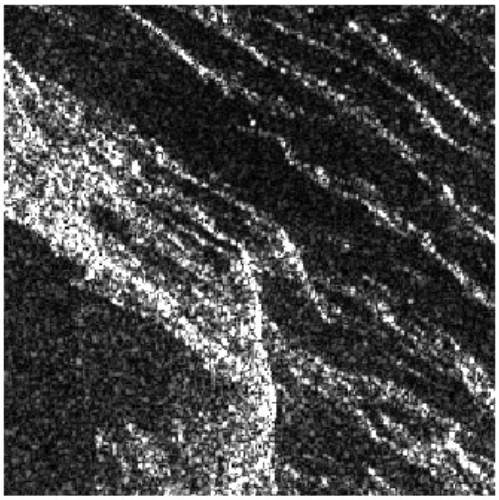

(c) Subimage n^o 14

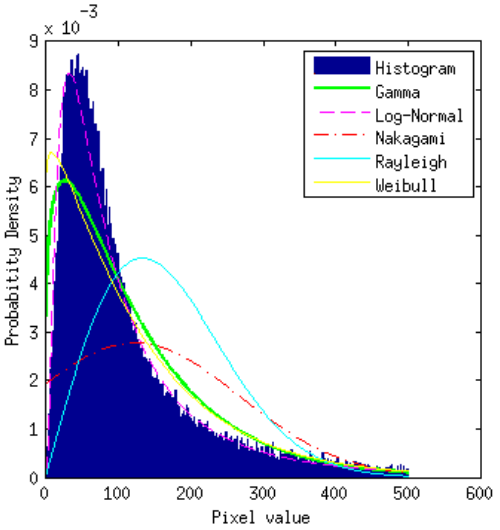

(d) Histogram fitting PDFs of subimage n^o 14

Figure 2.6: The fit of several PDFs to the histogram of TerraSAR-X image.

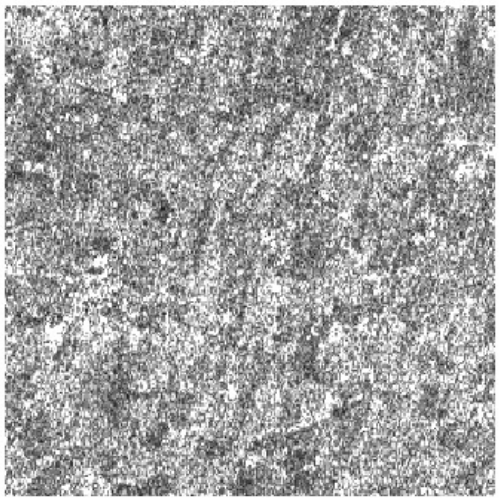

(a) Subimage n^o 4

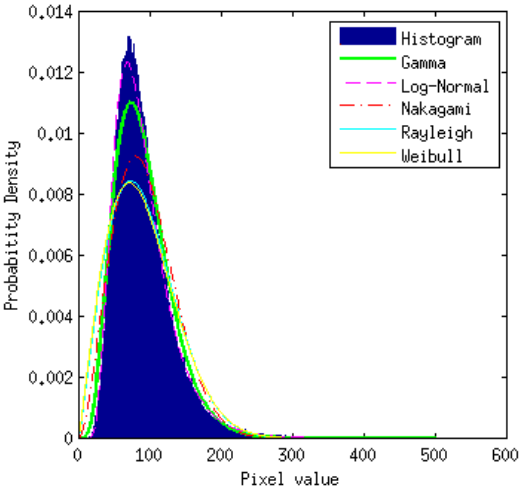

(b) Histogram fitting PDFs of subimage n^o 4

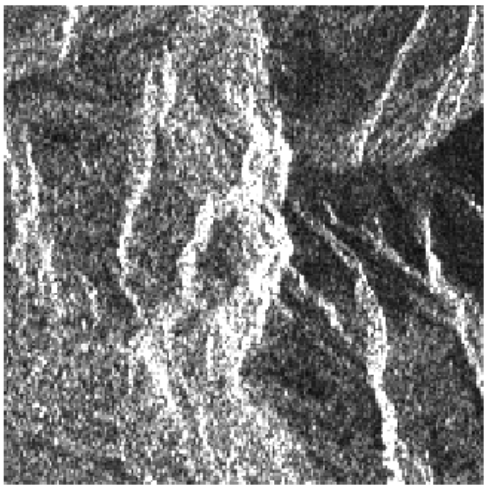

(c) Subimage n^o 11

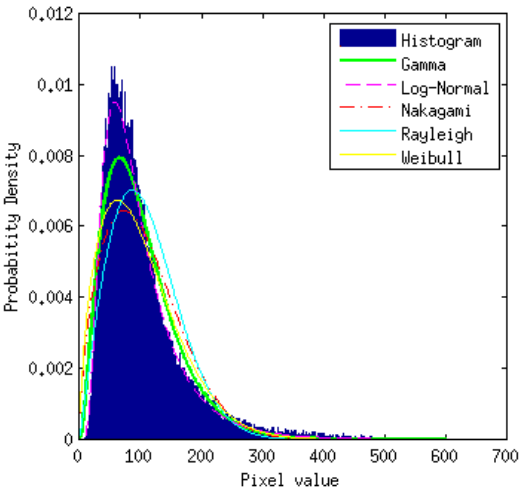

(d) Histogram fitting PDFs of subimage n^o 11

Figure 2.7: The fit of several PDFs to the histogram of Sentinel-1 image.

site, none of the given theoretical distributions fits the histogram of the real data (Fig. 2.7). According to the χ^2 statistic results (Fig. 2.5 (c)), the Log-normal distribution is the most fitted distribution among the considered distributions to the tested data.

2.2 Polarimetric SAR

The polarimetry is the study (measurement) of the electromagnetic wave polarization based on the interaction of an object, material or surface and a polarized electromagnetic wave in order to characterize the object. Antennas of polarimetric SAR systems usually transmit linearly polarized electromagnetic waves commonly on horizontal (H) and vertical (V) planes and also receive backscattered waves on these two planes. This makes possible to acquire four channels, i.e., HH, HV, VH and VV which are complex data. HH and VV are co-polarizations, obtained by operating the radar with the same (H or V) polarization on both transmitter and receiver, HV and VH are cross-polarizations, obtained by operating the radar with one (H or V) polarization on transmitter and the other (V or H) on receiver.

2.2.1 Scattering matrix

The polarimetry takes an interest in the response of targets with respect to the polarization of an incident wave. The scattering process at a target is described through the connection of the electric fields E_i and E_s of incident and scattered waves by using a scattering matrix S:

$$E_s = SE_i = \frac{e^{-jlR}}{R} \begin{bmatrix} S_{HH} & S_{HV} \\ S_{VH} & S_{VV} \end{bmatrix} E_i \tag{2.24}$$

where S_{pq} are complex scattering coefficients associated with the polarization of the incident (p) and the scattered (q) waves. S_{HH} and S_{VV} are the scattering matrix elements of co-polarization, S_{HV} and S_{VH} are the scattering matrix elements of cross-polarization. The term $\frac{e^{-jlR}}{R}$ takes into account the propagation effects both in amplitude and phase [Lee & Pottier 2009], with l the wavenumber.

The scattering coordinate system is defined for both the incident wave and the scattered wave. They are local three-dimensional coordinate systems centered on the transmitting and receiving antennas, respectively, with the z-axis in the way of the wave propagation. There are two principal conventions: forward scatter alignment (FSA) and back scatter alignment (BSA). In the FSA, the positive z-axes at the transmitter and the receiver are in the wave propagation directions, while in the BSA, the positive z-axes of these two coordinate systems point towards the target. The BSA convention is commonly used in SAR polarimetry because in the monostatic case, where radar receiver and transmitter locate at the same position, these two coordinate systems are the same in BSA convention. The scattering matrix is called Sinclair matrix S in BSA convention and Jones matrix J in FSA

convention which is well known in optical remote sensing. We have the relation between S matrix and J matrix as $J = \begin{bmatrix} -1 & 0 \\ 0 & 1 \end{bmatrix} S$.

2.2.2 Scattering vector

The scattering information can be addressed in a complex vector called scattering vector k in different bases.

$$k = \frac{1}{2}\mathrm{tr}(S\Psi) \tag{2.25}$$

where $\mathrm{tr}(\cdots)$ denotes the trace operator and Ψ is a complete set of 2×2 basis matrices which are constructed as an orthogonal set under the Hermitian inner product [Lee & Pottier 2009].

For the lexicographic basis, the matrix basis set is:

$$\Psi_l = \left\{ 2\begin{bmatrix} 1 & 0 \\ 0 & 0 \end{bmatrix} \quad 2\begin{bmatrix} 0 & 1 \\ 0 & 0 \end{bmatrix} \quad 2\begin{bmatrix} 0 & 0 \\ 1 & 0 \end{bmatrix} \quad 2\begin{bmatrix} 0 & 0 \\ 0 & 1 \end{bmatrix} \right\} \tag{2.26}$$

and Lexicographic scattering vector is defined as:

$$k_l = \begin{pmatrix} S_{HH} & S_{HV} & S_{VH} & S_{VV} \end{pmatrix}^T \tag{2.27}$$

where ^{T} denotes the transpose of the vector.
For the Pauli basis, we have

$$\Psi_p = \left\{ \sqrt{2}\begin{bmatrix} 1 & 0 \\ 0 & 1 \end{bmatrix} \quad \sqrt{2}\begin{bmatrix} 1 & 0 \\ 0 & -1 \end{bmatrix} \quad \sqrt{2}\begin{bmatrix} 0 & 1 \\ 1 & 0 \end{bmatrix} \quad \sqrt{2}\begin{bmatrix} 0 & -j \\ j & 0 \end{bmatrix} \right\} \tag{2.28}$$

then the Pauli scattering vector is:

$$k_p = \frac{1}{\sqrt{2}} \begin{pmatrix} S_{HH} + S_{VV} & S_{HH} - S_{VV} & S_{HV} + S_{VH} & j(S_{HV} - S_{VH}) \end{pmatrix}^T \tag{2.29}$$

For a reciprocal target matrix, in the monostatic backscattering case, the Sinclair scattering matrix is a symmetric matrix ($S_{HV} = S_{HV}$), 4-D scattering vectors in Eqs. (2.27) and (2.29) thus become 3-D vectors as follows:

$$k_l = \begin{pmatrix} S_{HH} & \sqrt{2}S_{HV} & S_{VV} \end{pmatrix}^T \tag{2.30}$$

$$k_p = \frac{1}{\sqrt{2}} \begin{pmatrix} S_{HH} + S_{VV} & S_{HH} - S_{VV} & 2S_{HV} \end{pmatrix}^T \tag{2.31}$$

2.2.3 Polarimetric covariance and coherency matrix

As above-mentioned, a resolution cell usually contains many random scatterers distributed in the cell. Such scatterers, are called partial scatterers and form the so-called distributed targets. Therefore, they cannot be described by a single scattering

matrix or vector (the first order polarimetric parameters). Under the assumption that the environment within a resolution cell is stationary and ergodic, distributed targets can be described by the second order polarimetric parameters, i.e., polarimetric coherency or covariance matrices. From the scattering vectors in two different bases: lexicographic (k_l) and Pauli (k_p), the polarimetric covariance matrix (C) and coherency matrix (T) are defined as expected values of the complex products of the associated scattering vectors with their conjugate transposes:

$$C = \langle k_l k_l^\dagger \rangle \tag{2.32}$$

$$T = \langle k_p k_p^\dagger \rangle \tag{2.33}$$

where $\langle \cdots \rangle$ denotes mathematical expectation and † indicates the complex conjugate transpose.

2.2.4 Polarimetric SAR statistics

In general, a scattering vector can be modeled as an m-dimensional complex circular Gaussian vector:

$$k = (S_1 \quad S_2 \quad \cdots \quad S_i \quad \cdots \quad S_m)^T \tag{2.34}$$

where m is the number of configurations of polarizations, $m = 3$ with a reciprocal medium case and $m = 4$ with nonreciprocal medium or for bistatic radars.

By applying the central limit theorem, the real and imaginary parts of each component S_i of the vector k are characterized by uncorrelated zero-mean Gaussian distributions [Goodman 1976]. The vector k thus follows a complex zero-mean Gaussian distribution [Goodman 1963]:

$$P_k(k) = \frac{1}{\pi^m \det(\Sigma)} \exp\left(-k^\dagger \Sigma^{-1} k\right) \tag{2.35}$$

where $\Sigma = \langle k k^\dagger \rangle$ is the complex covariance (C) or coherency (T) matrix which is a positive semi-definite Hermitian $m \times m$ matrix, $\det(\Sigma)$ is the determinant of Σ. In order to reduce speckle effects, L independent spatial or temporal 1-look samples are averaged in the multilook process to obtain L-look complex covariance or coherency matrix:

$$Z = \frac{1}{L} \sum_{i=1}^{L} k_i k_i^\dagger \tag{2.36}$$

The L-look complex covariance and coherency matrix follow a Wishart distribution defined as:

$$P_Z(\Sigma, L) = \frac{L^{mL} Z^{L-m}}{Z^L G_m(L)} \exp\left(\mathrm{tr}(-L Z^{-1} Z)\right) \tag{2.37}$$

where $L \geqslant m$ and $G_m(L) = \pi^{m(m-1)/2} \prod_{i=1}^{m} \Gamma(L - i + 1)$.

The Wishart distribution is the simplest model for the PDF of covariance/ coherency matrix applying for homogeneous regions and images of coarse resolu-

tion with the assumption of fully developed speckle and no texture [Lee & Pottier 2009], [Anfinsen & Eltoft 2011]. For heterogeneous regions which are more realistic cases, scattering vector is represented as a product of two independent stochastic variables:

$$k = \sqrt{z}g \tag{2.38}$$

where the square root of the positive random variable z represents the texture and g is the independent complex circular Gaussian vector representing speckle with zero mean and covariance matrix $\Sigma = \langle gg^{\dagger} \rangle$ [Oliver & Quegan 2004], [Vasile *et al.* 2010].

The complex covariance/coherency matrix of vector k is then:

$$Z = \frac{z}{L}\sum_{i=1}^{L} g_i g_i^{\dagger} \tag{2.39}$$

with the assumption that the texture is constant for each pixel averaged over the cell area.

If the texture random variable is Gamma distributed:

$$z \sim \gamma(\alpha) = \frac{\alpha^{\alpha}}{\Gamma(\alpha)} z^{\alpha-1} \exp\left(-\alpha z\right); \qquad \alpha > 0, \tag{2.40}$$

the target scattering vector follows a $\mathcal{K}$ distribution [Lee *et al.* 1994b] and then the scalar product model of multilook covariance/coherency matrix Z is:

$$\begin{aligned} P_Z(\Sigma, L, \alpha) = {} & \frac{2\left(\det(Z)\right)^{L-m}\left(L\alpha\right)^{\frac{\alpha+Lm}{2}}}{\left(\det(\Sigma)\right)^{L} G_m(L)\Gamma(\alpha)} \left(\mathrm{tr}(\Sigma^{-1}Z)\right)^{\frac{\alpha-Lm}{2}} \\ & \times K_{\alpha-Lm}(2\sqrt{L\alpha \mathrm{tr}(\Sigma^{-1}Z)}) \end{aligned} \tag{2.41}$$

where $K_{\iota}(\cdots)$ is the second-kind modified Bessel function of order ι.

For an Inverse Gamma distributed texture:

$$z \sim \gamma^{-1}(\lambda) = \frac{(\lambda-1)^{\lambda}}{\Gamma(\lambda)} \frac{1}{z^{\lambda+1}} \exp\left(-\frac{\lambda-1}{z}\right); \qquad \lambda > 0, \tag{2.42}$$

the target scattering vector follows a matrix-variate $\mathcal{G}^0$ distribution and thus we have the model of matrix Z [Frery *et al.* 1997], [Freitas *et al.* 2005] as:

$$\begin{aligned} P_Z(\Sigma, L, \lambda) = {} & \frac{L^{Lm}\left(\det(Z)\right)^{L-m}}{G_m(L)\left(\det(\Sigma)\right)^{L}} \frac{\Gamma(Lm+\lambda)(\lambda-1)^{\lambda}}{\Gamma(\lambda)} \\ & \times (L\mathrm{tr}(\Sigma^{-1}Z) + \lambda - 1)^{-\lambda-Lm} \end{aligned} \tag{2.43}$$

When the texture follows a Fisher-Snedecor distribution:

$$z \sim \mathcal{F}(\alpha, \lambda) = \frac{\Gamma(\alpha+\lambda)}{\Gamma(\alpha)\Gamma(\lambda)} \frac{\alpha}{\lambda-1} \frac{\left(\frac{\alpha}{\lambda-1}z\right)^{\alpha-1}}{\left(\frac{\alpha}{\lambda-1}z+1\right)^{\alpha+\lambda}}, \tag{2.44}$$

this distribution is the generalization of both Gamma and Inverse Gamma PDFs [Bombrun *et al.* 2011a] as:

$$\lim_{\lambda \to 0} \mathcal{F}(z, L, \alpha, \lambda) = \gamma(z, L, \alpha); \tag{2.45}$$

$$\lim_{\alpha \to 0} \mathcal{F}(z, L, \alpha, \lambda) = \gamma^{-1}(z, L, \lambda). \tag{2.46}$$

then the Kummer$\mathcal{U}$ distribution is given for L-look covariance/ coherency matrix Z [Bombrun & Beaulieu 2008], [Bombrun *et al.* 2011b] by:

$$\begin{aligned} P_Z(\Sigma, L, \alpha, \lambda) = & \frac{L^{Lm} \left(\det(Z)\right)^{L-m}}{G_m(L) \left(\det(\Sigma)\right)^L} \frac{\Gamma(\alpha+\lambda)}{\Gamma(\alpha)\Gamma(\lambda)} \left(\frac{\alpha}{\lambda-1}\right)^{Lm} \Gamma(Lm+\lambda) \\ & \times U\left(Lm+\lambda, Lm-\alpha+1, L\mathrm{tr}(\Sigma^{-1}Z)\frac{\alpha}{\lambda-1}\right) \end{aligned} \tag{2.47}$$

with $U(\cdots)$, the second-kind confluent hypergeometric Kummer function. The distributions in Eqs. (2.41), (2.43) and (2.47) have been normalized to unit mean [Anfinsen & Eltoft 2011].

2.3 Conclusions

In this chapter, we have presented the principal elements for the general understanding of SAR imaging. We have focused on the formation of single- and multi-polarization SAR data and their statistical properties. The fit of several standard probability distributions to different SAR amplitude data has been tested using the χ^2 statistics. In practice, real SAR amplitude data often present non-Rayleigh distribution with a heavy tail, and SAR intensity data at homogeneous region follow a Gamma distribution. However, at a heterogeneous region, an empirical approach like the Log-normal distribution is more appropriate. For PolSAR data, the complex Wishart distribution is still widely used due to its mathematical efficiency under the assumption of Gaussian statistics. In non-Gaussian cases, the $\mathcal{K}$, $\mathcal{G}^0$ and Kummer$\mathcal{U}$ distributions are more appropriate to real data.

Chapter 3

SAR image filtering and change detection

Contents

Change detection of specific features within a certain time interval using SAR data has to deal with a complex processing of this data and the so-called speckle which makes the use of SAR imagery difficult. In this chapter, the use of SAR image time series for the Earth observations/monitoring and a general overview of speckle filtering and change detection of SAR images is provided. In particular, similarity measurements exploited in this thesis as well as those commonly used for SAR and PolSAR data in literature are also given.

3.1 SAR image time series and applications

The launch of new generation satellites (e.g., TerraSAR-X, COSMO-SkyMed, ALOS, RADARSAT-2, Sentinel-1, etc.,) makes it possible to obtain time series of SAR images with high quality of both temporal and spatial resolutions. Many sensors frequently produce images over a scene with short repeat cycles, for instance, 11 days for TerraSAR-X images, 12 days for the new SAR images acquired by Sentinel-1A (launched in April, 2014), and even 6 days together with Sentinel-1B (to be launched in 2016). Designed with different acquisition modes, recent SAR sensors provide high (about 10 m) and very high (up to 1 m or less) spatial resolution SAR images. A SAR Image Time Series (SAR ITS) is defined as a sequence of SAR images over the same scene with observations from repeat cycles for a certain period. With multitemporal data, spatial and temporal information can simultaneously be exploited

to improve the results of research works. Indeed, in an ITS, many observations of the same scene are acquired. If there is no change, redundant information can be used for structure detection and for multitemporal filtering in order to increase precision and reliability. On the opposite, if there are changes in the time series, they should be detected and preserved in the data processing. This change information allows us to analyze the temporal evolution of objects within the scene. Applications employing information of SAR ITS are very diversified, such as: land cover classification [Bruzzone *et al.* 2004], [Waske & Braun 2009], [Lardeux *et al.* 2011]; natural/artificial feature mapping and analysis: forest [Quegan *et al.* 2000], [Champion *et al.* 2014], wet snow cover [Schellenberger *et al.* 2012], crop [Jiao *et al.* 2014], etc.; change detection [Gar-OnYeh & Qi 2015], [Akbari *et al.* 2014], etc.. In this thesis, change detection is one of our interests.

In the past few years, change detection techniques have been an active domain attracting interest for the analysis of multitemporal remote sensing imagery, (in particular SAR is well suited for change detection thanks to its advantages), due to their use in many fields of applications. Change detection is a difficult task which intends to determine the changes of specific features within a certain time interval by different temporal observations of the same scene. Two main kinds of change which can be observed in a time series are surface change and motion. In this thesis, we focus on the surface change issue.

Earth's surface is constantly changing, based on the nature/speed of changes occurring, we can observe:

- Many processes which change Earth's landscape instantaneously, called rapid change or abrupt change. This kind of changes are usually natural/human disasters which are the causes of huge damages to humans, such as: flood [Dellepiane & Angiati 2012], [Refice *et al.* 2014], fire (forest fire) [Leblon *et al.* 2002], tsunami [Chen & Sato 2013], volcanic eruption [Le *et al.* 2015b], etc.

- While other changes take place gradually over time, called slow changes. Some examples of these slow processes are: soil erosion [Amitrano *et al.* 2015], coastal marine erosion [Kerbaol & Collard 2005]; desertification [Catherine & Andre 2007]; seasonal changes of evolution of vegetation [Bouvet *et al.* 2009], forest [Pantze *et al.* 2010], etc.; or progressive expansion of agriculture/urban areas [Gomez-Chovaa *et al.* 2006], [Gar-OnYeh & Qi 2015], etc.

Motion or change detection of moving areas is also widely studied using SAR data. Target/surface displacements can be measured by amplitude correlation or phase differences (interferograms). SAR Interferometry (InSAR) or Differential SAR interferometry (D-InSAR) can measure ground deformations with a precision of a fraction of the wavelength [Massonnet & Feigl 1998]. Monitoring of this kind of change is an important issue for socio-economics, such as risk, damage assessment: landslide detection [Colesanti & Wasowski 2006], earthquake [Brunner *et al.* 2010], glacier [Engeset *et al.* 2002], [Schubert *et al.* 2013], ice sea motion [Lehtiranta *et al.* 2015], etc.

3.2 Despeckling of SAR images

In literature, in order to improve the efficiency of using SAR images, speckle filtering is often required as a preprocessing step. Many different approaches have been developed for the speckle reduction. In this section, an overview of SAR image filtering is organized as follows: spatial (for both local approaches and nonlocal approaches), multitemporal filtering of SAR images and PolSAR image filtering.

3.2.1 Spatial filtering

A large number of speckle filtering approaches have been proposed for single date SAR images (using spatial information only). An important issue of a filter is the sample selection for filtering process. In this respect, we have:

- **Local approaches:**
  These filters use the window/neighborhood of the considered pixel to estimate the filtered value. Different spatial estimation supports have been developed:
  * Boxcar window [Lee 1980], [Frost *et al.* 1982], [Kuan *et al.* 1987], etc., in which optimal parameters are estimated by a fixed-size rectangular window sliding through each pixel of the image. This is the simplest analysis window, its disadvantage is that speckle reduction also impacts the edge sharpness.
  * Directional neighborhood: For the edge preservation purpose, estimation neighborhood near the high contrast area takes the orientation of the edge into account by incorporating the local gradient or subwindow homogeneity into the local estimation algorithm [Lee 1981]. These approaches have better performances compared to boxcar algorithms, but the number of directions is limited.
  * Adaptive neighborhood: These approaches aim at seeking the most suitable neighborhood of each pixel. The adaptive neighborhood can be:
    - The maximum homogeneous region (the region including pixels belonging to the same statistical population) selected by testing the evolution of the standard deviation σ [Wu & Maitre 1992] or the coefficient of variation (CV) [Nicolas *et al.* 2001].
    - The neighborhood consisting of pixels which are similar to the seed pixel (the pixel being processed) [Rangayyan *et al.* 1998], [Vasile *et al.* 2006]. Local estimation within this adaptive neighborhood, hence, yields more accurate results than within a fixed neighborhood.
- **Nonlocal approaches:**
  These filters derive the filtered value by taking into account all the pixels being in the similar context with the considered pixel. Each searching pixel has a weight calculated by a similarity measure between considered patch and searching patch. This idea was first introduced in [Buades *et al.* 2005]

under the additive white Gaussian noise assumption and has been extended for SAR images in many researches such as: the Probabilistic Patch-Based (PPB) filter [Deledalle *et al.* 2009], which derives the weights iteratively by using maximum likelihood function. The speckle Bayesian NonLocal (BNL) mean filter [Zhong *et al.* 2011] resolves the bias assumption problem in the original BNL filter by incorporating Lee improved sigma filter. The SAR Block-Matching 3D (SAR-BM3D) filter [Parrilli *et al.* 2012] refines the results obtained from BM3D algorithm by using the Locally Linear Minimum Mean Square Error (LLMMSE) estimator in the wavelet domain and this approach is improved in [Cozzolino *et al.* 2013] to speed up block-matching. The Space-domain Filter with Alterable Window (SFAW) [Li *et al.* 2013] is a modified bilateral filter based on local CV and the joint probability density function model to adapt the window direction by different weights due to different local structures.

Besides that, in terms of speckle stationarity or non-stationarity, two models are used (multiplicative speckle model and product model for non-stationarity), leading to different filtering approaches. Indeed, multiplicative speckle model-based approaches [Lee 1980], [Frost *et al.* 1982], [Kuan *et al.* 1987], etc., are based on the assumption that speckle is stationary over the whole image (or locally stationary within a processing window). In the case where the scene is non-stationary, the product model requires to give several known probability distributions of the observed area and of the speckle [Lopes *et al.* 1993], [Datcu *et al.* 1998], etc. A complete review of this aspect is available in [Touzi 2002].

In terms of estimator selection, there are many algorithms for estimating filtering values, such as: Bayesian estimator [Lopes *et al.* 1993], [Datcu *et al.* 1998], Minimum Mean Square Error (MMSE) [Arsenault & Levesque 1984], [Hillion & Boucher 1988], LLMMSE [Lee *et al.* 2003], [Vasile *et al.* 2006], Weighted Maximum Likelihood Estimator (WMLE) [Deledalle *et al.* 2009], Minimum Error Norm Estimator (MENE) [Atto *et al.* 2012], [Le *et al.* 2013], etc. The choice of filtering estimator depends on SAR data and application purposes after filtering.

3.2.2 Multitemporal filtering

Several approaches have been developed for multitemporal filtering, the three first filters introduced below were reviewed and compared in [Trouve *et al.* 2003]. Most multitemporal filters have been extended from spatial filters.

3.2.2.1 Multichannel filter

This filter proposed in [Bruniquel & Lopes 1997] is based on a statistical approach. First, local statistics (means, variances, and channel cross correlations) for each pixel (i, j) of each image $I_t (1 \leqslant t \leqslant N)$ in a time series composed of N images are estimated by using a spatial window. Then Kuan's filter is applied to obtain the texture compensation of each image $\tilde{I}_t$. A summation weight A_t is computed

in order to have the optimal variance of the output, then the filtered image $\hat{I}_t$ is derived as:

$$\hat{I}_t(i,j) = \sum_{k=1}^{N} \frac{A_k(i,j) I_k(i,j)}{\tilde{I}_k} \tilde{I}_t \tag{3.1}$$

The increase of the window size reduces the estimation variance in homogeneous areas and leads to more stable inversion of the equation system. However, the filtered images tend to be blurred.

This summation weight is also applied in approaches [Quegan *et al.* 2000] and [Quegan & Yu 2001] with a more explicit form, and the filter is simply as:

$$\hat{I}_t(i,j) = \frac{\langle I_t(i,j) \rangle}{N} \sum_{k=1}^{N} \frac{I_k(i,j)}{\langle I_k(i,j) \rangle} \tag{3.2}$$

where $\langle I_t(i,j) \rangle$, $\langle I_k(i,j) \rangle$ are the local mean values of pixels in a window centered at pixel (i,j) in images I_t and I_k.

3.2.2.2 Time-space filter

In [Coltuc *et al.* 2000], the proposed method is based on a unitary transform applied on time axis to isolate the useful signal from the noise. The logarithm is applied to handle additive noise and the Discrete Cosine Transform (DCT) permits to transform temporal axis into frequency axis while keeping the data as real values. The images corresponding to different dates become frequency channels, where the noise and the signal are mutually separated. Supposing that the additive returned noise is independent from the signal and temporally decorrelated, it spreads on all DCT channels. On the other hand, the signal correlated in time concentrates on the zero frequency channel, the mean of log-intensity. Then, a spatial adaptive filter is used to reduce the noise on each frequency channel, except on the zero frequency channel in order to preserve the spatial resolution of the stable information. A 9×9 or 11×11 window provides the expected noise reduction on homogeneous areas of the nonzero frequency DCT channels.

3.2.2.3 Three-dimensional adaptive neighborhood filter

The approach in [Ciuc *et al.* 2001] extends the 2D adaptive neighborhood filtering to multitemporal data by using both spatial and temporal neighbors of the observed pixel. The idea is to find homogeneous regions in a 3D neighborhood in the volume of piled up coregistered images. The method includes the following steps: firstly, by using a spatial 3x3 median filter, the local mean is calculated. After that, authors used a narrow interval to aggregate pixels if their values appertain to that interval, this idea is based on the Sigma filter [Lee 1983]. After estimating reliable mean, the considered and rejected pixels at previous step are tested again with a larger interval. At last, filtered values are computed on the obtained 3D neighborhood by using Kuan's filter.

3.2.2.4 Two step multitemporal nonlocal mean filter

This filter [Su *et al.* 2014] is developed from the PPB filter [Deledalle *et al.* 2009] by a strategy including two steps:

1) In the first step, pre-denoised images are prepared for temporal averaging process by using PPB filter, then binary weights representing the presence of changes are calculated by using Generalized Likelihood Ratio (GLR) criterion and Kullback-Leibler (KL) divergence, afterward averaged data are obtained by taking into account both spatially and temporally varying number of looks.

2) In the second step, PPB filter is applied to averaged results in step 1.

The filter can also be used for unregistered data by using an offset vector between two pixels at the same pixel location but different geographic positions.

3.2.3 Polarimetric SAR image filtering

For multipolarization SAR data, many approaches are also proposed for spatial filtering but there are rare approaches dedicated to multitemporal filtering. Several filters for this kind of data can be found in literature.

The Polarimetric Whitening Filter (PWF) [Novak & Burl 1990] optimally combines elements of the scattering matrix and produces a single scalar intensity image in which speckle is reduced but the polarization information is lost. This filter is then developed for multilook complex data (Multilook PWF - MPWF) [Lopes & Sery 1997] related to the texture variation by using a product model for texture and speckle noise.

In [Lee *et al.* 1991], authors use the multiplicative speckle model and minimize the mean square error to filter the diagonal terms of the covariance matrix, which are real and represent the channel powers.

IDAN (Intensity Driven Adaptive Neighboorhood) [Vasile *et al.* 2006], an adaptive filter, is proposed for coherency matrix of PolSAR, InSAR and PolInSAR data using intensity information to grow the adaptive neighborhood (like the search of 3D adaptive neighborhood in multitemporal approach in section 3.2.2.3). Then filtered value is derived by applying a estimator like ML, LLMMSE, etc., to the obtained adaptive neighborhood.

To preserve the dominant scattering mechanism of each pixel, the approach proposed in [Lee *et al.* 2006] is based on the Freeman and Durden decomposition [Freeman & Durden 1998] to separate pixels into three dominant scattering categories: surface, double bounce, and volume. By using an unsupervised classification map derived after the decomposition as a mask, the averaging process of the filter includes only pixels in the same dominant scattering category.

In [Alonso-Gonzalez *et al.* 2012], a multiscale PolSAR data filtering technique is introduced based on a Binary Partition Tree (BPT) representation of the data. The BPT construction process is based on a region model which enables to represent

the homogeneous areas, and based on a dissimilarity measure in order to identify similar areas and the merging sequence.

Nonlocal mean filter is also developed for PolSAR data in [Liu & Zhong 2014] based on Discriminative Similarity Measure (DSM). The DSM deals with the speckle-free signal and the speckle discriminatively based on a Maximum A Posteriori (MAP) form. This form allows cooperation between the similarity of the speckle (corresponding to the performance of speckle smoothing) and the similarity of the underlying signal (corresponding to the detail preservation).

3.3 SAR image change detection

3.3.1 Change detection approaches for SAR data

3.3.1.1 Change detection in initial image domain

For the change detection task using SAR images, the classical Log-ratio of two co-registered observations of the same scene is proposed to detect SAR change features in [Rignot & vanZyl 1993]. Ratio operator is more effective to detect changes than the difference operator in SAR images because of:

- the speckle: the expected property of constant false alarm rate (CFAR) is obtained by using the ratio, whereas for the difference, the false alarm rate would increase with the backscattering coefficient [Touzi *et al.* 1988];
- the robustness of the ratio operator to calibration errors: these errors are reproduced in each repeat-pass image, and they can be eliminated in the ratio image computation.

The ratio (or Log-ratio) is then developed in other approaches. The Generalized Likelihood Ratio Test (GLRT) [Lombardo & Olivier 2001] extends the ratio operator for change detection on SAR ITS. This is a ML change detection using a normalized log of the ratio of geometric and arithmetic means of temporal texture measure. The authors show that the normalized log measure can provide reasonable classification with reduced computation load. While approach in [Dierking & Skriver 2002] uses the ratio operator to compare the temporal images and a decision mechanism based on a desired value of the probability of false alarm.

To describe the statistical distribution under changed and unchanged hypotheses, some distribution models are used, such as: the Gamma distribution (for a homogeneous area) and the mixture distribution (for a heterogeneous area) [Bujor *et al.* 2004], the GG [Bazi *et al.* 2005], the Nakagami-ratio, the Weibull-ratio and the Log-normal models [Moser & Serpico 2006], etc. Several schemes can be used to estimate the parameters of distribution models such as: the Method of Moments (MoM) [Bazi *et al.* 2005], the ML [Lombardo & Olivier 2001] methodology and Method of Log-Cumulant (MoLC) [Bujor *et al.* 2004], [Moser & Serpico 2006], etc.

In [Quin *et al.* 2014], an original approach called Method for generalIzed Means Ordered Series Analysis (MIMOSA) is proposed. The Fisher distribution is used

for modeling SAR amplitude images of the time series. MIMOSA method compares two different temporal means between the amplitude images (geometric mean with harmonic or arithmetic or quadratic mean). Based on the theoretical joint PDF between the two temporal means, the decision is made according to a given false alarm rate.

Kullback-Leibler (KL) divergence is introduced as a quantitative measurement of differences between PDFs [Inglada 2003]. Then the calculation of KL divergence is performed through edgeworth approximation in [Inglada & Mercier 2007] based on the evolution of the local statistics of the image between two dates.

In order to automatically take decision for changed and unchanged classes, some thresholding algorithms are implemented, for instance: Otsu's method [Otsu 1979], entropy-based algorithm [Pun 1980], Kittler-Illingworth (KI) threshold [Kittler & Illingworth 1986], CFAR detection, etc. The approach in [Bazi *et al.* 2005] uses a reformulation of the KI threshold with the Generalized Gaussian (GG) assumption for modeling the statistical distributions of changed and unchanged classes in the Log-ratio image. Then, another version of this threshold is developed for the specific non-Gaussian statistics of SAR amplitude ratio images [Moser & Serpico 2006]. The CFAR detection algorithm is also often used for change detection of SAR images with several modeling statistical distributions of the data. For instance, the K distribution [Paes *et al.* 2010], the Log-Normal distribution [Ai *et al.* 2010] are used for the ship detection. This algorithm is also proposed for the GΓD distributed background of high resolution SAR images in [Qin *et al.* 2013].

3.3.1.2 Change detection in wavelet transform image domain

Wavelet transform for change detection purpose is also studied in several approaches. A wavelet decomposition is based on both level-dependent high- and low-pass wavelet filters in order to represent a signal at different scales or resolutions. At a particular resolution of the wavelet decomposition, the one dimensional (1D) signal $S(x)$ is approximated by a sum of scaling functions ϕ_x (low-pass function), and the details at the finer resolution can be expressed by a sum of wavelet functions ψ_x (high-pass function) [Horgan 1998]. For a two-dimensional (2D) wavelet representation of a signal $\mathcal{I}(x, y)$ (e.g., rows and columns of an image), $\phi_x\phi_y$ is a 2D scaling function, and the details needed to achieve the next finer resolution can be represented by three wavelets, $\phi_x\psi_y$, $\psi_x\phi_y$ and $\psi_x\psi_y$. A wavelet transform representation of an image $\mathcal{I}$ has the form:

$$\begin{aligned}\mathcal{I}^{\mathcal{W}[j,\varepsilon]} &= \mathcal{W}[j,\varepsilon]\{\mathcal{I}\} \\ &= \left\{\mathcal{I}, \phi_{(J,x)}\phi_{(J,y)}\right\} + \sum_{j=1}^{J}\left\{\mathcal{I}, \phi_{(j,x)}\psi_{(j,y)}\right\} \\ &+ \sum_{j=1}^{J}\left\{\mathcal{I}, \psi_{(j,x)}\phi_{(j,y)}\right\} + \sum_{j=1}^{J}\left\{\mathcal{I}, \psi_{(j,x)}\psi_{(j,y)}\right\}\end{aligned} \tag{3.3}$$

where the operator $\mathcal{W}[j, \varepsilon]$ computes the wavelet decomposition at level j ($j \in \{1, 2, \cdots, J\}$) into four coefficients $\mathcal{I}^{\mathcal{W}[j,\varepsilon]}$ with $\varepsilon \in \{0, 1, 2, 3\}$ corresponding to terms of the sum in the right part of Eq. (3.3), which are approximation, horizontal, vertical and diagonal coefficients, respectively.

A Two-Dimensional Stationary Wavelet Transform (2D-SWT) based multiscale decomposition of the Log-ratio image in multitemporal SAR data [Bovolo & Bruzzone 2005] transforms Log-ratio images in different dependent levels of change signal. The final change detection result is obtained according to an adaptive scale-driven fusion algorithm. This method is then extended in [Marin *et al.* 2015] for building change detection. Here, after the wavelet decomposition, the optimal building scale is selected. Then, changes associated with the increase and the decrease of backscattering at this scale are identified by using split-based threshold selection [Bovolo & Bruzzone 2007]. Finally, the extracted change information is classified into four defined types of building change based on backscattering models of new/destroyed building and a fuzzy theory.

Wavelet/curvelet transforms are also applied in [Atto *et al.* 2013] for the analysis of SAR ITS. In this approach, each image in the ITS is decomposed by SWT and Fast Discrete Curvelet Transform (FDCT). Wavelet frame are relevant to build parsimonious models by reducing several types of lower and higher order dependencies which related to the presence of non-stationarities in SAR images. Changes in the time series are detected by Kullback-Leibler (KL) divergences between image features (distribution parameters) extracted from SWT and FDCT in two stages:

1) global changes at images/subimages level expressed through a Multi-Date Divergence Matrix (MDDM),

2) changes between acquisitions-of-interest derived from MDDM analysis at pixel level.

The SWT and FDCT subbands of SAR images are considered as stochastic fields due to speckle occurring in this data. The parameter extraction is thus from stochastic modeling of SWT and FDCT coefficients. Approximations are modeled by edgeworth expansions, while parameters of the statistical modeling distributions for SWT details and FDCT orientations are selected based on the Kolmogorov stochasticity test. Indeed, the ML method is used to estimate the parameters of GG, Log-normal and Weibull distributions for SWT details and FDCT orientations. Then, the most relevant distribution which has the smallest value in the Kolmogorov test is selected.

The SWT [Coifman & Donoho 1995], [Atto & Berthoumieu 2012] exploited in the approaches above is a wavelet transform proposed to overcome the lack of translation invariance of the Discrete Wavelet Transform (DWT).

3.3.2 Similarity measurement for SAR and PolSAR data

3.3.2.1 Coefficient of variation for homogeneity test

To test the homogeneity over reduced number of samples, the local coefficient of variation (CV) can be a test criterion and an adaptive threshold can deal with the variation of number of samples in each test. Let us consider an $L-$looks amplitude image $\mathcal{I}$ at pixel position (i, j):

$$\mathcal{I}(i,j) = \varrho(i,j).s(i,j) \tag{3.4}$$

where, $\varrho(i,j)$ is the speckle-free image and $s(i,j)$ is the speckle noise, L is the number of looks, i.e., the number of independent samples averaged when the image is produced. Standard deviation of speckle noise in purely homogeneous area is $\sigma_s = \frac{0.5227}{\sqrt{L}}$ [Lopes *et al.* 1993]. The CV is denoted as the ratio of standard deviation to the mean of the observed image.

$$CV = \frac{\sigma_{\mathcal{I}}}{\mu_{\mathcal{I}}} \tag{3.5}$$

If the ground surface is purely homogeneous, we should have $CV = \sigma_s$. On the contrary, if it varies because of textures, edges, isolated targets, etc., the CV increases: CV $> \sigma_s$. The CV can, thus, be a measure to test the homogeneity of the ground surface reflectivity. The test is represented as:

$$CV(i,j) \leq \sigma_s + \delta(i,j) \tag{3.6}$$

where $\delta(i,j)$ is a small value added to σ_s as a tolerance of the threshold and derived from [Park *et al.* 1999].
Hence, the adaptive threshold is denoted:

$$\lambda(i,j) = \zeta\left(\sigma_s + \sigma_s\sqrt{\frac{1+2\sigma_s^2}{2n(i,j)}}\right) \tag{3.7}$$

in which, $n(i,j)$ is the number of elements involved in the CV test, ζ is a system parameter that determines the degree of smoothing. In general, the values of ζ are around 1.0 [Park *et al.* 1999].

3.3.2.2 Kullback-Leibler distance

The Kullback-Leibler (KL) divergence [Kullback & Leibler 1951] is a non-symmetric measure of the difference between two probability distributions P_X and P_Y of random variables X and Y.

$$\mathcal{K}(X \parallel Y) = \int P_X(x) \log\left(\frac{P_X(x)}{P_Y(x)}\right) dx \tag{3.8}$$

The KL divergence can be appropriate for change detection when changes on the ground is considered to induce different shapes of the local PDF [Inglada & Mercier 2007].

The symmetric KL distance can be defined as:

$$d_{KL}(X,Y) = d_{KL}(Y,X) = \frac{1}{2}\left(\mathcal{K}(X \parallel Y) + \mathcal{K}(Y \parallel X)\right) \tag{3.9}$$

This distance is exploited in [Atto *et al.* 2013] between two SWT decomposed images as:

$$\begin{aligned} d_{KL}^{\mathcal{W}}(\mathcal{I}_t, \mathcal{I}_\ell) = & \, d_{KL}\left(\mathcal{I}_t^{\mathcal{W}[J,0]} + \mathcal{I}_\ell^{\mathcal{W}[J,0]}\right) \\ & + \sum_{\substack{j\in 1,2,\cdots,J \\ \varepsilon \in 1,2,3}} d_{KL}\left(\mathcal{I}_t^{\mathcal{W}[j,\varepsilon]} + \mathcal{I}_\ell^{\mathcal{W}[j,\varepsilon]}\right) \end{aligned} \tag{3.10}$$

where $\mathcal{I}_t^{\mathcal{W}[k,\varepsilon]}$ and $\mathcal{I}_\ell^{\mathcal{W}[j,\varepsilon]}$ are SWT coefficients of images $\mathcal{I}_t$ and $\mathcal{I}_\ell$, respectively.

The KL distance of two scaled complex Wishart populations is given in [Frery *et al.* 2014] as follows:

$$\begin{aligned} d_{KL}(Z_1, Z_2) = & \frac{L_1 - L_2}{2}\left\{\log\frac{Z_1}{Z_2}\log\frac{L_1}{L_2}\right. \\ & + m\left[\Psi^{(0)}(L_1 - m + 1) - \Psi^{(0)}(L_2 - m + 1)\right] \\ & \left. + (L_2 - L_1)\sum_{i=1}^{m-1}\frac{i}{(L_1 - i)(L_2 - i)}\right\} \\ & + \frac{\operatorname{tr}\left(L_2 Z_2^{-1} Z_1 + L_1 Z_1^{-1} Z_2\right)}{2} - \frac{m(L_1 + L_2)}{2} \end{aligned} \tag{3.11}$$

in which Z_1 and Z_2 are $m \times m$ covariance matrices with L_1- and L_2-looks, respectively. $\Psi^{(0)}(\cdot)$ is the digamma function.

3.3.2.3 Bhattacharyya distance

The Bhattacharyya distance measures the similarity of two discrete or continuous probability distributions [Bhattacharyya 1943].

$$d_{BH}(X,Y) = -\log\left(\int \sqrt{P_X P_Y}\right) \tag{3.12}$$

where, P_X and P_Y are two probability laws of the random variables X and Y.

This approach is used in [Morio *et al.* 2008], in order to measure the contrast between two regions on SAR image. Then, in [Morio *et al.* 2009], Bhattacharyya distance is decomposed as the sum of three terms that represent the contributions of intensity, polarimetry, and interferometry.

The Bhattacharyya distance of two covariance matrices which follow the Wishart

distributions is defined in [Frery *et al.* 2014] as:

$$\begin{aligned} d_{BH}([Z_1],[Z_2]) = & \frac{L_1 \log\left(\det\left([Z_1]\right)\right)}{2} + \frac{L_2 \log\left(\det\left([Z_2]\right)\right)}{2} \\ & - \frac{L_1+L_2}{2} \log\left(\det\left(\frac{L_1[Z_1]^{-1} + L_2[Z_2]^{-1}}{2}\right)\right) \\ & + \sum_{i=0}^{m-1} \log\left(\frac{\sqrt{\Gamma(L_1-1)\Gamma(L_2-1)}}{\Gamma\left(\frac{L_1+L_2}{2}-i\right)}\right) \\ & - \frac{m}{2}\left(L_1 \log\left(L_1\right) + L_2 \log\left(L_2\right)\right) \end{aligned} \tag{3.13}$$

3.3.2.4 Wishart distance

For PolSAR images where the scattering information can be addressed in a complex vector or a covariance/ coherency matrix, some similarity measures are used for classification purposes: the Wishart distance, the spherically invariant random vector (SIRV) distance [Vasile *et al.* 2010], the Wishart-Chernoff (WC) distance [Dabboor *et al.* 2013], etc.

The Wishart distance [Lee *et al.* 1994a] is derived from ML procedure under Wishart distribution assumption for the averaged covariance/coherency matrix Z. The Wishart distance derived from maximum likelihood procedure on Wishart distribution assumption is:

$$d_{Wishart}\left(Z_1, Z_2\right) = \ln\left(\det\left(Z_2\right)\right) + \mathrm{Tr}\left(Z_2^{-1} Z_1\right). \tag{3.14}$$

The revised Wishart distance derived from likelihood ratio test is introduced in [Kersten *et al.* 2005] as:

$$d_{R-Wishart}\left(Z_1, Z_2\right) = \ln\left(\frac{\det(Z_2)}{\det(Z_1)}\right) + \mathrm{Tr}(Z_2^{-1} Z_1) - m \tag{3.15}$$

where m is the dimension of the target vector.
Then a symmetric measure is defined as:

$$\begin{aligned} d^S_{R-Wishart}\left(Z_1, Z_2\right) &= \frac{1}{2}\left(d_{R-Wishart}\left(Z_1, Z_2\right) + d_{R-Wishart}\left(Z_2, Z_1\right)\right) \\ &= \frac{1}{2}\mathrm{Tr}\left(Z_1 Z_2^{-1} + Z_2 Z_1^{-1}\right) - m. \end{aligned} \tag{3.16}$$

3.3.2.5 Spherically invariant random vector (SIRV) distance

The previous measure is dominated by the intensity (SPAN) information. To reduce this effect, the SIRV model has been proposed for PolSAR data. As introduced in Section 2.2.4, target vector can be represented as a product of two independent stochastic variables: $k = \sqrt{z}g$, where the square root of the positive random variable z represents the texture and g is the independent complex circular Gaussian vector representing speckle with zero mean and covariance matrix $\Sigma = \langle gg^{\dagger} \rangle$.

The maximum likelihood distance associated to this model is proposed for unsupervised PolSAR classification [Vasile *et al.* 2010], [Formont *et al.* 2011] as:

$$d_{SIRV}\left(Z_{FP}, Z\right) = \ln\left(\frac{\det\left(Z\right)}{\det\left(Z_{FP}\right)}\right) + \frac{m}{L}\sum_{i=1}^{L}\frac{k_i^{\dagger} Z^{-1} k_i}{k_i^{\dagger} Z_{FP}^{-1} k_i} \tag{3.17}$$

where,

$$Z_{FP} = \frac{m}{L}\sum_{i=1}^{L}\frac{k_i k_i^{\dagger}}{k_i^{\dagger} Z_{FP} k_i} \tag{3.18}$$

is the "fixed point" estimator of the normalized covariance matrix in the deterministic texture case.

More measures of similarity/dissimilarity for PolSAR data can be consulted in [Trouve 2011] or in a survey by [Yang *et al.* 2015].

3.4 Conclusions

In this chapter, we have introduced the advantages and potentials of SAR ITS in the Earth observation/monitoring and have reviewed the main approaches proposed for SAR image filtering and change detection.

With filtering approaches, almost all multitemporal filters are not explicitly taking the presence of changes in the time series into account. Hence, the samples selected for the filtering process are often local spatio-temporal neighbors of the processing pixel. This can smooth the change and detail information of the original time series and may lead to the radiometric, spatial and temporal degradation of filtered values. In recent approaches of change detection and change analysis on SAR ITS like MDDM approach [Atto *et al.* 2013] and MIMOSA approach [Quin *et al.* 2014], some authors focus either on the spatial or on the temporal localization of changes. In MDDM approach, changes are detected at image level (for the whole images in the time series). Only one MDDM is, therefore, obtained for the time series. It can be observed in the MDDM when changes globally occur in temporal domain but can not be determined where they are in spatial domain. Whilst in MIMOSA approach, the joint-use of the two temporal means can identify where changes occur but it can not point out when. In Chapter 5, we will propose a framework for change analysis of SAR ITS which can overcome the limitations of these multitemporal filtering and change detection approaches.

Each distance introduced in section 3.3.2 can be suitable for a kind of data depending on the natural statistics of SAR/PolSAR imagery and the purpose of application. This gives a fundamental tool for the approach proposed in this thesis.

Chapter 4

Data description and preprocessing

Contents

In this chapter, we introduce the study areas and datasets used in the experimental works, as well as several preprocessing steps executed before extracting information from these data. Two test-sites are studied: Chamonix Mont-Blanc, France and Merapi volcano, Indonesia, with different types of change (i.e., seasonal evolution, glaciers, volcanic eruption, etc.). Observations of these test-sites are acquired on four SAR image time series from single polarization to full polarization, from medium (∼20 m) resolution to high (∼8 m), very high (∼2 m) resolution, i.e., Sentinel-1, ALOS-PALSAR, RADARSAT-2 and TerraSAR-X time series.

4.1 Study areas

4.1.1 Chamonix Mont-Blanc

Chamonix Mont-Blanc test-site is located at the heart of the french Alps, in the Haute-Savoie department in the Rhône-Alpes region, south-eastern France. This test-site, a part of Mont-Blanc massif, is a heterogeneous area with mountainous terrain including alpine glaciers (i.e., Argentière, Mer-de-Glace, Leschaux, Tacul,

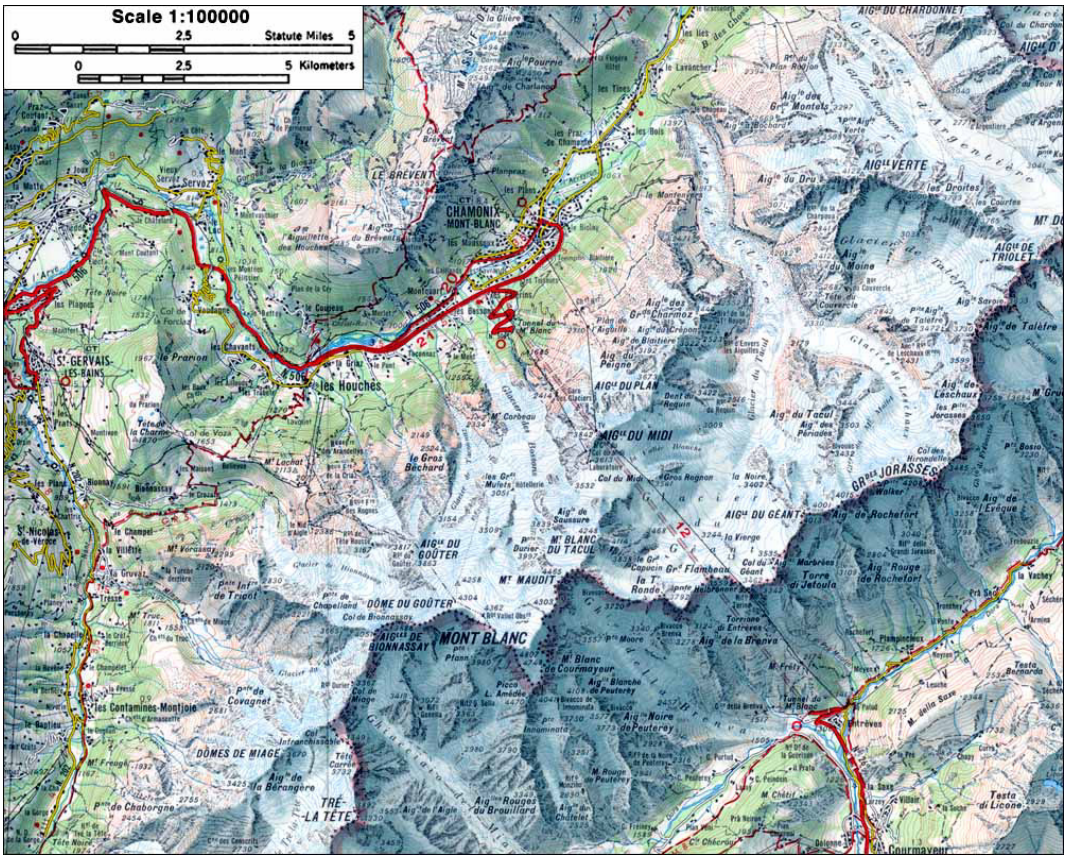

(a) Chamonix Mont-Blanc topographic map

(b) Google Earth image

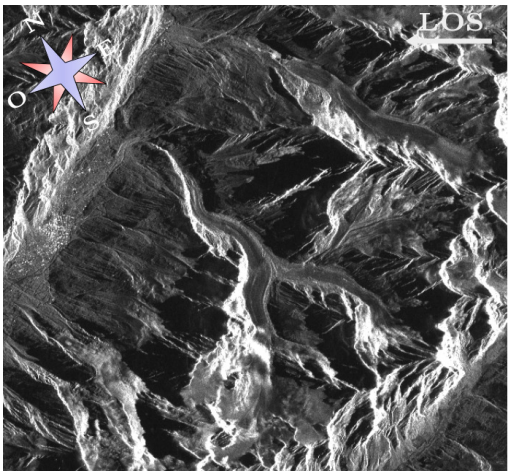

(c) Sentinel-1 image

Figure 4.1: Chamonix Mont-Blanc test-site. (a) 1:100,000 scale topographic map of Chamonix Mont-Blanc (©MAPPERY); (b) Google Earth image; (c) Amplitude image obtained by arithmetic mean of a time series of 11 Sentinel-1 images.

Bossons, Taconnaz), the Chamonix valley with some villages such as Les Bossons, Les Praz, Argentière, etc., the town of Chamonix and forested areas (see Fig. 4.1).

Many researches have been conducted for the monitoring of alpine glaciers [Berthier & Vincent 2012], [Vincent *et al.* 2014], [Pham 2015], etc., due to the fact that glaciers are an indicator of climate change. Associated with the climate change, in particular with the contemporary global warming that causes the retreat of glaciers, glacial risks for nearby human activities tend to increase, such as serac falls, breaks of subglacial water pockets, etc. Chamonix has a humid continental climate, with an average annual precipitation of 1,055 mm. Summers are mild and winters are cold and snowy. The Chamonix valley of this test-site has an average altitude about 1,000 m above the sea level and the Mont-Blanc summit, the top of Europe, is at 4,810 m elevation. In the Mont-Blanc massif, the temperature decreases from 0.33 to 0.91°C every 100 m in elevation. In this area, different types of change occur such as glacier surface evolution, progressive changes like seasonal change, i.e., the snow appears/disappears little by little on the forest and glacier surface, etc.

4.1.2 Merapi volcano

Indonesia is the country containing many volcanoes that are created due to the subduction zones between the Eurasian plate and the Indo-Australian plate. Merapi, located at 7° 32' 26" S and 110° 26' 48" E, is a volcano in the north of the Yogyakarta city in central Java, Indonesia (Fig. 4.2).

It is known as one of the most dangerous volcanoes worldwide due to its persistent eruptive activity and location within densely populated areas. The population density exceeds 1400 inhabitants per km^2 on the western and southern slopes of the volcano. Merapi has erupted regularly since 1548 producing periodic pyroclastic and lava flows. Small eruptions occur every two or three years and more important ones take place every ten to fifteen years, and at least seventeen eruptions have caused fatalities [Solikhin *et al.* 2015].

From October 26 to November 23, 2010, the largest eruption since 1872 occurred with numerous pyroclastic flows that traveled down the heavily populated slopes of the volcano, mostly to southeast, south and southwest. This violent eruption caused the greatest influence to human life with more than 200 direct deaths, 2200 damaged infrastructures, buildings, agriculture areas, etc., and over 400,000 evacuated people from the affected area [Surono *et al.* 2012], [Komorowski *et al.* 2013]. The volcanic ash clouded few km above the summit and went with the wind in the air, endangered health of people in surrounding cities and also caused major disruption to aviation across Java. In the experimental works of the thesis, we have used a time series of ALOS-PALSAR images involving some abrupt changes due to the explosive eruption in 2010.

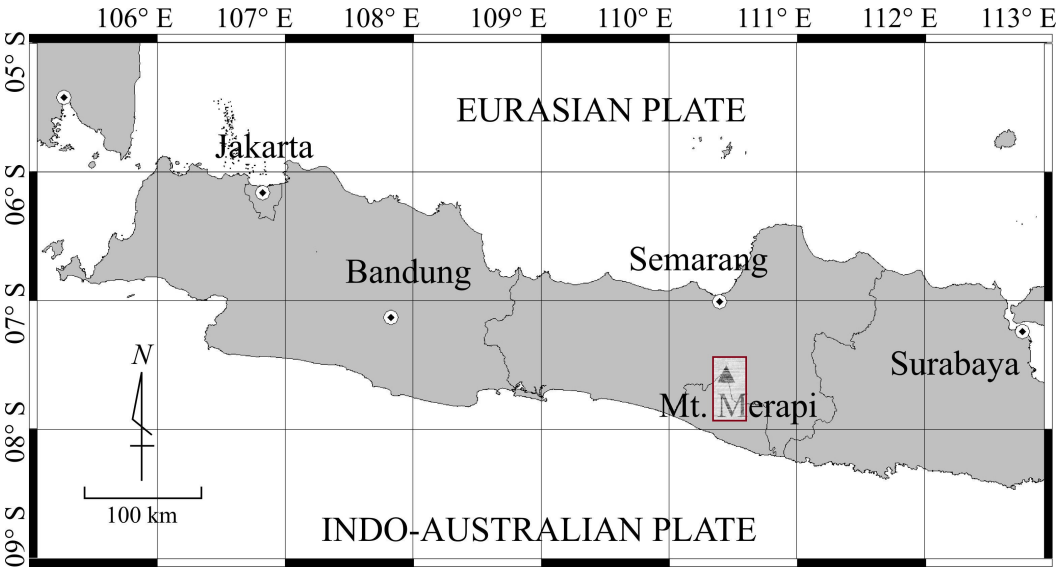

(a) Location of Merapi volcano

(b) ALOS-PALSAR image (Jun 16, 2010)

(c) ALOS-PALSAR image (February 01, 2011)

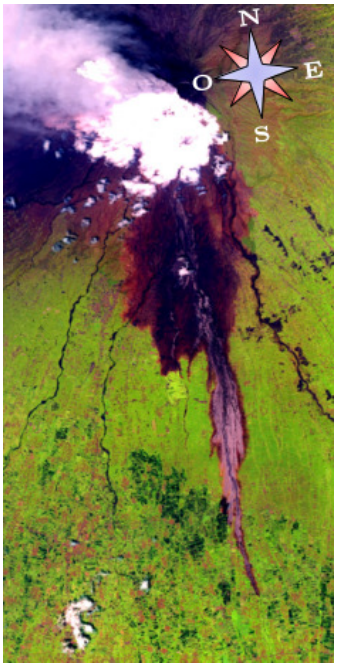

(d) SPOT-5 image (November 15, 2010)

Figure 4.2: Merapi volcano test-site. (a) Location of mount Merapi in central Java, Indonesia (©asepsaepuloh); (b), (c) Color composition ALOS-PALSAR ascending image on Jun 16, 2010 (before the 2010 eruption) and on February 01, 2011 (after the 2010 eruption) (R: C_{11}; G: $\mid C_{22} - 2C_{12\ real} + C_{11} \mid$; B: C_{22}; where $C_{i,j}$ are elements of the covariance matrix of dual-pol data); (d) SPOT-5 image on November 15, 2010 (during the 2010 eruption).

4.2 Datasets

The experimental works of the thesis will be performed on four datasets over the two test-sites mentioned above, with different characteristics: spatial, temporal resolution, wave band, polarization, etc., in order to illustrate the relevancy of the framework proposed in the thesis.

4.2.1 TerraSAR-X

4.2.1.1 TerraSAR-X mission

TerraSAR-X is a German SAR satellite mission for scientific and commercial applications which was launched on June 15, 2007 from the Russian Cosmodrome, Baikonur, Kazakhstan. The project is in collaboration between German Aerospace Center (DLR) and EADS Astrium GmbH. The technical aspects like satellite, the scientific data rights are owned and operated by DLR, while the exclusive commercial exploitation rights for this data is managed by EADS Astrium/Infoterra. TerraSAR-X is a Sun-synchronous dusk-dawn orbit satellite at an altitude of 514 km with a speed about 7.6 km/s. After a repeat cycle of 167 revolutions in 11 days, the satellite revisits a specific point on the Earth from almost of the same position (repeat-pass orbit). The satellite was designed to have 5 year lifetime, however until now (8 years passed) it is still in an excellent status and is expected to continue playing its role for further five years. Table 4.1 shows main parameters of TerraSAR-X satellite and sensor.

Table 4.1: Specifications of TerraSAR-X satellite and sensor.

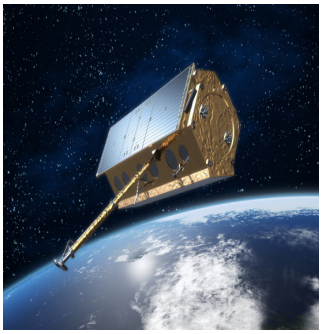

Orbit	Sun-synchronous repeat orbit
Repeat cycle	11 days
Inclination	97.44°
Altitude	514 km
Antenna size	4.78 m × 0.7 m × 0.15 m
Center frequency	9.65 GHz (X-band)
Chirp bandwidth	150 MHz / 300 MHz
Incidence angle	15° - 60°
Polarization	Single, Dual, Quad

The TerraSAR-X imaging sensor is an SAR system operating in the X band with three types of acquisition mode being possible: SpotLight, StripMap, and ScanSAR. It has the capability to acquire images in single and dual polarization, depending on imaging mode. Quad-polarization can be provided to users under "experimental mode" in limited periods depending on the consumption.

- The SpotLight imaging modes can technically cover a scene size of 10 km × 10 km (range × azimuth) for the basic SpotLight (SL) mode and 5 to 10 km × 5 km (range × azimuth) in the High Resolution SpotLight (HS) mode. In

the Staring SpotLight (ST) mode, the scene size is dependent on the incidence angle: 7.5 km × 2.5 km and 4 km × 3.7 km (range × azimuth) when incidence angles are respectively 20° and 60°. Acquired SAR images have resolutions that can be up to 0.25 m in ST mode, 1 m in HS and 2 m in SL mode (image acquired with a bandwidth of 300 MHz) in single or dual polarization.

- In StripMap (SM) mode, the scene size can be 30 km × 50 km (range × azimuth), up to 1,650 km length with spatial resolution of up to 3 m.

- ScanSAR (SC) imaging mode can achieve a swath width of 100 km by scanning four adjacent ground sub-swaths with four different incidence angles and a scene size of 100 km × 150 km (range × azimuth) can be scanned. While for Wide ScanSAR (WS), by scanning six adjacent ground sub-swaths, scene size can be 270 km × 200 km. Spatial resolutions for these two modes are 18.5 m and 40 m, respectively.

Different polarimetric data are accessible: the single polarization HH or VV is available for all acquisition modes, the dual polarization HH/VV is possible for spotlight (HS, SL) and SM modes, the dual polarization (HH, HV) or (VV, VH) are only available for SM. Whilst quadruple polarization (HH, VV, HV, VH) data recording the full scattering matrix can be acquired only for certain periods selected by DRL and Infoterra.

All categories of SAR raw data are processed by the TerraSAR-X Multi Mode SAR Processor (TMSP) in "radar brightness" β^0 before being provided to data users. The radar brightness β^0 format allows to compare TerraSAR-X data to the detected ground range products from ERS-1 and 2, ENVISAT/ASAR and RADARSAT. The four available TerraSAR-X Basic Image Products types are:

- Single Look Slant Range Complex (SSC): this is a single look product of the focused radar signal which provides amplitude and phase in complex numbers. This product is intended to applications requiring complex images without further processing, such as SAR polarimetry and interferometry.

- Multi look Ground range Detected (MGD): with this product, speckle is reduced by a multilook process and pixel spacing is equalized in azimuth and in ground range. The transformation from slant range to ground range is implemented by using the WGS-84 ellipsoid and the average altitude of the imaged scene.

- Geocoded Ellipsoid Corrected (GEC): like MGD product, GEC is a multilook detected product, projected to the WGS-84 ellipsoid with average height of the terrain. Besides that, this product is geocoded during a spatial resampling.

- Enhanced Ellipsoid Corrected (EEC): this product is GEC product with terrain correction by using a Digital Elevation Model (DEM). The EEC data are geometrically corrected, they thus enable to interpret and to combine with auxiliary data.

Detailed and further information of TerraSAR-X mission and data can be found in [AirbusDS 2014a].

4.2.1.2 TerraSAR-X time series

TerraSAR-X data used in this thesis is a time series of 25 SLC ascending images acquired from November 06, 2009 to September 14, 2011 with 2 m resolution and polarization HH over Chamonix Mont-Blanc test-site (Fig. 4.3a). The main characteristics of these images are presented in Table 4.2.

Table 4.2: TerraSAR-X data set description.

Specifications	**TerraSAR-X data set**
Operator/Manufacturer	DLR/EADS Astrium
Satellite launch date	June 15, 2007
Satellite orbit	Ascending
Incidence angle	45°
Repeat cycle	11 days
Imaging frequency	X-band at 9.6 GHz
Imaging mode	Strip map
Data product	Single Look Complex
Spatial resolution	2 m
Polarization	Single pol. HH
Test-site	Chamonix Mont-Blanc, France
Number of images	25 images
Acquisition dates (YY/MM/DD)	09/06/11; 09/06/22; 09/07/03; 09/07/14; 09/07/25; 09/08/05; 09/08/16; 09/08/27; 09/09/18; 09/09/29; 09/10/10; 09/10/21; 11/05/05; 11/05/16; 11/05/27; 11/06/07; 11/06/18; 11/06/29; 11/07/10; 11/07/21; 11/08/01; 11/08/12; 11/08/23; 11/09/03; 11/09/14.

This time series is a part of the 50 TerraSAR-X images acquired by LISTIC, GIPSA, LTCI, and IETR laboratories during the EFIDIR project thanks to the DLR TerraSAR-X Science Project MTH0232.

4.2.2 RADARSAT-2

4.2.2.1 RADARSAT-2 mission

RADARSAT-2 is an Earth Observation satellite jointly-funded by Canadian Space Agency and MacDonald Dettwiler Associates Ltd. (MDA). RADARSAT-2, follow-on RADARSAT-1 satellite mission, was launched on December 14, 2007. It retains all RADARSAT-1 modes, adds a fully polarimetric SAR mode, and also improves the ground range resolution (up to 3 m) for a single polarization mode. Like TerraSAR-X, RADARSAT-2 orbit is also Sun-synchronous on the dawn-dusk terminator, op-

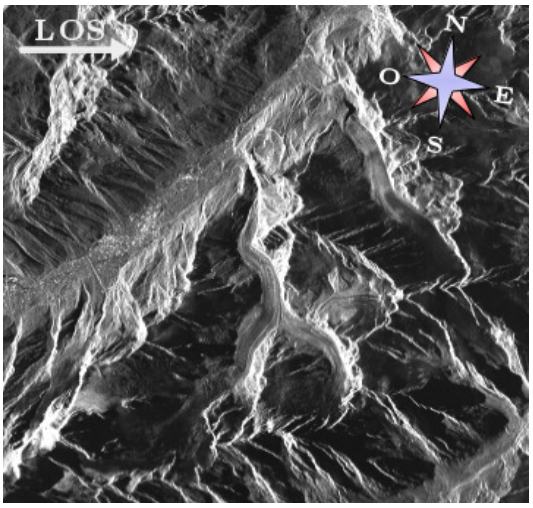

(a) TerraSAR-X ascending HH image

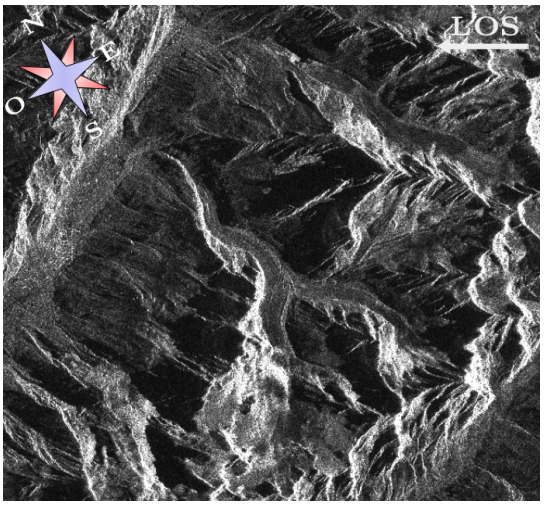

(b) Sentinel-1 descending VV image

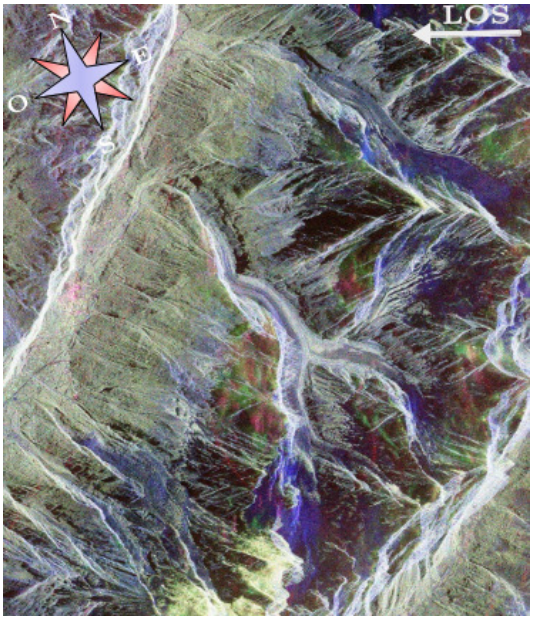

(c) RS-2 descending quad-pol image

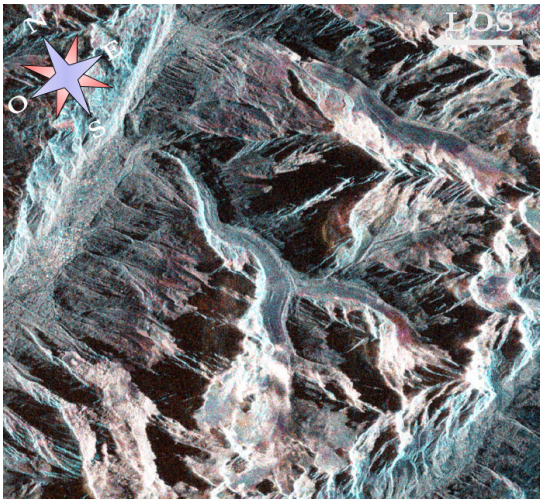

(d) Sentinel-1 descending dual-pol image

Figure 4.3: SAR data over Chamonix Mont-Blanc test-site. (a) TerraSAR-X ascending HH image on October 10, 2009; (b) Sentinel-1 descending VV image on March 15, 2015; (c) RADARSAT-2 descending quad-pol image on June 22, 2009 (Pauli basis, R: HH - VV, G: 2HV, B: HH + VV); (d) Sentinel-1 descending dual-pol image on March 15, 2015 (R: C_{11}; G: $\mid C_{22} - 2C_{12\ real} + C_{11} \mid$; B: C_{22}; where $C_{i,j}$ are elements of the covariance matrix of dual-pol data).

erating at an altitude of 798 km. The satellite flies about 14 orbits per day and has a repeat cycle of 24 days. With a designed life of 7.25 years, on December 14, 2014, RADARSAT-2 completed 7 years on orbit and it continues to operate

above its mission in most areas. The satellite carries a C-band (5.405 GHz) SAR system operating in one of three fundamental imaging sensor modes: single beam, scanSAR and spotlight. The RADARSAT-2 SAR sensor can transmit microwave signals on horizontal (H) or vertical (V) linear plane and receive either H or V polarized signals. Therefore, RADARSAT-2 can provide single co-polarization, single cross-polarization, dual-polarization and quad-polarization imaging. Table 4.3 shows the main parameters of RADARSAT-2 satellite and sensor and Fig. 4.4 and Table 4.4 give principal characteristics of acquisition modes.

Table 4.3: Specifications of RADARSAT-2 satellite and sensor.

Orbit	Sun-synchronous repeat orbit
Repeat cycle	24 days
Inclination	98.6°
Altitude	798 km
Antenna size	15 m × 15 m
Center frequency	5.405 GHz (C-band)
Bandwidth	100 MHz
Incidence angle	18° - 60°
Polarization	Single, dual, quad

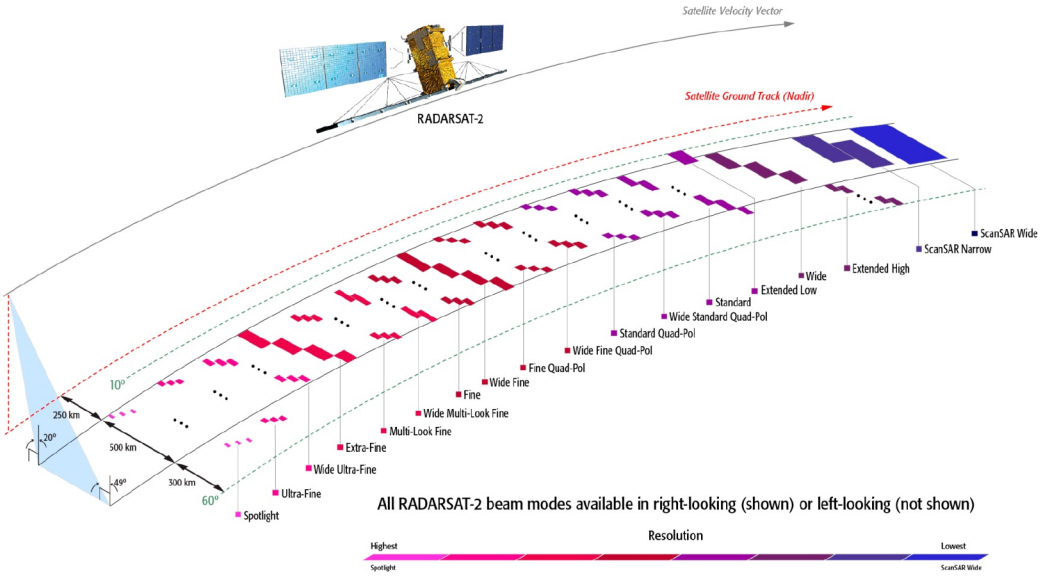

Figure 4.4: RADARSAT-2 acquisition modes (© [MDA 2014]).

From raw SAR data, three types of RADARSAT-2 products are available: Slant Range Single Look Complex, Ground Range (GR), and Geocorrected. In SLC products, each image pixel is represented by a complex value in slant range - azimuth plane. Pixel spacings are determined by the radar range sampling rate and pulse

Table 4.4: Characteristics of RADARSAT-2 acquisition modes.

Beam modes		Swath coverage (km)	Incidence angle range	Polarization	Nominal resolution of SLC products Rng (m) × Az (m)
Single beam	Standard	100 - 500	20° - 52°	HH or VV or HV or VH; HH/HV or VV/VH	9.0 or 13.5× 7.7
	Wide	130 - 170	20° - 45 °	HH or VV or HV or VH; HH/HV or VV/VH	13.5× 7.7
	Fine	50	30° - 50°	HH or VV or HV or VH; HH/HV or VV/VH	5.2× 7.7
	Wide Fine	120 - 170	20° - 45°	HH or VV or HV or VH; HH/HV or VV/VH	5.2× 7.7
	Multilook Fine	50	30° - 50°	HH or VV or HV or VH	3.1× 4.6
	Wide Multilook Fine	50 - 90	30° - 50°	HH or VV or HV or VH	3.1× 4.6
	Extra Fine	108 - 160	22° - 49°	HH or VV or HV or VH	3.1× 4.6
	Ultra Fine	20	30° - 50°	HH or VV or HV or VH	1.6× 2.8
	Wide Ultra Fine	50	30° - 50°	HH or VV or HV or VH	1.6× 2.8
	Extended High (High Incidence)	70 - 80	49° - 60°	HH	13.5× 7.7
	Extended Low (Low Incidence)	170	10° - 23°	HH	9.0× 7.7
	Standard Quad-Polarization	25	18° - 49°	HH/VV/HV/VH	9.0 or 13.5× 7.6
	Wide Standard Quad-Polarization	50	18° - 42°	HH/VV/HV/VH	9.0 or 13.5× 7.6
	Fine Quad-Polarization	25	18° - 49°	HH+VV+V+VH	9.0 or 5.2× 7.4
	Wide Fine Quad-Polarization	50	18° - 42°	HH/VV/HV/VH	9.0 or 5.2× 7.6
ScanSAR	ScanSAR Narrow	300	20° - 47°	HH or VV or HV or VH; HH/HV or VV/VH	81 - 38× 60
	ScanSAR Wide	3450 - 500	20° - 49°	HH or VV or HV or VH; HH/HV or VV/VH	163 - 73× 100
SpotLight		18	20° - 50°	HH or VV or HV or VH	1.6× 0.8

repetition frequency (PRF). Polarization channels of dual or quad polarization SLC products are coregistered. In the GR products, each pixel is an unsigned integer, i.e, magnitude detected pixels. The interpolation from image coordinates into ground range coordinates is based on the selected ellipsoid in the Production Order at a local elevation height. There are various types of GR product for different acquisition modes which can be consulted in [MDA 2014]. In Geocorrected type, we have SAR System Geocorrected (SSG) products and SAR Precision Geocorrected (SPG) products. With SSG product, image is corrected to a map projection, while ground control points are additionally used to improve positional accuracy in SPG products.

4.2.2.2 RADARSAT-2 time series

RADARSAT-2 data used in this thesis is a time series of 7 descending fine-quad polarization images acquired from January 29, 2009 to Jun 22, 2009 with 8 m resolution. The data also cover the Chamonix Mont-Blanc test-site (Fig. 4.3 (c)). Images were acquired by LISTIC and GIPSA laboratories within the EFIDIR project

thanks to the SOAR project 3399. The main characteristics of these images are presented in Table 4.5.

Table 4.5: RADARSAT-2 data set description.

Specifications	**RADARSAT 2 data set**
Operator/Manufacturer	MDA/CSA
Satellite launch date	December 14, 2007
Satellite orbit	Descending
Incidence angle	32°
Repeat cycle	24 days
Imaging frequency	C-band at 5.405 GHz
Beam mode	Fine Quad Polarization
Data product	Single Look Complex
Spatial resolution	9.0 m × 7.4 m (range × azimuth)
Polarization	Full pol. HH/HV/VH/VV
Test-site	Chamonix Mont-Blanc, France
Number of images	07 images
Acquisition dates (YYYY/MM/DD)	2009/01/29; 2009/02/22; 2009/03/18; 2009/04/11; 2009/05/05; 2009/05/29; 2011/06/22

4.2.3 ALOS-PALSAR

4.2.3.1 ALOS-PALSAR mission

The Advanced Land Observing Satellite (ALOS) was launched on January 24, 2006 by the Japan Aerospace and Exploration Agency (JAXA). ALOS completed its operation on May 12, 2011. The satellite carried three remote sensing instruments: the Panchromatic Remote-sensing Instrument for Stereo Mapping (PRISM), the Advanced Visible and Near-Infrared Radiometer type 2 (AVNIR-2), and the polarimetric Phased Array L-band Synthetic Aperture Radar (PALSAR) which is in focus in this section. ALOS had the Sun-synchronous orbit at 691.65 km altitude, 98.16° inclination, and had about 14 revolutions per day around the Earth. The repeat cycle to revisit a same scene was 46 days. The PALSAR was a right-looking SAR using L-band frequency (at 1.3 GHz) with 8° to 60° incidence angle range.

PALSAR had the three following observation modes: High resolution, ScanSAR and Polarimetry modes.

- High resolution: This is the most commonly used mode for regular operation. In this mode, the swath width covers a scene size of 40 - 70 km with an incidence range of 8° - 60°. Single and dual polarizations are available for this

Table 4.6: Specifications of ALOS satellite and PALSAR sensor.

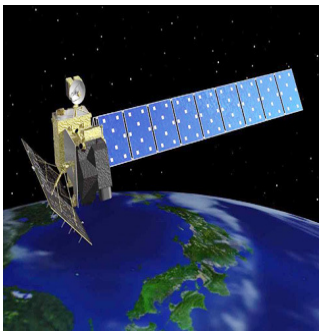

Orbit	Sun-synchronous repeat orbit
Repeat cycle	46 days
Inclination	98.16°
Altitude	691.65 km
Antenna size	3.1 m × 8.9 m (height × length)
Center frequency	1.27 GHz (L-band)
Chirp bandwidth	14 MHz / 28 MHz
Incidence angle	8° to 60°
Polarization	Single, Dual, Quad

mode, in which the single polarization (HH) images has the resolution of 7 m - 44 m × 10 m (in range × azimuth), and dual polarization (HH/HV) or (VV/VH) images has medium resolution of 14 - 88 m × 20 m.

- ScanSAR mode: In this mode, radar beam scans the swath of about 70 km and covers a wide area from 250 km to 350 km with an incidence range of 18° - 43°. Only single polarization HH was available for this mode, and ground resolution was low (71 m - 157 m × 94 m - 100 m, range × azimuth).

- Polarimetry mode: This mode enables quad-polarization simultaneous observation. This is an experimental mode, the operation time is limited due to power consumption. The ground resolution is 24 - 89 m × 20 m with 20 - 65 km swath width in an incidence range of 8° - 30°.

PALSAR products consist of 5 processing levels:

- Level 1.0 Product is the raw data of ALOS-PALSAR observation modes after detecting systematic errors and performing a basic processing of byte-unit arrangements, etc.

- Level 1.1 Product is SLC image of each observation mode except for ScanSAR mode. Each image pixel is a complex value on slant range image plane.

- Level 1.5 Product is the product of High resolution mode by single polarization. At this processing level, images are multi-look processed and slant range coordinates are converted into ground range coordinates. The products can be either Geo-referenced or Geo-coded products processed at sea level.

- Level 4.1 Product: In this level, we have product categories like in level 1.5 but for High resolution mode of dual polarization or the product of Polarimetry mode.

- Level 4.2 Product is the product of ScanSAR mode.

Detailed information of ALOS-PALSAR data can be consulted in [J-SS 2012].

4.2.3.2 ALOS-PALSAR time series

Since full polarization images are not so often available, we also use a dual polarization dataset for the experimental works of the thesis. The time series includes 11 ascending ALOS-PALSAR images with resolution of 23 m and polarization HH and HV. The images in this series are acquired from June 08, 2007 to February 01, 2011 on Merapi volcano test-site, Indonesia. In this acquisition period, on October 25, 2010, Merapi volcano erupted pyroclastic, lava flows and remained eruptive activity until the end of November, 2010. This time series has images involving this event, i.e., 9 images before the eruption (from June 08, 2007 to September 16, 2010), 1 image during the eruption (November 01, 2010) and 1 image after the event (February 01, 2011.) (see Fig. 4.2 (b), (c) and Table. 4.7). The time series was acquired by the ISTerre laboratory thanks to the project no. 1188 of JAXA.

Table 4.7: ALOS - PALSAR data set description.

Specifications	**ALOS - PALSAR data set**
Manufacturer	JAXA
Satellite launch date Operation completed date	January 24, 2006 May 12, 2011
Satellite orbit	Ascending
Incidence angle	34.3°
Repeat cycle	46 days
Imaging frequency	L-band at 1.27 GHz
Beam mode	High resolution Double Polarization
Data product	Single look complex (Level 1.1)
Spatial resolution	33.2 m × 28.4 m (range × azimuth)
Polarization	Dual pol. HH/HV
Test-site	Merapi volcano, Indonesia
Number of images	11 images
Acquisition dates (YYYY/MM/DD)	- Before the eruption: 2007/06/08; 2007/09/08; 2008/04/25; 2008/06/10; 2008/07/26; 2008/09/10; 2009/06/13; 2010/06/16; 2010/09/16. - During the eruption: 2010/11/01. - After the eruption: 2011/02/01.

4.2.4 Sentinel-1

4.2.4.1 Sentinel-1 mission

Sentinel-1 is the European Radar Observatory designed and developed by European Space Agency (ESA) and funded by the EC (European Commission) within the

Global Monitoring for Environment and Security (GMES) Space Component program. Sentinel-1 is composed of a constellation of two satellites, Sentinel-1A and Sentinel-1B, moving on the same orbital plane with 180° phasing apart. Sentinel-1A was launched on April 03, 2014 from Europe's Spaceport in French Guiana, and the lunch of Sentinel-1B is scheduled in 2016. Inherited and developed from SAR systems on ERS-1, 2 and Envisat, Sentinel-1 mission aims at providing independent operational capability for primarily medium- to high-resolution radar mapping of the Earth with enhanced temporal resolution, coverage, reliability for applications requiring long time series. Each Sentinel-1 satellite has a designed lifetime of 7 years and has a near-polar Sun-synchronous orbit at 693 km altitude, 98.18° inclination with 12 day repeat cycle (175 orbits per cycle) and 6 days with the lunch of Sentinel-1B satellite in 2016.

Sentinel-1 SAR sensor operates at same C-band frequency (5.405 GHz) as the Canadian RADARSAT-2, and supports operation in single (HH or VV) and dual polarizations (HH/HV, VV/VH). Sentinel-1 uses the four following observation modes:

- Stripmap (SM) mode acquires images of 5 m × 5 m spatial resolution (single look) over a narrow swath width of 80 km with incidence angle range of 18.3° - 46.8°. This acquisition mode provides only single polarization HH or VV.

- The Interferometric Wide swath (IW) mode is the default acquisition mode. It scans a large swath width of 250 km on the ground with incidence angle range of 29.1° - 46.0°, including three sub-swaths using Terrain Observation with Progressive Scans SAR (TOPSAR) technique. Acquired images of the mode have medium geometric resolution (5 m × 20 m in range × azimuth) and can be single (HH or VV) or dual (HH/HV or VV/VH) polarization.

- Extra Wide Swath (EW) mode operates similar to IW mode but it uses five sub-swaths in order to cover a wider area on the ground (over a 400 km swath) with incidence angle range of 18.9° - 47.0°. This results in a lower resolution (20 m × 40 m). Images of this acquisition mode are suitable for the monitoring of objects over a global scale, for instance, sea-ice, polar zones and certain maritime areas, etc.

- Wave mode alternately acquires data of SM mode in 20 km × 20 km vignettes on two different incidence angles (23° and 36.5°). Vignettes are acquired for every 100 km along the orbit and separated by 200 km on the same incidence angle. The Wave mode acquisitions are useful for ocean studies in additional with global ocean wave models. VV polarization is the default mode for acquiring data over open ocean.

Table 4.8 shows main parameters of Sentinel-1A satellite and sensor.
Sentinel-1 SAR includes four product types at three processing levels:

- Level-0 products are compressed and unfocused SAR raw data and additional information including noise, internal calibration and echo source packets as well as orbit and attitude information.

Table 4.8: Specifications of Sentinel-1A satellite and sensor.

Orbit	near-polar Sun-synchronous repeat orbit
Repeat cycle	12 days
Inclination	98.18°
Altitude	693 km
Antenna size	12.3 m × 0.821 m
Center frequency	5.405 GHz (C-band)
Incidence angle	20° - 46°
Polarization	Single, Dual

- Level-1 products: Raw SAR data is focused in slant-range geometry to obtain Level-1 Single-Look Complex products (SLC). Then SLC data is detected, multilooked and projected to ground range plane using an Earth ellipsoid model and specified terrain height to produce Level-1 Ground Range Detected (GRD) products.

- Level-2 products are obtained by geocoding Level-1 products. Level-2 Ocean products may contain the following geophysical components derived from the SAR data: Ocean Wind field (OWI), Ocean Swell spectra (OSW) and Surface Radial Velocity (RVL) [ESA 2015].

4.2.4.2 Sentinel-1 time series

Sentinel data are made available recently and free of charge to all data users. We have started to collect ascending and descending images over the Chamonix Mont-Blanc test-site (cf. Fig. 4.5). In this thesis, we exploit time series of 11 descending IW Level-1 SLC Sentinel-1 SAR images acquired from November 15, 2014 to March 15, 2015 over a crop area on Chamonix Mont-Blanc, France in single polarization (Fig. 4.3 (b)) and dual polarization (Fig. 4.3 (d)). Table 4.9 shows the principal parameters of the dataset.

4.3 SAR data preprocessing

A SAR image time series can be taken from varying observations with different recording parameters, or from repetitive orbit positions. For SAR images which are very sensitive to the local incidence angle, we usually prefer to analyze time series acquired from repeat-pass orbits. In order to make images in a time series comparable, some preprocessing steps such as radiometric calibration, coregistration and geometric correction, etc., should be performed before carrying out any specific analysis.

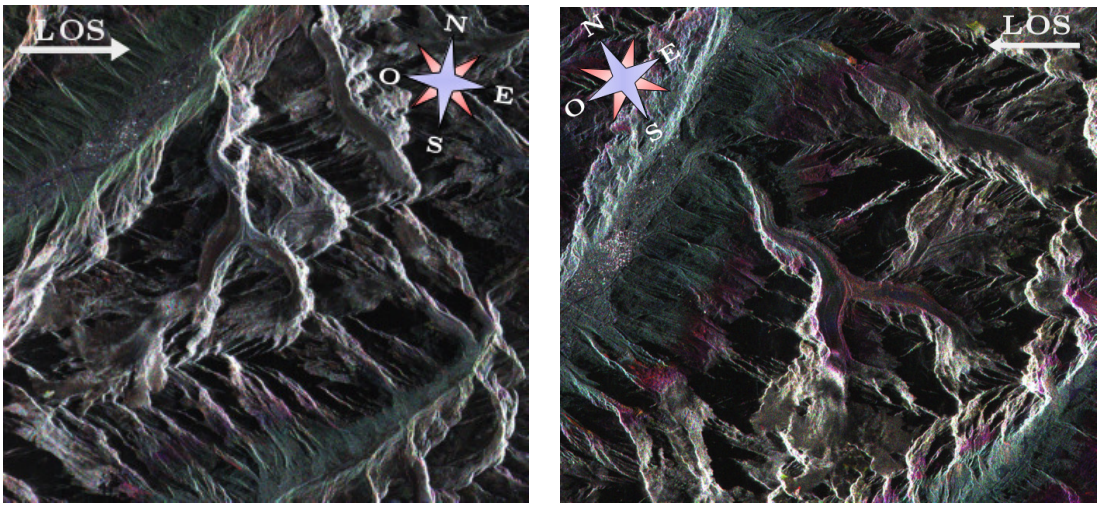

(a) Sentinel-1 ascending image (b) Sentinel-1 descending image

Figure 4.5: Color composition of Sentinel-1 images over Chamonix Mont-Blanc test-site. (a) Sentinel-1 ascending image (R: 2015/01/27; G: 2014/12/22; B: 2014/12/10); (b) Sentinel-1 descending image (R: 2014/12/09; G: 2014/11/27; B: 2014/11/15).

Table 4.9: Sentinel-1 dataset description.

Specifications	**Sentinel-1 dataset**
Operator/Manufacturer	European Space Agency (ESA)
Satellite Launched date	Sentinel-1A April 03, 2014
Satellite orbit	Descending
Incidence angle	43.1°
Repeat cycle	12 days
Imaging frequency	C-band at 5.405 GHz
Imaging mode	IW
Data product	SLC Level-1
Resolution	5 m × 20 m (range × azimuth)
Polarization	Single -pol (VV) and dual-pol (VV/VH)
Test-site	Chamonix Mont-Blanc, France
Number of images	11 images
Acquisition dates (YYYY/MM/DD)	2014/11/15; 2014/11/27; 2014/12/09; 2014/12/21; 2015/01/02; 2015/01/14; 2015/01/26; 2015/02/07; 2015/02/19; 2015/03/03; 2015/03/15.

4.3.1 Radiometric calibration

The objective of SAR radiometric calibration is to calculate backscattering coefficients of the targets in the scene. Hence, using the SAR calibrated images, radar backscattering coefficient of the reflecting surface (represented in digital number at each pixel) can be extracted, or images acquired with different sensor or from the same sensor with different incidence angles, ascending/descending orbits and opposite look directions, etc. become comparable.

The radiometric calibration is based on the radar equation that relates the important parameters affecting the received signal of radar. As mentioned in Section 2.1.3, backscattering coefficients are the normalized radar backscatter by a unit area. The unit area can be taken on the ground, then the calculated backscattering coefficient is σ^0 ("sigma nought") - the normalized RCS, or in the slant range plane, the backscattering coefficient is β^0 ("beta nought") - the radar brightness, or in the plane perpendicular to the slant range direction - γ^0 ("gamma nought"). Through practically calibrated values (σ^0 or β^0 or γ^0), the radiometric calibration corrects the following radiometric distortions:

- The normalization area: the area for converting image pixel values to normalized backscater values may be distorted due to varying terrain heights.
- The range spreading loss: the signal attenuation when the signal propagates from the emitter to the target and back to the receiver is compensated.
- The antenna gain pattern: the change in the antenna gain is corrected in calibrated backscattering coefficient as a function of the local incidence angle.

To perform a full correction of antenna gain pattern and illuminated area, it is necessary to use topographic information (e.g., a DEM of the imaged scene). The detailed algorithms of TerraSAR-X, RADARSAT-2, ALOS-PALSAR and Sentinel-1 product calibrations can be found in [AirbusDS 2014b], [RADARSAT 2004], [Lavalle & Wright 2009] and [Miranda & Meadows 2015], respectively.

In the time series used in this thesis, we rely on the initial calibration performed by the space agencies for the SLC products. No DEM dependent calibration is performed, but this has a limited impact since these time series are collected from repeat-pass orbits (same incidence angle).

4.3.2 Coregistration

Coregistration of a SAR image time series is the alignment of SAR images in the time series. This process ensures that all images in the time series are in a same coordinate system, and pixels, associated to the same position on the ground, of the corresponding images are stacked. The objective of coregistration is to find a geometric transformation between images to be coregistered which maximizes the similarity degree of corresponding pixels in the time series [Tupin *et al.* 2014]. The types of transformation may consist of: linear transformations including rotation,

scaling, translation, and other affine transforms; and perspective, global polynomial transforms counting distortions when projecting a 3-D model of the scene on the images.

SAR images of datasets used in this thesis are acquired from repetitive orbits of the satellites. The coregistrations of these time series, thus, require only image translation for the proposed applications. For each time series, the similarity measure used for matching the reference image (any selected image in the series, e.g., the first image) and target images (other images in the time series to be registered according to the reference image) is the Zero mean Normalized Cross-Correlation (ZNCC) [Fallourd 2012].

At the Chamonix Mont-Blanc test-site, two corner reflectors (CR) have been installed on a moraine block and a stable rock on June 25, 2015 and on November 07, 2014, respectively. They have the size of 70 and 200 cm respectively and are oriented according to descending orbit of Sentinel-1 satellite. In Fig. 4.6, we can see clearly the CR imaged on Sentinel-1 data. CR points on SAR images can be used for the coregistration as sharp, easily recognizable points to enhance the accuracy of the automatic point matching by ZNCC measure. When there are many sharp points on the ground, CR points can be used as the control points to check the accuracy of the coregistration of the time series.

4.3.3 Geometric correction

Geometric correction is the process of minimizing geometric distortions from a distorted image due to position and attitude changes of satellite, the variation in sensor mechanics, viewing geometry, topographic effect, etc. The process determines the relationship between the image coordinate system and the geographic coordinate system. For SAR geometric correction, the conversion of a slant-range SAR image into a map coordinate requires topographic data (e.g., coordinates of ground control points, digital contours or DEM) and associated data about satellite orbit. Geometric correction consists of different levels:

- Rectification (also known as georeferencing): is the process of geometrically rectifying SAR image to a map projection in order to make the image planimetric [Schowengerdt 2007].

- Orthorectification uses elevation data to correct terrain distortion, hence, SAR image is corrected both for side-looking viewing geometry and effects of high-relief terrain.

Orthorectified SAR data, after eliminating (or minimizing) geometric distortions and geocoding errors, thus can be a reliable source for the integration into geographic information system (GIS).

SAR images used in the thesis are preprocessed by the two first steps which are adequate for time series analysis. However, the experimental results can be geocoded, by SAR-LUT tool [Petillot 2008] of EFIDIR project for instance. Besides

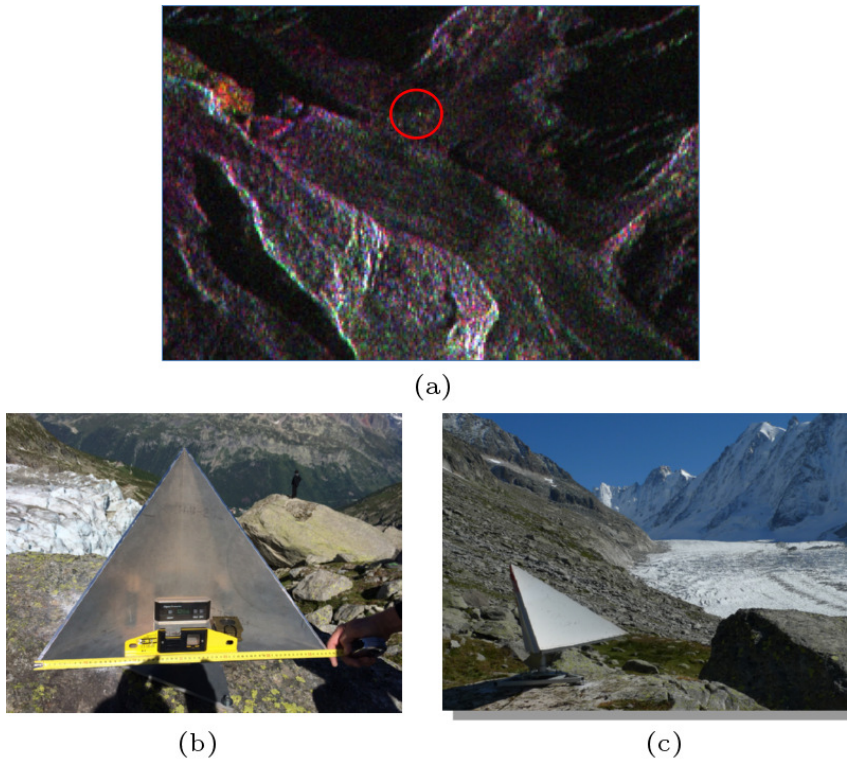

Figure 4.6: Corner reflector (CR) imaged on descending Sentinel-1 data over Argentière glacier. (a) Sentinel-1 descending image (R: 2015/01/27; G: 2014/12/22; B: 2014/12/10); (b) Installation of the CR at a moraine block on 2015/06/25 with the size of 70 cm; (c) the CR at stable on 2014/11/07 with the size of 200 cm, descending oriented.

that, PolSARpro software is used for reading ALOS-PALSAR data and Sentinel-1-Toolbox is used for the TOPSAR deburst step of Sentinel-1 data.

4.4 Conclusions

We have presented in this chapter the two test-sites and the four datasets which will be used in the experimental works. These test-sites are heterogeneous areas with high relief terrain and many kinds of change. The introduced datasets are diverse, with different acquisition modes (SAR amplitude, polarimetry, different bands, etc.), acquisition conditions (ascending and descending orbits, different viewing angles, etc), resolution (medium, high, very high), etc. We have also presented the satellite missions, the parameters, the characteristics, etc., of each data in order to understand the advantages and limitations of the data. The data preprocessing is an important step in the data processing chain. This step includes the radiometric calibration, the coregistration and the geometric correction. The heterogeneous

study areas, the variety of data used can illustrate the relevancy of the methodology proposed in the next chapters of this thesis.

Chapter 5

Change detection matrix

Contents

In this chapter, we propose a methodological framework for the analysis of SAR image time series. The proposed approach can give a response to the problem of effectively exploiting the diverse SAR image database with different acquisition modes (SAR amplitude, polarimetry, different bands, etc.), and acquisition conditions (ascending and descending orbits, different viewing angles, etc). The construction, implementation, properties and potentials of the proposed *"Change Detection Matrix"* will be presented respectively in the following sections.

5.1 Problem formulation

The development of applied sciences and sensor technologies makes it possible to acquire SAR images with high spatial and temporal resolutions. A large amount of such data is now available for studies on many regions of interest on the Earth. Effective exploitation of large information provided by SAR image time series to benefit the advantages of these data is a challenging issue for analysts and method developers.

Time series made of SAR images taken from the same scene at different acquisition times open new opportunities for observing changes on the Earth surface to understand its behavior and to predict its trends. Features showing temporal variation compared to their surroundings can, indeed, be mapped from multitemporal data. The demand for change detection is to identify where and when the change occurs, the duration and the type of change, etc. With the improvement of spatial resolution of SAR images from new generation satellites, these data are becoming a

reliable source of information for up-to-date geographic data into the GIS. Therefore, besides the task of monitoring, the results of change detection can also be used for updating existing landuse/landcover maps, inserting changed topographic objects into the GIS.

Detection of changes of specific features between two or more time periods using SAR data has to deal with a complex processing of this data and the presence of speckle. This is one of important problems of SAR data which makes it difficult for both human and automatic change detection and interpretation. Most multitemporal filtering approaches have an assumption that pixels at a same spatial location remain unchanged over the time [Quegan *et al.* 2000], [Coltuc *et al.* 2000], [Ciuc *et al.* 2001]. All of the pixels at the same spatial coordinate in the time series then can be involved in the filtering process (averaging intensity/amplitude values, for instance). This can be acceptable for some cases such as homogeneous fields, permanent scatterers (constructions, buildings), etc., in short periods. However, it is not true for heterogeneous time varying regions, in particular, with a long time series. This assumption is not appropriate with the fact that the ground features are not stable in all images of the time series. By this way, the presence of changes in the time series is not taken into account in the filtering process and may lead to the radiometric, spatial and temporal degradation of filtered values.

In general, it lacks in the literature a method for simplifying the analysis of multitemporal SAR data. Such method should benefit from the advantages of repeated SAR acquisitions and be able to process different kinds of SAR data (i.e. single, multipolarization SAR, etc.) for various applications. In this context, we propose in this thesis a general framework based on a spatio-temporal information matrix called *Change Detection Matrix* (CDM). This matrix should reveal temporal neighborhoods which are adaptive to changed and unchanged areas thanks to similarity cross tests.

The following sections will introduce the CDM approach and its properties and potentials to apply to different tasks.

5.2 Change detection matrix constructing method

To determine changed and unchanged pixels in SAR image time series, we propose constructing a change detection matrix (CDM) containing the information on responses of similarity cross tests between each pair of dates.

We consider an N-length cocalibrated and coregistered SAR/PolSAR image time series $\mathcal{I} = \{\mathcal{I}_t\}_{1 \leqslant t \leqslant N}$, where $\mathcal{I}_t$ denotes the image acquired at time t. Each pixel $\mathcal{I}_t(i,j)$ of image $\mathcal{I}_t$ can have an amplitude/intensity value of a single channel SAR image or be characterized by a covariance/coherency matrix of PolSAR image. Let $\mathcal{I}_t^w(i,j)$ be the analysis window which determines the spatial neighborhood of $\mathcal{I}_t(i,j)$. Let $\{\mathcal{I}_t(i,j)\}_{1 \leqslant t \leqslant N}$ be a vector including all values of pixels at spatial position (i,j), called *pixel pile*.

For each pixel pile at a given position (i,j), the proposed change detection matrix

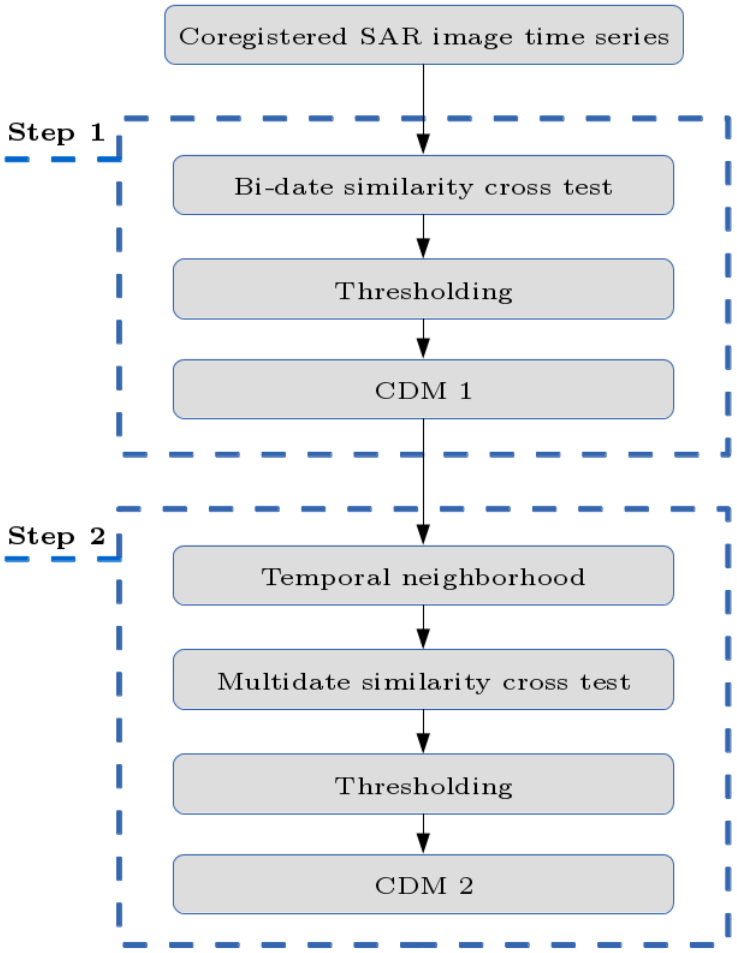

Figure 5.1: CDM construction strategy.

is built in a strategy including two steps (Fig. 5.1):

- The first step is a bi-date analysis: In this step, similarity tests are computed between each two dates using spatial windows to derive a change detection matrix (CDM 1). This matrix contains all the responses of similarity tests which determine changed and unchanged pixels corresponding to each reference date.

- The second step is a multidate analysis: Based on the result of the first step, similarity tests are computed between all the unchanged pixels identified in CDM 1 corresponding to each two dates in the pixel pile. The result of this step is another change detection matrix (CDM 2) which provides us with changed and unchanged pixels more accurately.

5.2.1 Bi-date analysis

Considering pixel spatial location (i, j) observed in two different dates $t, \ell \quad (1 \leqslant t, \ell \leqslant N)$, similarity tests are taken between each two temporal sample $\mathcal{I}_t(i, j)$ and $\mathcal{I}_\ell(i, j)$ using a spatial window w. Let

$$K^w_{t,\ell}(i, j) = \mathfrak{D}\left(\mathcal{I}^w_t(i, j), \mathcal{I}^w_\ell(i, j)\right) \tag{5.1}$$

denotes a similarity degree between $\mathcal{I}_t(i, j)$ and $\mathcal{I}_\ell(i, j)$ with $\mathfrak{D}$, a similarity measure. To decide whether $K^w_{t,\ell}(i, j)$ represents noise only or contains some change information, it is compared to a threshold λ. The change information is thus determined through a similarity test as follows:

$$M^w_{t,\ell}(i, j) = \left[K^w_{t,\ell}(i, j) \underset{1}{\overset{0}{\lessgtr}} \lambda\right]. \tag{5.2}$$

Matrix M called Change Detection Matrix 1 (CDM 1) is a N×N symmetric matrix containing 0 and 1 values representing "unchanged" and "changed" pixels, respectively.

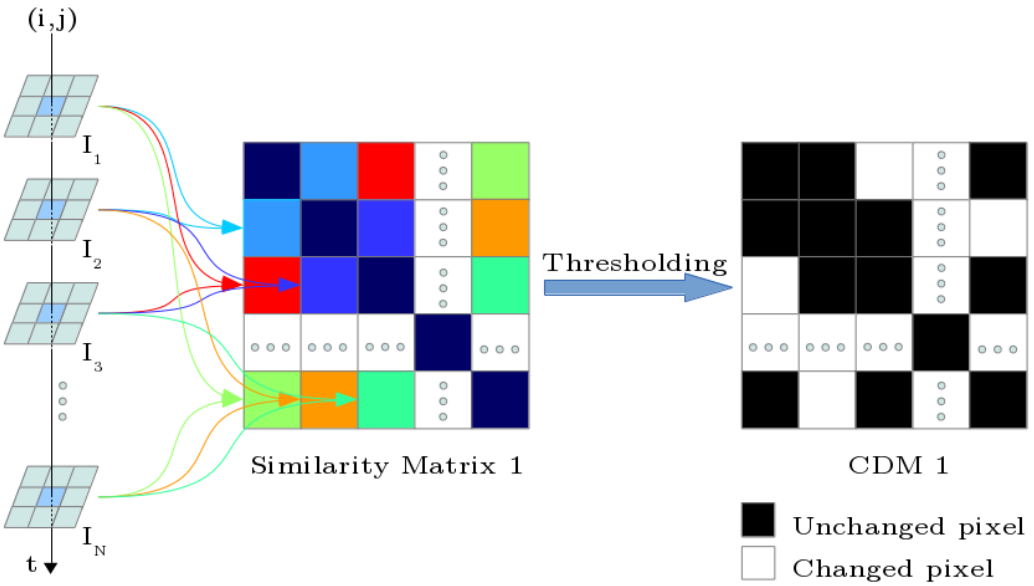

Figure 5.2: CDM 1 construction - Bi-date analysis.

Fig. 5.2 shows the construction of CDM 1. This matrix provides initial change detection results of the time series between each two dates. From this, similar temporal samples of the whole time series can be identified for the next step.

5.2.2 Multidate analysis

In order to refine the result of changed and unchanged pixel determination in each pixel pile derived from step 1 (bi-date analysis), we reconsider the similarity test given above in a multidate framework. All unchanged pixels determined in CDM 1 corresponding to each date are used to build multitemporal neighborhoods. Indeed, from CDM 1, for every pixel $\mathcal{I}_t(i,j)$, we obtain a set of elements having in their close spatial neighborhood the same statistical properties as $\mathcal{I}_t(i,j)$ with respect to $\mathfrak{D}$ and λ in the similarity test (5.2) as:

$$\Psi(\mathcal{I}_t^w(i,j)) = \{\mathcal{I}_k(i,j) \mid M_{t,k}^w(i,j) = 0; k = 1 \cdots N\}. \tag{5.3}$$

The similarity tests between each two dates are revised using corresponding temporal neighborhoods to obtain more accurate change detection results as follows:

$$\hat{K}_{t,\ell}^w(i,j) = \mathfrak{D}\left(\Psi\left(\mathcal{I}_t^w(i,j)\right), \Psi\left(\mathcal{I}_\ell^w(i,j)\right)\right) \tag{5.4}$$

$$\hat{M}_{t,\ell}^w(i,j) = \left[\hat{K}_{t,\ell}^w(i,j) \underset{1}{\overset{0}{\lessgtr}} \lambda\right]. \tag{5.5}$$

Matrix $\hat{M}$ is called Step 2 Change Detection Matrix (CDM 2) which contains more accurate change detection results of the time series than CDM 1.

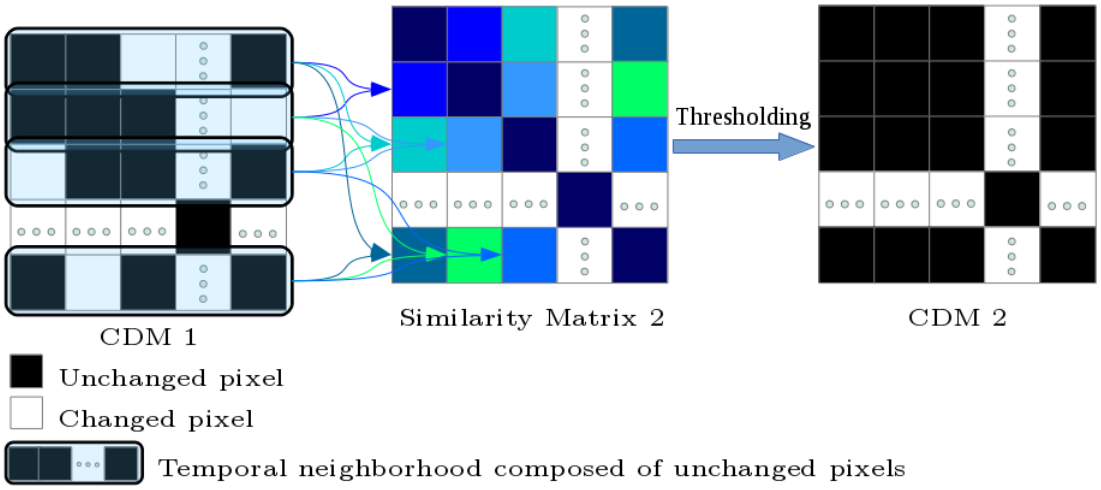

Figure 5.3: CDM 2 construction - Multidate analysis.

The construction of CDM 2 is shown in Fig. 5.3. The changed and unchanged information identified in CDM 2 is extracted from SAR image time series after a two-step strategy. This provides reliable information on changed and unchanged pixels within each pixel pile, which is exploited in different applications in the next parts of the thesis.

5.3 Implementation and properties of CDM

5.3.1 Implementation of CDM

The most critical point for implementing the proposed method is the selection of an appropriate similarity measure $\mathfrak{D}$ and the threshold λ. This depends on such main factors as the type of SAR images, the scale and characteristics of the study area, the availability of ground truth and user's need. The user's need or the requirement of researches decides the nature of change analysis and the scale of the study area, therefore affecting the selection of suitable spatial resolution of available SAR data. After the determination of work scale and data used, we can choose a similarity measure and a threshold taking into account also the accuracy of results, the cost and time constraints, and the experience of analyst in using the selected approaches to the selected data.

In general, researches at a global scale, coarse/low spatial resolution data such as wide swath ENVISAT ASAR (about 75 - 100 m) [Baldassarre *et al.* 2011] are helpful, at a regional scale, medium spatial resolution data such as ALOS-PALSAR, Sentinel-1 data (about 20 - 30 m) [Le *et al.* 2015a] are often used, whilst high resolution data like RADARSAT-2 (8 m) or very high resolution data such as TerraSAR-X, COSMO-SkyMed (1 - 2 m) [Marin *et al.* 2015] are suitable for tasks at local scale. For instance, in our works, we have collected four datasets over two test-sites as introduced in Section. 4.2. Therein, over Chamonix Mont-Blanc region, Sentinel-1 data with medium resolution of 5 m $\times$ 2 m (range $\times$ azimuth) can be used for the change analysis of this area (see Fig. 4.3b). Each image in this time series has the size of 1300 $\times$ 1200 pixels. High resolution data, RADARSAT-2 (9 m $\times$ 7.6 m in range $\times$ azimuth) with 7 images of size 700 $\times$ 1100 pixels, and very high resolution data, TerraSAR-X ($\sim$2 m) are, then, exploited to study two local characteristic areas: a parking area (Grands Montets - 600 $\times$ 600 pixels) and a moving glacier (the serac fall of Argentière - 500 $\times$ 500 pixels) which surface moves about 20 cm/day, i.e., more than one pixel between two consecutive dates in the TerraSAR-X time series. The two sub-test-sites include different kinds of change: parking occupation, glacier surface evolution, etc. (see Fig. 5.4 and 5.5). Over Merapi volcano, only ALOS-PALSAR data with medium resolution of 33.2 m $\times$ 28.4 m (range $\times$ azimuth) are available for the study of changes caused by the 2010 eruption (see Fig. 4.2), and the size of each image in this dataset is 1500 $\times$ 750 pixels. After the selection of study scales and data used for each task, we consider appropriate similarity measure and threshold to discriminate changed from unchanged pixels in the time series.

5.3.1.1 Similarity measure selection

For amplitude Sentinel-1 time series over a non-homogeneous area like Chamonix Mont-Blanc, the data present non-Rayleigh distribution and empirical distributions are more appropriate to describe the data. Based on the analysis of statistical model fit for SAR data in Section. 2.1.3, we have chosen the KLD of Log-normal distributions to measure the similarity between pixels of each pixel pile of this time

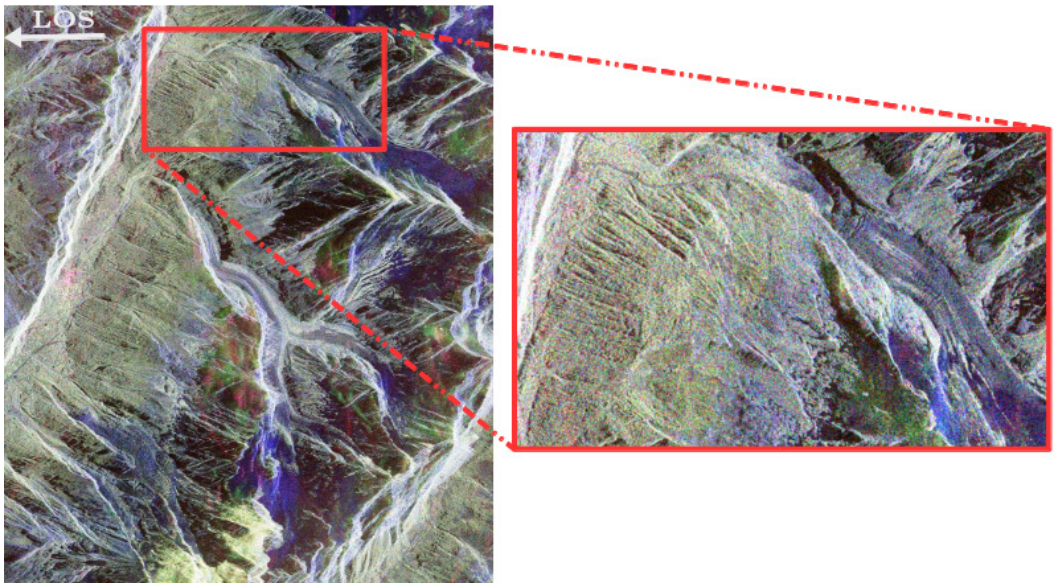

Figure 5.4: RADARSAT-2 sub-image (700 × 1100 pixels) of Argentière glacier and village acquired on June 22, 2009 (Pauli basis, R: HH - VV, G: 2HV, B: HH + VV).

series. It can be computed [Atto *et al.* 2013] as:

$$\begin{aligned}\mathfrak{D} &= KLD_{\text{Log-normal}}(X,Y) \\ &= \frac{1}{2}(\mu_X-\mu_Y)^2\left(\frac{1}{\sigma_X^2}+\frac{1}{\sigma_Y^2}\right)+\frac{1}{2}\left(\frac{\sigma_Y^2}{\sigma_X^2}+\frac{\sigma_X^2}{\sigma_Y^2}\right)-1.\end{aligned} \tag{5.6}$$

where μ_X, μ_Y, σ_X and σ_Y are the location and the scale parameters of two distributions of random variables X and Y, respectively. In order to detect changes at a feature level and to ensure the samples for the estimation of the Log-normal distribution, a large analysis window of 32×32 pixels are used.

With very high resolution TerraSAR-X data, changes can be analyzed at pixel level, in particular at moving area where glacier surface has a great difference between two consecutive acquisitions (in 11 days), or urban changes like the construction of buildings, appearance/disappearance of isolated targets, etc. For the purpose of detecting changes in each pixel pile by taking a test using as much as possible temporal samples and a few spatial samples if necessary, similarity measures that requires a small number of samples are preferable. We have chosen the minimum analysis window (including central pixel and its four nearest neighbors) when using spatial information. The CV can cope with reduced number of samples resulting from small temporal or spatio-temporal neighborhood and adaptive thresholds are thus selected. This is a homogeneity test using CV introduced in Section. 3.3.2.

For quad-pol RADARSAT-2 and dual-pol ALOS-PALSAR and dual-pol Sentinel-1 time series, considering the task requirement, the computational complexity, etc., Wishart distance given in Eq. (3.14) is selected to measure the similarity between

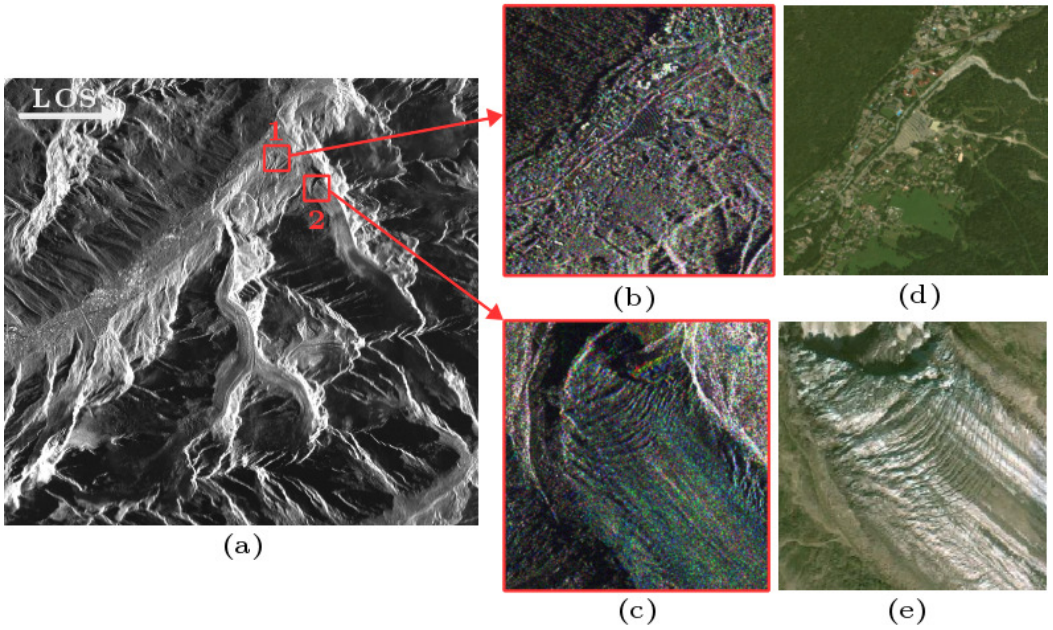

Figure 5.5: TerraSAR-X sub-images: 1 - Grands Montets parking (600 × 600 pixels); 2 - Serac fall of Argentière glacier (500 × 500 pixels); (a) Image acquired on October 10, 2009 over the entire Chamonix Mont-Blanc test-site; (b), (c) Color composition images (R: 2011/06/07; G: 2011/06/18; B: 2011/06/29), and (d), (e) Google Earth image of the two sub-areas.

pixels of each PolSAR pixel pile due to its mathematical efficiency under the assumption of Gaussian statistics. The analysis window size is 3×3 pixels when using spatial samples for this test.

With dual-pol Sentinel-1 time series, we have also performed the proposed approach in a frame of wavelet transform in order to detect changes at a pixel level and profit from parsimonious models related to the presence of non-stationarities in SAR images. Hence, texture changes in forested areas and accumulation zones of the glaciers caused by transitions between seasons (e.g., the surface is changed from uncovered into covered by snow) can be observed. Indeed, for dual-pol SAR data, polarimetric information is presented by a covariance matrix which is a complex, positive semi-definite, Hermitian, 2×2 matrix:

$$C = \langle k.k^{\dagger} \rangle = \begin{bmatrix} C_{11} & C_{12} \\ C_{21} & C_{22} \end{bmatrix}, \tag{5.7}$$

In this case, the SWT is used to decompose dual PolSAR images into low- and high- frequency subbands presented in different coefficients at different scales. The SWT coefficients of SAR subbands are considered as stochastic fields due to speckle occurring in this data. Each element C_{pq} of the covariance matrix of dual PolSAR data in (5.7) is decomposed by SWT as follows:

$$C_{pq}^{\mathcal{W}[J,\varepsilon]} = \mathcal{W}[J,\varepsilon]\{C_{pq}\}, \tag{5.8}$$

where the operator $\mathcal{W}[J,\varepsilon]$ computes the stationary wavelet decomposition at levels $J \in \{1,2,3\}$ into four coefficients $\varepsilon \in \{a,h,v,d\}$, with a is approximation subband (low-frequencies) and h (horizontal), v (vertical), d (diagonal) are detail subbands (high-frequencies). $C_{pq}^{\mathcal{W}[J,\varepsilon]}$ is a wavelet coefficient of C_{pq} (Fig. 5.6). In this work, we have used the Symlets 8 wavelet for SWT decomposition [Daubechies 1992].

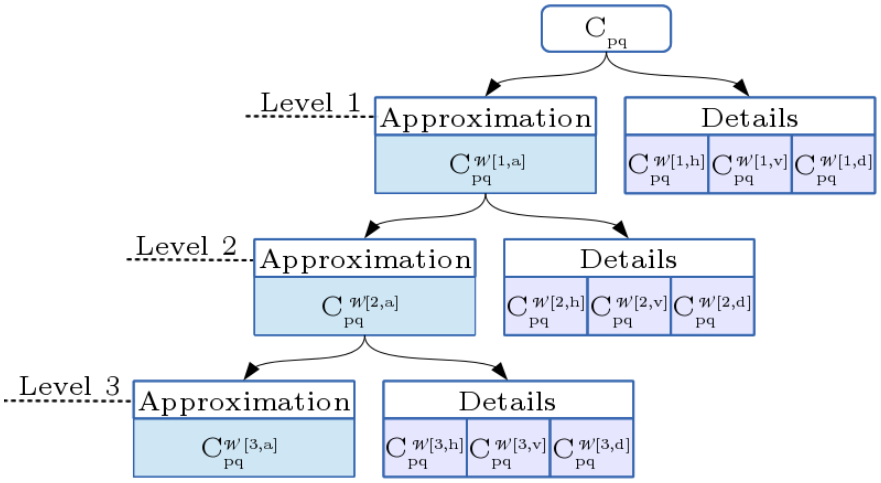

Figure 5.6: Wavelet decomposition tree with 3 levels of approximation and detail coefficients.

All individual elements $C_{pq}^{\mathcal{W}[J,\varepsilon]}$ are then synthesized to construct the SWT decomposed covariance matrix $C^{\mathcal{W}}$, i.e:

$$\mathcal{C}^{\mathcal{W}} = \left\{C^{\mathcal{W}[J,\varepsilon]}\right\} = \left\{\begin{bmatrix} C_{11}^{\mathcal{W}[J,\varepsilon]} & C_{12}^{\mathcal{W}[J,\varepsilon]} \\ C_{21}^{\mathcal{W}[J,\varepsilon]} & C_{22}^{\mathcal{W}[J,\varepsilon]} \end{bmatrix}\right\}; \begin{smallmatrix} J\in\{1,2,3\}; \\ \varepsilon\in\{a,h,v,d\} \end{smallmatrix}. \tag{5.9}$$

Then the Wishart distance is used to measure the similarity between two SWT decomposed SCMs $\langle \mathcal{C}^{\mathcal{W}} \rangle_t$ and $\langle \mathcal{C}^{\mathcal{W}} \rangle_\ell$ $(1 \leqslant t, \ell \leqslant N)$. For this experimental works, the Wishart distance is defined as the total sum of symmetric Wishart distances between two SWT subband SCMs $\langle C^{\mathcal{W}[J,\varepsilon]} \rangle_t$ and $\langle C^{\mathcal{W}[J,\varepsilon]} \rangle_\ell$ at the same level J and coefficient ε. From the SWT, PolSAR images are decomposed into multiresolution images at different scales, i.e. to obtain different instances of change information. Changes in approximations mainly consist in multidate pixel variations in low spatial frequencies (trends). Whereas changes in details are referred to variation in high spatial frequencies. Therefore, to measure the similarity between SWT decomposed SCMs, the Wishart distance $\mathfrak{D}$ are applied separately to approximation (5.10) and detail (5.11) subbands. In which, all approximation and detail subbands are considered to take advantage of redundancy:

$$\mathfrak{D}_A^{\mathcal{W}}\left(\langle\mathcal{C}^{\mathcal{W}}\rangle_t,\langle\mathcal{C}^{\mathcal{W}}\rangle_\ell\right)=\sum_{J\in\{1,2,3\}}\mathfrak{D}\left(\langle C^{\mathcal{W}[J,a]}\rangle_t,\langle C^{\mathcal{W}[J,a]}\rangle_\ell\right) \tag{5.10}$$

$$\mathfrak{D}_D^{\mathcal{W}}\left(\langle\mathcal{C}^{\mathcal{W}}\rangle_t,\langle\mathcal{C}^{\mathcal{W}}\rangle_\ell\right)=\sum_{\substack{J\in\{1,2,3\}\\ \varepsilon\in\{h,v,d\}}}\mathfrak{D}\left(\langle C^{\mathcal{W}[J,\varepsilon]}\rangle_t,\langle C^{\mathcal{W}[J,\varepsilon]}\rangle_\ell\right). \tag{5.11}$$

5.3.1.2 Threshold selection

The selection of a threshold value is a crucial step to discriminate "change" from "no-change". Over such heterogeneous areas like Chamonix Mont-Blanc and Merapi volcano, images are more or less affected by their high-relief terrain. In this thesis, we adopt the following approaches to determine threshold values:

- An adaptive threshold shown in Eq. (3.7) which can deal with the variation of number of samples in each test is applied to TerraSAR-X time series in CV tests.

- An automatic threshold selection approach, the minimum error thresholding algorithm (Kittler-Illingworth) (KI) [Kittler & Illingworth 1986], is applied to ALOS-PALSAR data over Merapi volcano to detect abrupt changes due to the eruption, and to Sentinel-1 data (with both amplitude and dual-pol time series).

- For the comparative purpose, we also conduct an empirical threshold selection with the RADARSAT-2 time series. This threshold is determined from training samples of test site specific content. This content relates to the different pixel classes which can be observed in the test site. Assuming that the study area has m classes, we choose the same number of training samples for each class. Then Wishart distances are calculated between pixels within each class (intraclass-distance) and between pixels of two different classes (interclass-distance) using an arbitrary image in the time series. We obtain m histograms of intraclass-distances and $m(m-1)/2$ histograms of interclass-distances. The empirical approach then consists in setting the threshold as the smallest Wishart distance value at the intersection point between histogram of intraclass-distances and histogram of interclass-distances (see Fig. 5.7).

  Fig. 5.7 shows the threshold selection of the quad-pol RADARSAT-2 dataset based on the Wishart distances between training samples of 4 classes which can be observed in the study region: homogeneous area (like grass), forested area, urban area and glacier area. Histograms in Fig. 5.7 illustrate the closeness of the classes, which implies the intricate threshold selection for this area. The threshold selection results of the KI approach and this empirical method are quite close (5.1 and 5.5, respectively).

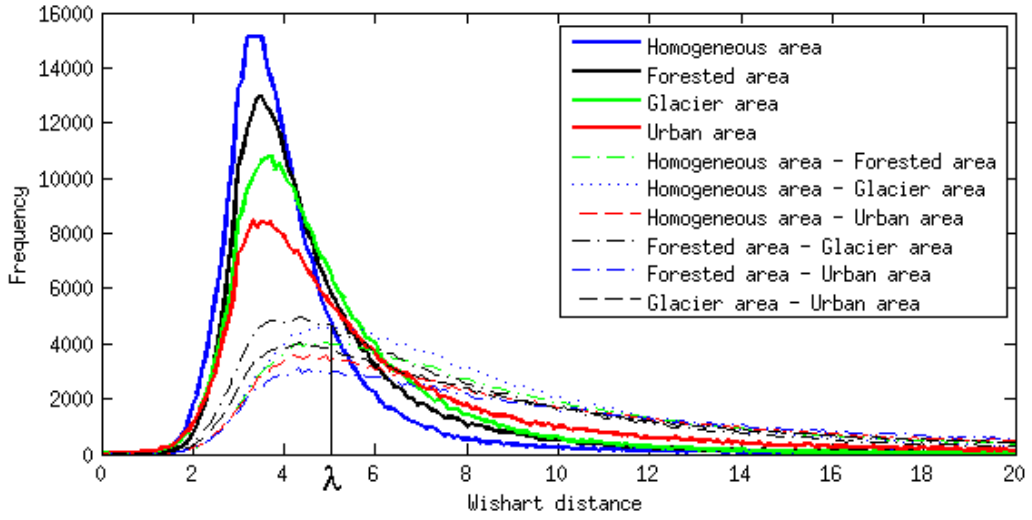

Figure 5.7: Histograms of Wishart distances of RADARSAT 2 data set of 4 classes observed in the study region: homogeneous area, forested area, urban area and glacier area. Solid lines: intraclass-distances; Dashed lines: interclass-distances.

5.3.2 CDM analysis

For every pixel pile, we obtain CDMs in which the CDM 1 is the preliminary detection of changes between each two dates in the time series. CDM 2 is the refined change detection results, derived by using all unchanged pixels identified in CDM 1 of each pile as multitemporal neighborhood to be retested.

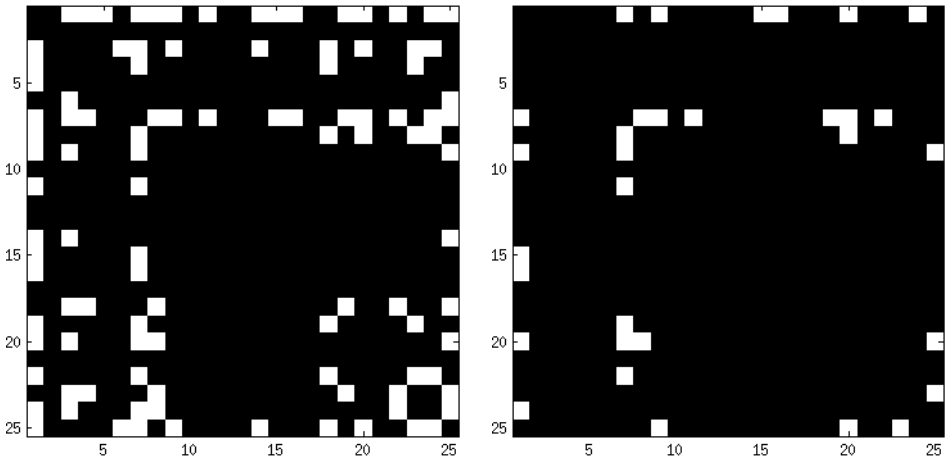

Figure 5.8: Example of CDMs at a homogeneous pixel pile in TerraSAR-X time series. (a) CDM 1; (b) CDM 2.

We can observe in Fig. 5.8 that the proposed method detects changed/unchanged

pixels in each pixel pile effectively and CDM 2 is a refined detection as reducing the "false alarms" involved in CDM 1.

To illustrate the proper determination of changed and unchanged pixel in CDMs, we compare the Log-normal distribution estimated from 32×32 spatial samples with Log-normal distributions estimated from three spatio-temporal neighborhoods selected from CDM:

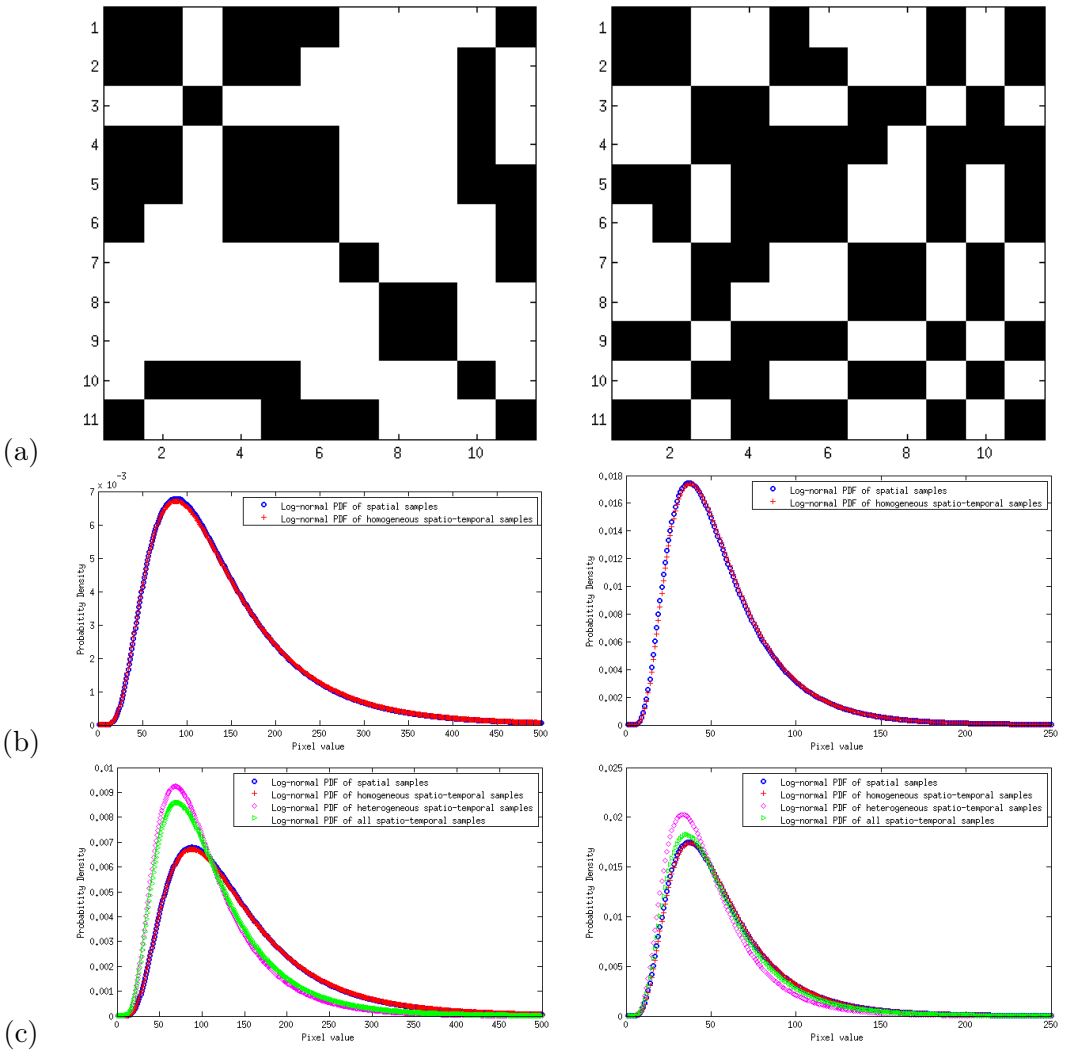

Figure 5.9: Examples of CDMs of a heterogeneous Sentinel-1 pixel piles and comparison of Log-normal distributions of different spatio-temporal neighborhoods determined from this CDM. Left - Example 1; Right - Example 2. (a) CDM, changed and unchanged pixels are represented in white and black respectively; (b) Log-normal distributions of spatio-temporal homogeneous samples versus Log-normal distribution of spatial samples; (c) Log-normal distributions of spatial samples, homogeneous spatio-temporal samples, heterogeneous spatio-temporal samples and all spatio-temporal samples.

- homogeneous samples (samples of only unchanged pixels in the pile),
- heterogeneous samples (samples of only changed pixels in the pile),
- and all spatio-temporal samples of the pile.

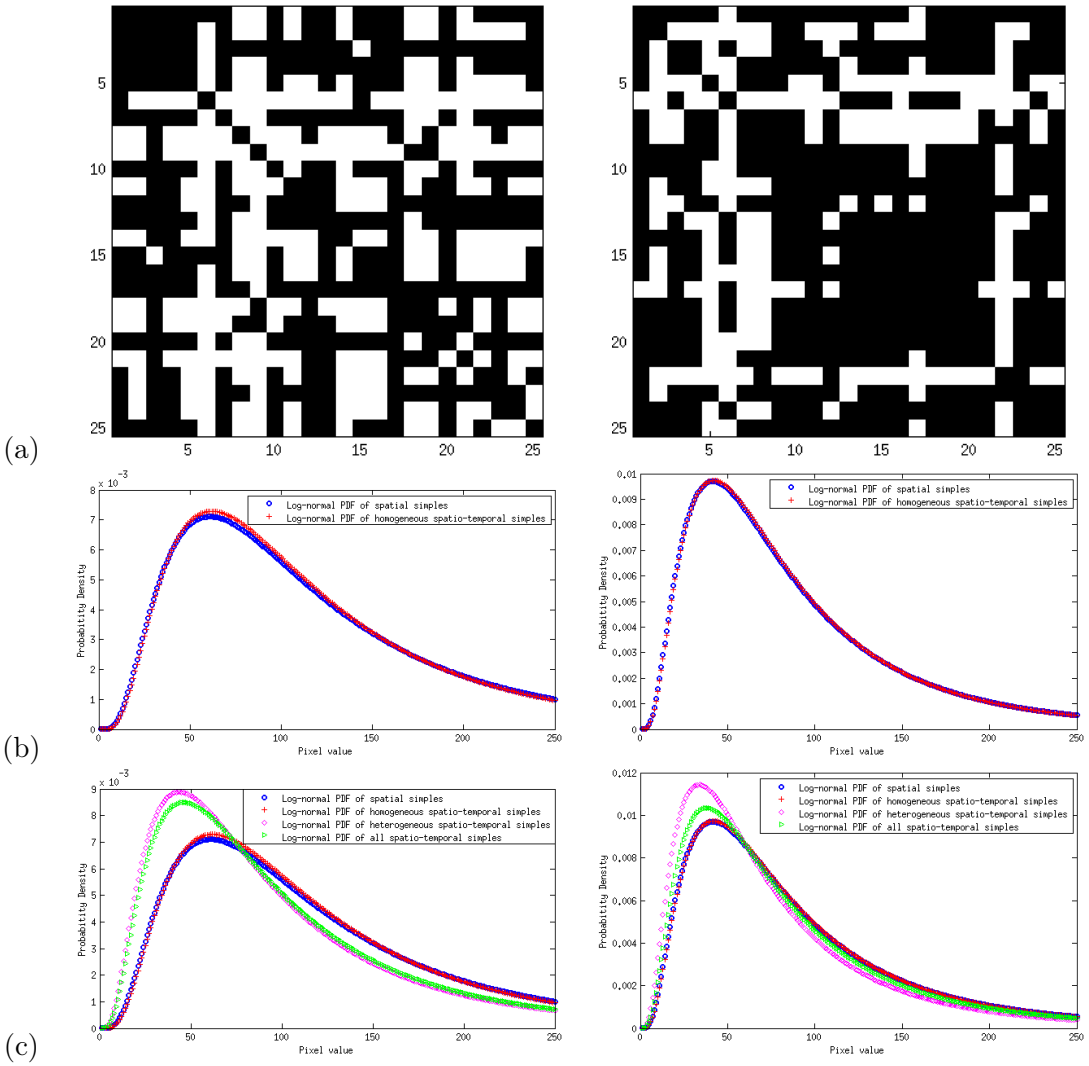

Figure 5.10: Examples of CDMs of a heterogeneous TerraSAR-X pixel piles and comparison of Log-normal distributions of different spatio-temporal neighborhoods determined from this CDM. Left - Example 1; Right - Example 2. (a) CDM, changed and unchanged pixels are represented in white and black respectively; (b) Log-normal distributions of spatio-temporal homogeneous samples versus Log-normal distribution of spatial samples; (c) Log-normal distributions of spatial samples, homogeneous spatio-temporal samples, heterogeneous spatio-temporal samples and all spatio-temporal samples.

Fig. 5.9 and 5.10 show some examples of the separation of changed and unchanged pixels in CDM when using Sentinel-1 and TerraSAR-X data with Log-normal distributions at heterogeneous pixel piles. They illustrate that the proposed approach has separated correctly changed and unchanged pixels in pixel piles. The distribution of homogeneous spatio-temporal samples is similar to the one of spatial samples (Fig. (b) of these figures). In Fig. (c) of these figures, the distributions of heterogeneous spatio-temporal samples are definitely different from the distributions of spatial samples. When we use all spatio-temporal samples of the pile, their distribution is the mixture between the distribution of homogeneous samples and distribution of heterogeneous samples.

The appearance of CDM reveals the possible changes in time of each pixel in a pixel pile. CDMs' appearance depends on: the similarity test to detect changes in the time series (similarity measure and thresholding method), the length of the time series (size of CDMs), the resolution, the frequency (band) and the polarization of SAR images compared to the observed phenomena, etc. In general, we can observe from appearances of CDMs some types of change under following hypotheses (see Fig. 5.11):

- H_0 - Temporal stability: no change occurs in the whole time series. This type of behavior may occur in a time series at a stable area or when its surface cover has no impact on the backscattering (covered by fresh dry snow for instance). The CDM of this behavior is expected to be totally black.

- H_1 - Dirac change: a change occurs in the time series on only one date. This kind of change presents the behavior on the radiometric temporal signal like dirac pulse. The CDM of this change is expected to include a change of white line and column at that date (except on the diagonal, of course). For instance, a flood presents on an image of the time series is a change of this type. The example in Fig. 5.12 (a) shows that a car appears in the Grands Montets parking at a certain location at the acquisition time of the 8^{th} date in the TerraSAR-X time series, but at other dates, there is no car at this position.

- H_2 - Step change: an abrupt change of an important magnitude occurs from date t_k and lasts until the end of the time series. The CDM is expected to appear two black block, one for the state on d dates before the change occurs and the other for the state after on $N - d$ dates. Therefore, when looking at CDM of this type of change, we can determine the time when the event occurs and its duration in the time series. This type of change expresses abrupt changes like natural disasters (earthquake, tsunami, etc.). Fig. 5.12 (b) shows the eruption of Merapi volcano in the last two date of the acquired time series. Gathering all pixels that have the CDMs of this type, we can obtain change map of this eruption.

- H_3 - Ramp change: a progressive change with increasing magnitude occurs from date t_k to date t_ℓ or from date t_k and maintained from that time. This

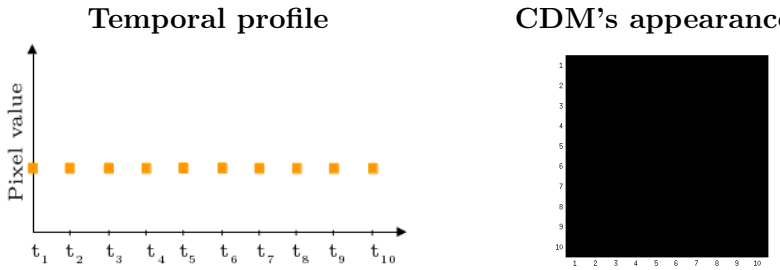

(a) H_0 - Temporal stability

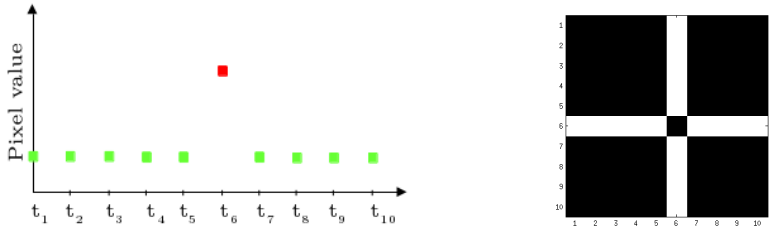

(b) H_1 - Dirac change

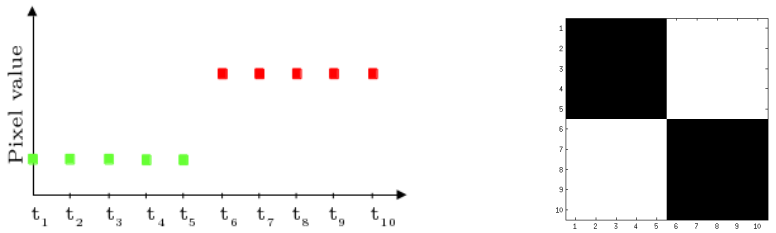

(c) H_2 - Step change

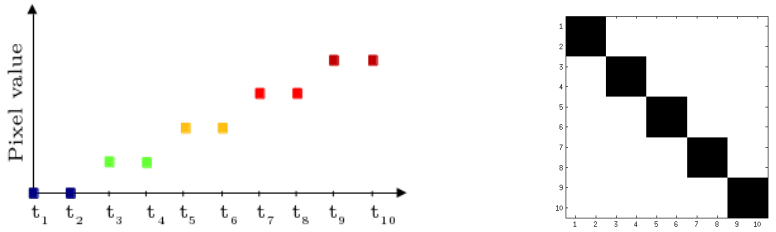

(d) H_3 - Ramp change

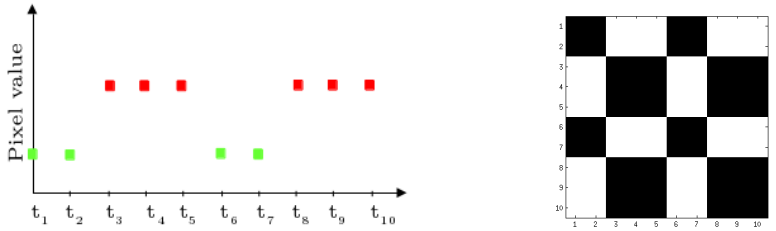

(e) H_4 - Periodic change

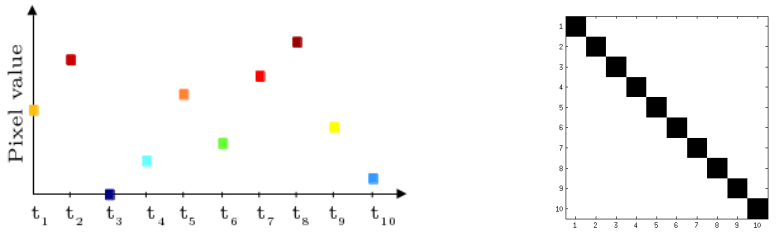

(f) H_5 - Chaotic change

Figure 5.11: Change hypotheses for change analysis of SAR image time series.

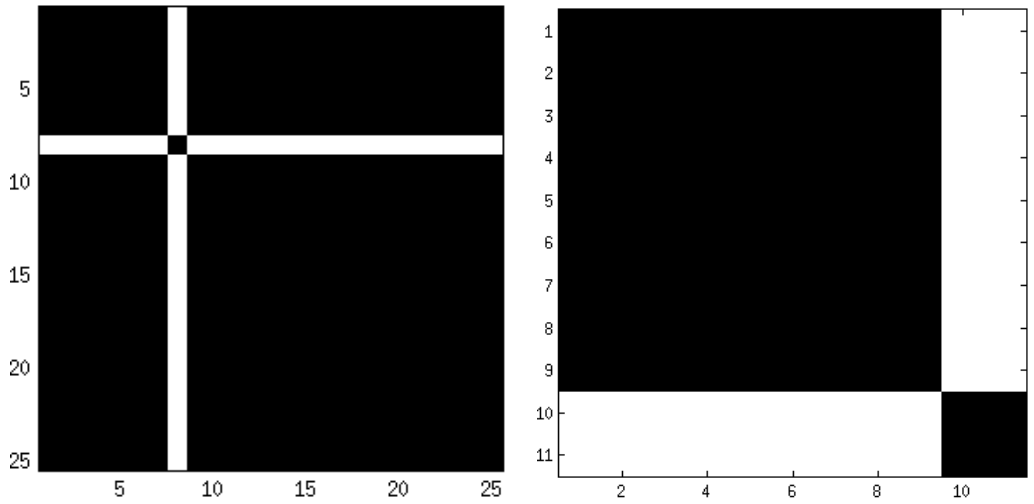

(a) (b)

Figure 5.12: CDMs when abrupt changes occurred. (a) A car appears in a parking in one date of the TerraSAR-X time series; (b) The eruption of Merapi volcano in two dates of the ALOS-PALSAR time series.

type of change often occurs at cultivated area or soil/coast erosion (by water and wind) and the change magnitude increases up to the vegetation growth or the erosion degree. The CDM appearance of this change should show regular black blocks corresponding to development periods of the studied object.

- H_4 - Periodic change: a progressive change of the same magnitude occurs in a period from date t_k to date t_ℓ (stationarity). It becomes cyclostationary change when occurring cyclically. This hypothesis is the case of seasonal change. Stationary periods of the time series can be observed on CDMs as black blocks. Fig. 5.13 shows two stable periods of a position at glacier area in the RADARSAT 2 series: one is the period from January 29, 2009 to February 22, 2009 (date 1 and 2) when snow still covered the surface. The other is from April 11, 2009 to Jun 22, 2009 (date 4 to 7) when snow disappeared. There is one image (date 3) that shows the transition between two stationary periods when snow was melting. From the detection of seasonal change, if the length of the time series is long enough, we can study the cycle of this kind of change in the observed area (cyclostationarity).

- H_5 - Chaotic change: changes occur with different magnitudes over the time. This kind of change often describes the fast surface evolution (at moving area for instance). CDMs at moving area look disorderly in our study case like glacier with moving tracks (Fig. 5.14 (a)). At this area, pixels almost change from date to date in the time series, there hence are few unchanged pixels detected (Fig. 5.14 (b)). At a same moving area, depending on the spatial

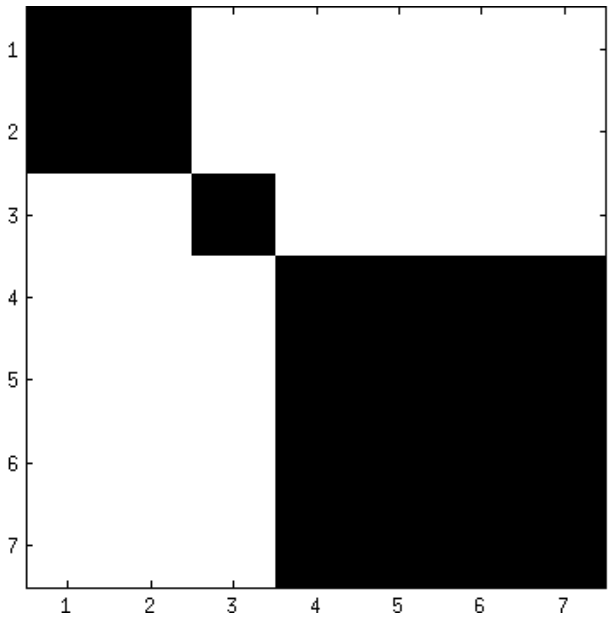

Figure 5.13: CDM including two stationary periods (date 1 to date 2: when snow covered the surface; date 4 to date 7: when the snow disappeared) at glacier area in RADARSAT 2 time series.

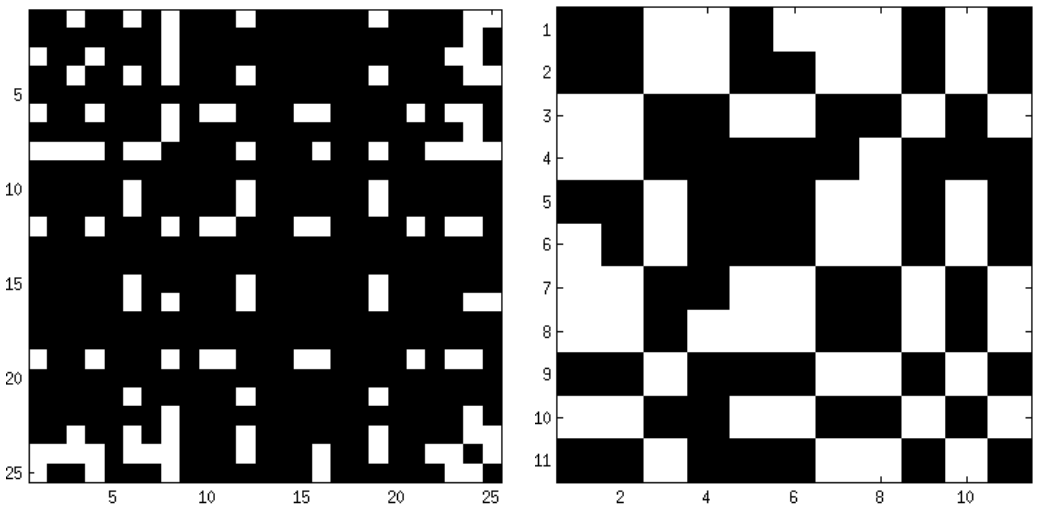

(a) (b)

Figure 5.14: CDMs at moving areas in TerraSAR-X time series (a) and in Sentinel-1 time series (b).

and temporal resolution of data, the appearances of CDMs are different due to the motion and to the glacier fast surface changes.

These characterizations are provided for the illustrative purpose, other scenarios can be considered ulteriorly according to the applications.

5.4 Conclusions

In this chapter, a framework for the analysis of SAR images time series has been proposed. This approach is based on the construction of CDM which identifies changed and unchanged pixels in the time series through similarity cross tests. The key point to perform the approach is the selection of appropriate similarity measure and threshold value to separate changes from no-changes. This selection depends on the user's need, the scale of study and the data used. This is also a trade-off between the task requirement and the cost/time constrains.

The proposed approach can be used with various similarity measures, i.e., the CV to test the homogeneity of sets of samples, the Wishart distance to measure the similarity between covariance matrices of PolSAR data with a small analysis window size to analyze changes at pixel level, and also the KL distance with a large analysis window size in order to detect changes at a feature level.

Table 5.1 shows the recapitulation of datasets, similarity tests and analysis window sizes used in this thesis to implement the proposed method.

Table 5.1: Summary of datasets and similarity tests used.

Dataset	Similarity measure	Thresholding method	Window size (pixels)
HH TerraSAR-X	CV	Adaptive	1 central + 4 nearest
Quad-pol RADARSAT-2	WD	Empirical	3×3
Dual-pol ALOS-PALSAR	WD	KI	3×3
Dual-pol Sentinel-1	WD	KI	3×3
VV Sentinel-1	KLD	KI	32×32

The analysis from diverse SAR data over two different study areas with many kinds of change, the properties of CDM show that the proposed framework provides a relevant tool for simplifying the analysis and the extraction of changed/unchanged information in SAR image time series.

In general, for the single polarization data with low/medium resolution, we recommend an analysis at patch scale using similarity measures between patches (e.g. KL distance) and an automatic threshold approach. In the case of high resolution, an analysis at pixel scale is more appropriate in order to preserve detail information provided by this kind of data, and then a similarity measure between small neighborhoods (e.g. the CV) and an adaptive automatic threshold approach are preferable. For the multipolarization data, we recommend the use of suitable similarity measures between covariance/coherency matrices such as the Wishart distance, the

Fixed Point distance, etc. and an automatic threshold or a supervised threshold approaches (if training zones/samples are available).

For the construction of CDM 2, in the case where long time series are acquired and heterogeneous zones are considered, it becomes possible to use purely temporal neighborhoods. Conversely, in the case of small time series over homogeneous zones, spatio-temporal neighborhoods are preferable. For the discrimination of different types of change in low and high spatial frequencies, the multiscale analysis of wavelet transformation can be applied to CDM approach.

With the proposed two step strategy of the method, different types of change occurring in the time series can be detected: seasonal changes, abrupt changes, surface evolution, etc. The appearance of CDMs makes these changes visible and analyzable. The important advantages of the proposed framework are that it can be applied to various SAR data and the temporal neighborhoods provided by the CDM can be used to investigate change dynamics of observed areas, to detect many kinds of change in the time series and to perform spatio-temporal filtering. These applications of CDM will be described in next chapters.

Chapter 6

Change analysis

Contents

With the proposed approach, we obtain CDMs which show the variation in time of features at each pixel location. According to these CDMs, we have "pictures" about the development periods of objects (for instance, slow changes like the erosion, vegetation evolution, etc., or abrupt changes like natural disasters: tsunami, earthquake, etc.). The information of CDM, thus, opens abilities to apply to many fields such as multitemporal filtering, multitemporal change detection, classification, etc. In this chapter, spatio-temporal information extracted from SAR image time series in CDMs is first exploited to perform change analysis. From changes detected in CDM of each pixel pile after similarity tests in Section 5.2, we obtain pair-wise binary change maps of the time series. Depending on the research purpose, the change characteristics of the study area over the time series, these pair-wise change maps, are then combined to enhance change detection results. After that, we propose an index of change dynamics based on change information in CDMs, which enable to obtain a change dynamics' map in order to have a general view of changes occurring over time series.

6.1 Binary change map

6.1.1 Pair-wise change maps

From CDM2s obtained in Eq. (5.5), we can obtain multitemporal change maps between each two dates of the time series as follows:

$$\mathcal{CM}_{t,\ell} = \{\hat{M}^{w}_{t,\ell}(i,j)\}_{\substack{1\leqslant i\leqslant N_c \\ 1\leqslant j\leqslant N_l}} \tag{6.1}$$

where, $\mathcal{CM}_{t,\ell}$ is the change map between date t and ℓ and $N_c \times N_l$ is the size of each image in the time series. We then have $N(N-1)/2$ change maps as illustrated in Fig. 6.1.

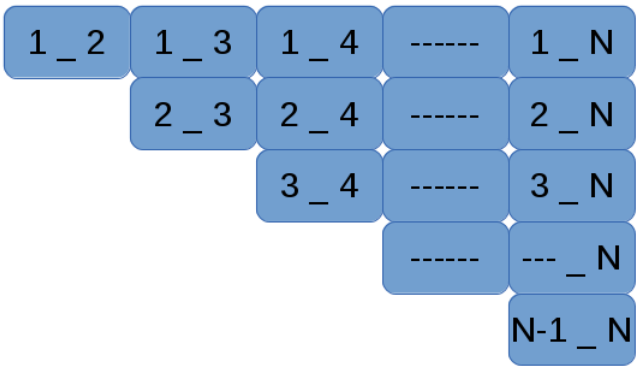

Figure 6.1: Pair-wise change maps

6.1.2 Detection of d-length change

With pair-wise change maps given in Fig. 6.1, there are various ways to employ them in order to have a better result of change detection. For example, the diagonal offers change maps between each two consecutive dates (t and $t+1$). Columns or rows give change maps between a reference date t and all other dates ℓ ($1 \leqslant \ell \leqslant N; \ell \neq t$) in the time series, etc.

By taking pair-wise change maps in a column/row into a test to output only one change map for each date in the time series, we intend to detect changes which affect at least "d" different images. The example in Fig. 6.2 (a) shows that, the change appears in the last two dates of the time series, and in Fig. 6.2 (b), the change appears at the sixteenth date and lasts in four dates. We propose to define "d-length" change map corresponding to the reference date t as:

$$\mathcal{CM}_t^{(d)}(i,j) = \begin{cases} 0 & \text{if } \sum_{\substack{\ell=1 \\ \ell \neq t}}^{N} \mathcal{CM}_{t,\ell}(i,j) < N-1-d \\ 1 & \text{if } \sum_{\substack{\ell=1 \\ \ell \neq t}}^{N} \mathcal{CM}_{t,\ell}(i,j) \geqslant N-1-d \end{cases} \tag{6.2}$$

Indeed, if there is an abrupt change occurring in the observed region which lasts "d-dates", images acquired at these d dates (where the change still appears) will be different from all other dates. At the changed zone, one can refer to two cases:

1) The reference image t is acquired in the period d: when comparing this image to all other images in the period d, we have $d-1$ responses which are "0 -

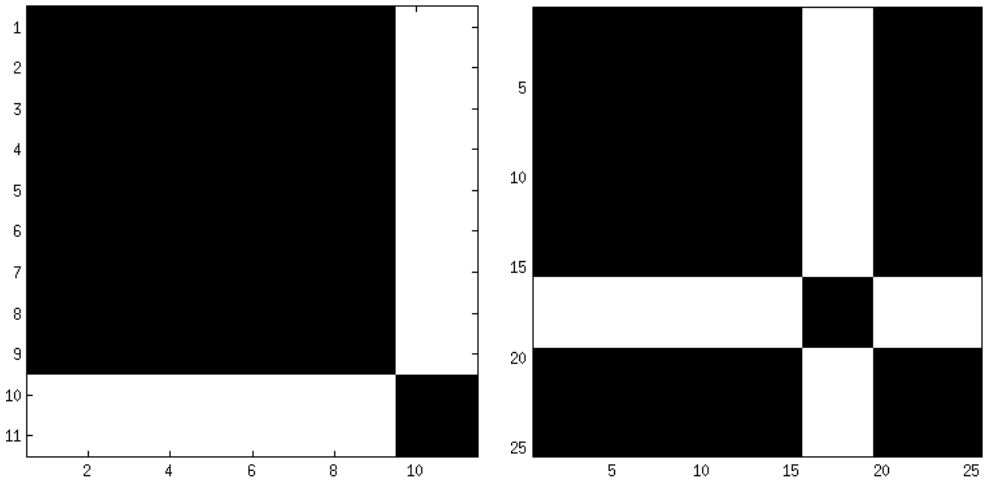

(a) (b)

Figure 6.2: CDMs at d-length change regions. (a) The change appears and lasts in the last two dates of the time series including 11 images. (b) The change appears and lasts from the sixteenth date to the nineteenth date in the time series including 25 images.

unchanged", and $N - d$ responses being "1 - changed" when comparing to all images which are out of the period d.

2) Otherwise, the results are: d "changed" and $N - 1 - d$ "unchanged" responses.

Therefore, to assign a pixel of image t into d-length change class, it should have at least $N - 1 - d$ responses indicating that it is different to other pixels in the pixel pile.

6.1.3 d-length change detection result

The experimental work of this change detection is conducted using the ALOS-PALSAR data set. Fig 6.3 shows the change maps between date 11 and other dates in the time series. By taking all these change information into the test in (6.2), we obtain only one change map containing change information related to the eruption in date 11 with $d = 2$.

Table 6.1: Error evaluation of pair-wise change detection results over Merapi volcano using ALOS-PALSAR image time series.

Errors \ $\mathcal{CM}_{t-\ell}$	11_1	11_2	11_3	11_4	11_5	11_6	11_7	11_8	11_9
Overall errors(%)	19.8	22.5	20.4	21.9	17.3	21.2	20.7	19.4	20.1

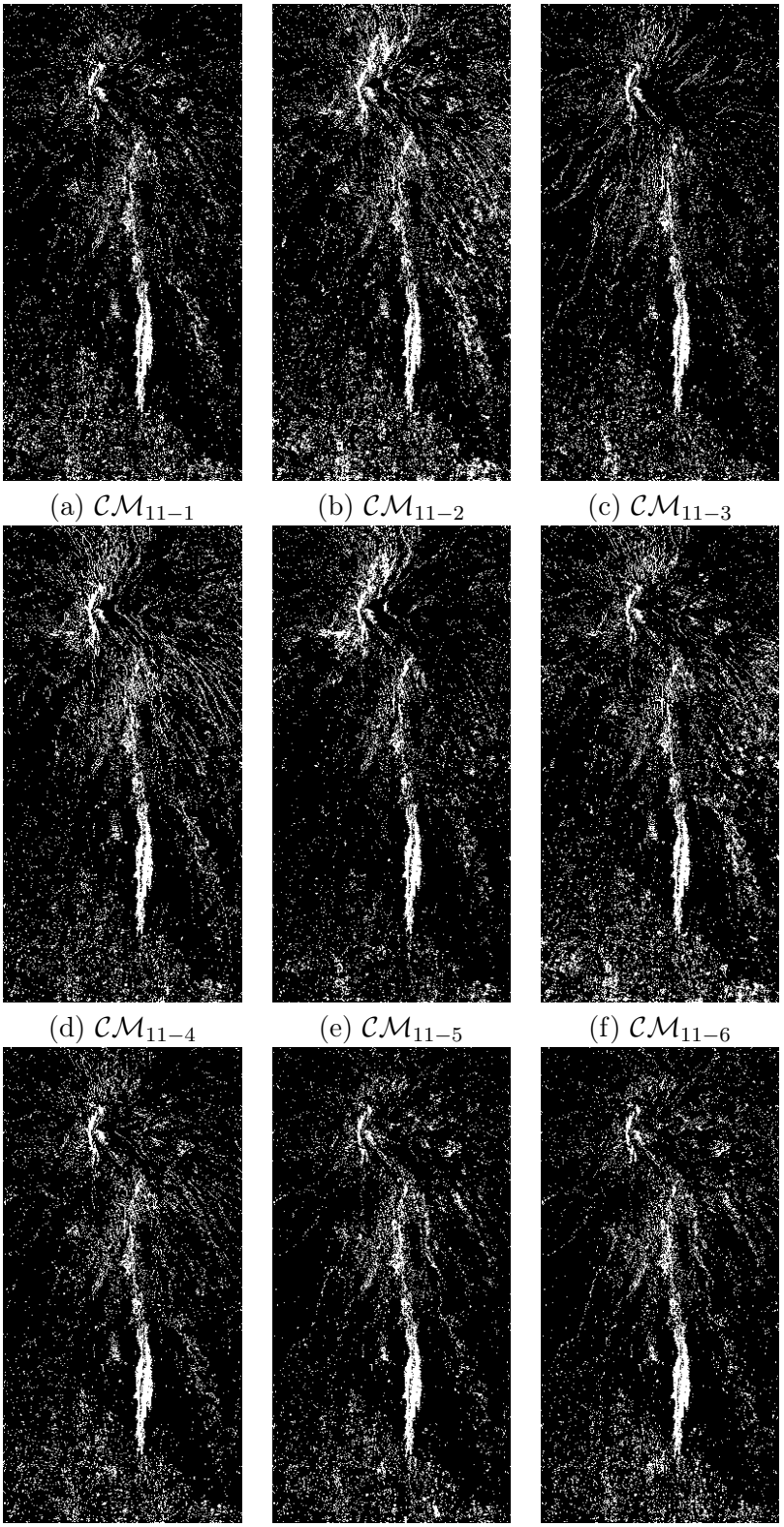

(a) $\mathcal{CM}_{11-1}$ (b) $\mathcal{CM}_{11-2}$ (c) $\mathcal{CM}_{11-3}$

(d) $\mathcal{CM}_{11-4}$ (e) $\mathcal{CM}_{11-5}$ (f) $\mathcal{CM}_{11-6}$

(g) $\mathcal{CM}_{11-7}$ (h) $\mathcal{CM}_{11-8}$ (i) $\mathcal{CM}_{11-9}$

Figure 6.3: Change maps between date 11 and other $N - d$ dates in the ALOS-PALSAR time series over Merapi volcano.

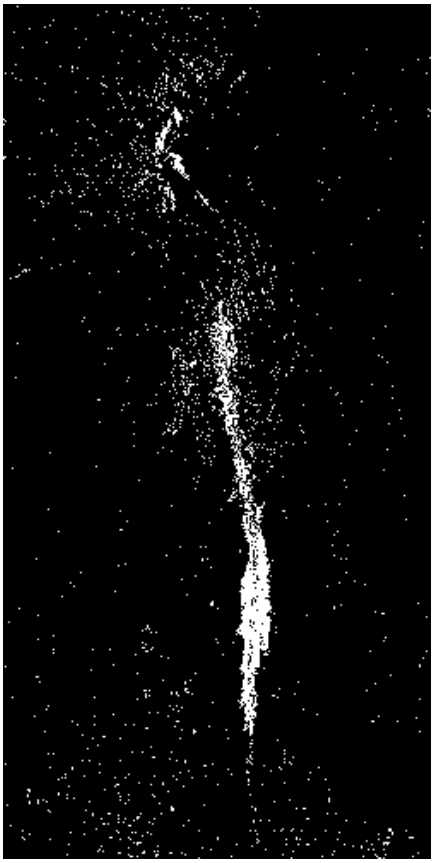

Figure 6.4: Change map $\mathcal{CM}_{11}^{(2)}$ presents the eruptive deposits with t = 11, d = 2 of Merapi volcano eruption in 2010 using ALOS-PALSAR image time series.

Fig. 6.4 shows the 2-length change map $\mathcal{CM}_{11}$ corresponding to the eleventh image of the time series in comparison to other images. In our case, the date of the event is known, we can derive directly the change map corresponding to this date. If we do not know the date of the event in the time series, the analysis of CDMs will reveal the date and the length of change (e.g. Fig. 5.12 (b)).

The quantitative assessment of change detection result obtained by the proposed method is presented in Table 6.2 and Table 6.3 by using ground truth samples. They have been manually extracted based on visual interpretation of optical views and by referring to field-based data by [Charbonnier *et al.* 2013], [Komorowski *et al.* 2013] and [Solikhin *et al.* 2014]. Comparing to 5638 ground truth samples of both changed and unchanged classes, the proposed method detected 2319 correct and 102 false changed pixels, while it missed 457 changed pixels which are assigned as unchanged pixels. The obtained change detection result has high accuracy (90.09%) with limited errors: 4.21% false alarms, 16.46% missed alarms and 9.91% overall errors. The combination of all information acquired in the time series (both change and redundancy information) increases the accuracy of change detection (in comparison with

Table 6.2: Confusion matrix of d-length change detection result over Merapi volcano using ALOS-PALSAR image time series.

Class		Ground truth		Total
		Changed	Unchanged	
Change map	Changed	2319	102	2421
	Unchanged	457	2760	3217
Total		2776	2862	5638

Table 6.3: Error evaluation of d-length change detection result over Merapi volcano using ALOS-PALSAR image time series.

	False alarms	Missed alarms	Overall errors
(Pixels)	102/2421	457/2776	559/5638
(%)	4.21	16.46	9.91

the accuracy of pair-wise change detection results between date 11 and other dates in Table 6.1).

6.2 Analysis of change dymamics in SAR image time series

6.2.1 Index of change dynamics

The change information provided by CDMs allows the investigation of the dynamics of changes occurring at the observed area in order to understand the evolution trends of the area. Features showing temporal variation compared to their surroundings make the pixels have different levels of change dynamics, ranging from stable pixels (almost unchanged) to unstable pixels (always changed). In this section, we introduce an index relating the change dynamics at each pixel position.

A change detection decision can be seen as a random variable (binomial trial) with two possible outcomes: 1 for changed pixels and 0 for unchanged ones. Let $\rho(i, j)$ be the probability of the "changed" outcome at position (i, j), the probability of the "unchanged" outcome is thus equal to $1-\rho(i, j)$. Given an N-length time series and $N(N-1)/2$ change detection experiments, the probability of having exactly q

changed results is then:

$$P(q) = \binom{N(N-1)/2}{q} \rho(i,j)^q (1-\rho(i,j))^{N(N-1)/2-q} \tag{6.3}$$

where the notation $\binom{\cdots}{\cdots}$ denotes the standard binomial coefficients.

Given a pixel pile $\{\mathcal{I}_t(i,j)\}_{1\leqslant t\leqslant N}$, we propose to define an index of change dynamics as the probability $\rho(i,j)$ of "changed" responses of similarity tests given in Section 5.2 estimated hereafter by the proportion of "1" in the CDM $\hat{M}^w_{t,\ell}(i,j)$ at that position:

$$\rho(i,j) = \frac{2}{N(N-1)} \sum_{t=1}^{N} \sum_{\ell=t+1}^{N} \hat{M}^w_{t,\ell}(i,j) \tag{6.4}$$

The index ρ has values from 0 - purely stable (no temporal change occurs in the time series) to 1 - unstable (pixels change for any arbitrary pair of dates).

6.2.2 Map of change dynamics in SAR image time series

A CDM being a boolean change information matrix, the index $\rho(i,j)$ provides the expectation of change in the different pairs $(\mathcal{I}_t(i,j), \mathcal{I}_\ell(i,j))$ found in the pixel pile from spatio-temporal similarity measurements given in Section 5.2. The map of dynamic indexes obtained in Eq. (6.4) has some impulse noise reflecting non-significant changes when we construct CDM in pixel scale. A regularization step is thus necessary to derive a map of change dynamics. The strategy proposed below is based on change occurrence level and exploits a combination of Median and Mode values, both statistics are considered in a recursive implementation:

$$\rho_1(i,j) = \text{Median}\begin{bmatrix} \rho_1(i-u,j-v)\cdots\rho_1(i-u,j-1)\rho_1(i-u,j)\rho_1(i-u,j+1)\cdots\rho_1(i-u,j+v) \\ \vdots \quad \vdots \quad \vdots \quad \vdots \quad \vdots \\ \rho_1(i-1,j-v)\cdots\rho_1(i-1,j-1)\rho_1(i-1,j)\rho_1(i-1,j+1)\cdots\rho_1(i-1,j+v) \\ \rho_1(i,j-v) \quad \cdots\rho_1(i,j-1) \quad \rho(i,j) \quad \rho(i,j+1) \quad \cdots\rho(i,j+v) \\ \rho(i+1,j-v) \quad \cdots\rho(i+1,j-1) \quad \rho(i+1,j) \quad \rho(i+1,j+1) \quad \cdots\rho(i+1,j+v) \\ \vdots \quad \vdots \quad \vdots \quad \vdots \quad \vdots \\ \rho(i+u,j-v) \quad \cdots\rho(i+u,j-1) \quad \rho(i+u,j) \quad \rho(i+u,j+1) \quad \cdots\rho(i+u,j+v) \end{bmatrix}^{\ddagger} \tag{6.5}$$

$$\rho_2(i,j) = \text{Mode}\begin{bmatrix} \rho_2(i-u,j-v)\cdots\rho_2(i-u,j-1)\rho_2(i-u,j)\rho_2(i-u,j+1)\cdots\rho_2(i-u,j+v) \\ \vdots \quad \vdots \quad \vdots \quad \vdots \quad \vdots \\ \rho_2(i-1,j-v)\cdots\rho_2(i-1,j-1)\rho_2(i-1,j)\rho_2(i-1,j+1)\cdots\rho_2(i-1,j+v) \\ \rho_2(i,j-v) \quad \cdots\rho_2(i,j-1) \quad \rho_1(i,j) \quad \rho_1(i,j+1) \quad \cdots\rho_1(i,j+v) \\ \rho_1(i+1,j-v)\cdots\rho_1(i+1,j-1)\rho_1(i+1,j)\rho_1(i+1,j+1)\cdots\rho_1(i+1,j+v) \\ \vdots \quad \vdots \quad \vdots \quad \vdots \quad \vdots \\ \rho_1(i+u,j-v)\cdots\rho_1(i+u,j-1)\rho_1(i+u,j)\rho_1(i+u,j+1)\cdots\rho_1(i+u,j+v) \end{bmatrix}^{\ddagger} \tag{6.6}$$

where ρ_1, ρ_2 are the index of change dynamics after the Median and the Mode filtering and ‡ stands for vectorization of a matrix (whatever the order since Median and Mode are invariant with respect to set ordering). The analysis window size of these two filters is $(2u+1)\times(2v+1)$.

These two recursive filters are used with a line by line scan of the image. This scan has shown relevancy for regularization of map of change dynamics over glaciers and volcanoes impacted by impulse noise. It is worth noticing that other scans, such as Hilbert Peano scan, can be applied, depending on the data statistics or geometry contents.

In this strategy, the Median operator is highly robust to outlier values (map of change dynamics suffers from non-significant changes, see Fig. 6.6 (b) for illustration) and the Mode operator (most frequently occurring value) performed on median values makes sharp regularization possible (see for instance Fig. 6.6 (c)).

6.2.3 Result of change dynamics' analysis

For each pixel pile of the time series, we have an index of change that show the degree of change at this pixel location. The map of change dynamics for the whole time series thus provides a general view of the variation in time of the observed area. In this section, the change dynamics over the two test-sites are analyzed respectively as follows: results of single polarization datasets (Sentinel-1 (VV) and TerraSAR-X (HH)) using KLD and CV tests; and of multipolarization datasets (dualpol Sentinel-1 and dualpol ALOS-PALSAR) using Wishart distance tests with original time series and wavelet decomposed time series.

6.2.3.1 With single polarization datasets over Chamonix Mont-Blanc test-site

VV Sentinel-1 image time series

The map of change dynamics obtained from the single polarization Sentinel-1 dataset over the whole Chamonix Mont-Blanc test-site is given in Fig. 6.5. This figure presents the result obtained with the VV amplitude Sentinel-1 time series and KL distance between two Log-normal distributions for the similarity criterion. The thresholding method used for separating changed and unchanged pixel is KI method (cf. Section 5.3.1).

The map of change dynamics in Fig. 6.5 shows that dynamic zones in the test-site are the moving areas, i.e., the three glaciers: Argentière, Mer-de-Glace and Bosson, in particular at the serac fall and crevasse zones where slope ruptures create fast changing features in SAR images. It can be observed that the change dynamics varies on the glaciers, depending on the morphology of surface cover:

- in the presence of crevasses and seracs, it reaches the maximum values ($\rho \simeq 0.8$) where the glacier flows are the most rapid (1 m/day at the Géant serac of Mer-de-Glace and about 50 cm/day at serac fall of Argentière glacier);

- in the presence of debris rocks on the surface, it still often shows a medium value ($\rho \simeq 0.5$) due to the change of the distributed targets and penetration properties (e.g. dry/wet snow);

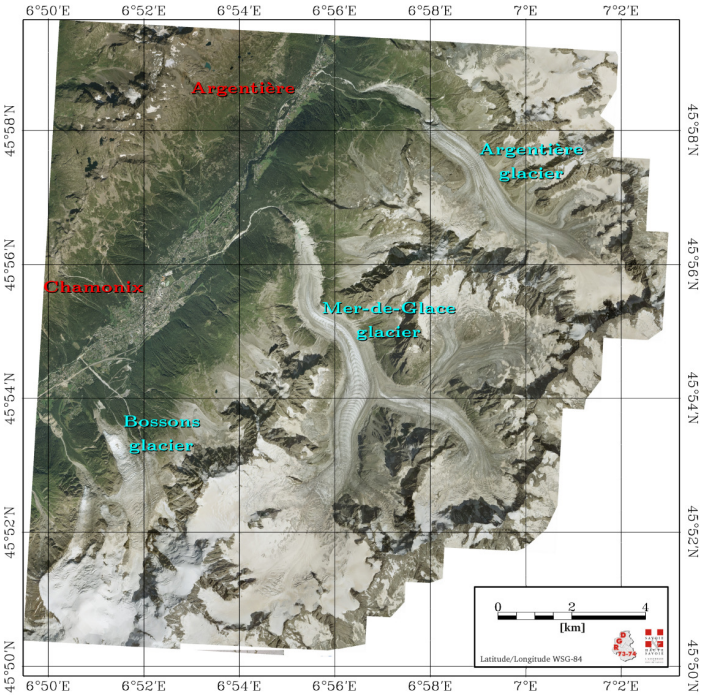

(a)

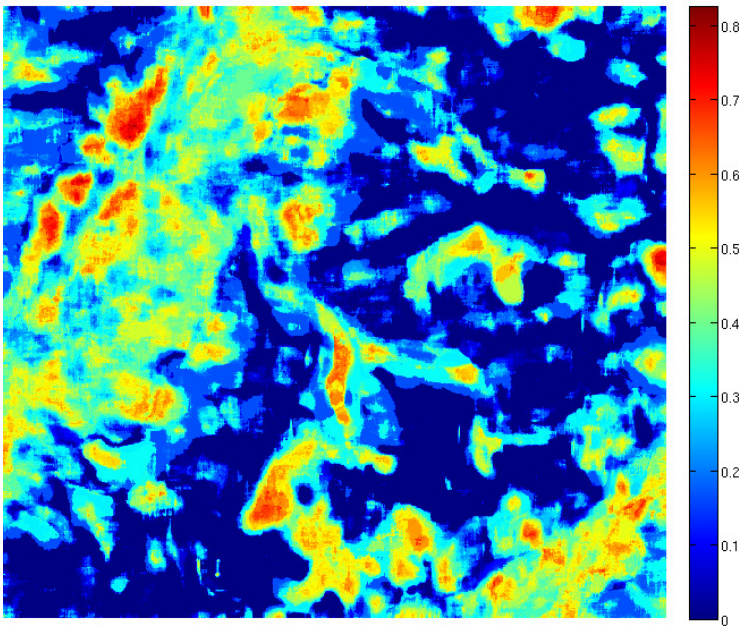

(b)

Figure 6.5: Map of change dynamics at Chamonix Mont-Blanc obtained with VV amplitude Sentinel-1 image time series using KLD tests. (a) Chamonix Mont-Blanc main glaciers and villages (2008 airborne photography, © RGD 73-74); (b) Map of change dynamics.

- in the present of firn on the highest part of glaciers (in accumulation areas), it is usually lower ($\rho < 0.5$) since these areas are more stable.

In the two first cases above, the glacier surface produces the texture in SAR images. On the contrary, in the last case, the glacier surface is composed of only bare ice or firn without crevasses, debris rocks, etc., resulting in less texture in SAR images.

Indexes of change dynamics in forested areas are about 0.5 to 0.6 by the cause that the image acquisition dates are from November 15, 2014 to March 15, 2015. This acquisition period involves a transition between the autumn and the winter, the surface is thus changed from uncovered into covered by snow. At the villages in Chamonix valley, where many activities occurred in December and January (during the touristic season), indexes of change dynamics are about 0.6. Besides that, some layover effect areas with quite high indexes of change dynamics can also be observed due to radiometric changes.

In the KLD approach, we have used a large analysis window of 32×32 pixels, when using spatial information, to ensure the number of samples for the estimation of Log-normal PDF parameters, which allows the detection of change in feature/texture level. With large analysis window, the regularization strategy proposed in Section 6.2.2 is not applied but the map of change dynamics is still smooth.

HH TerraSAR-X image time series

With the analysis over the whole test-site of Chamonix Mont-Blanc using medium spatial resolution Sentinel-1 data, we have a general look of change dynamics at this study area. With very high resolution TerraSAR-X dataset, we have chosen the serac fall of Argentière glacier for the analysis of change dynamics at pixel level. At this area, glacier pixel values in the time series change from date to date, in particular each point on this surface moves more than one pixel between different acquisitions. The spatial analysis window size at pixel level includes the considered pixel and its four nearest neighbors, and the similarity test for this dataset is the CV test (cf. 3.3.2.1).

The map of change dynamics of the serac fall of Argentière in Fig. 6.6 properly reflects the actual situation when comparing it to the amplitude arithmetic mean image of the whole time series (Fig. 6.6 (a)) which can be seen as a kind of ground truth in this case. Fig. 6.6 (b) shows the map of change dynamics with non-significant noise due to the change analysis in pixel scale. The proposed regularization strategy is then applied in order to obtain smoother map of change dynamics. It can be observed in Fig. 6.6 (c) that at glacier area, indexes of change dynamics are high ($\rho \approx 0.7$), in particular, at the seracs fall and the fast moving crevasses ($\rho \approx 0.9$). On the contrary, at stable area (like rock) where almost no change occurs, indexes of change dynamics are very low ($\rho \approx 0.1$).

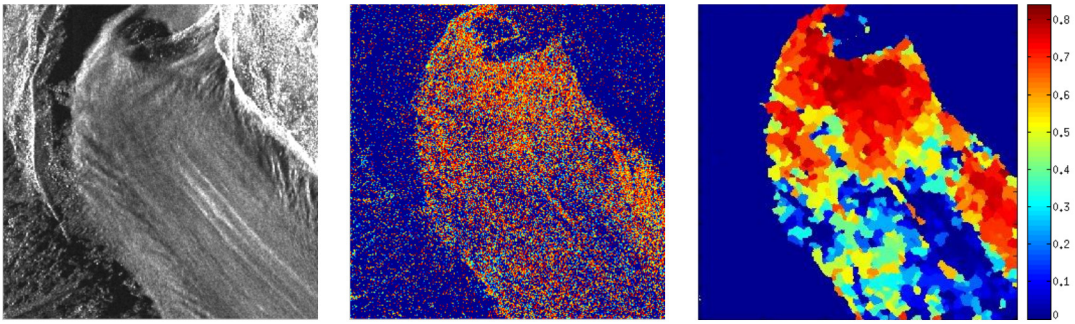

(a) (b) (c)

Figure 6.6: Map of change dynamics of HH amplitude TerraSAR-X image time series. (a) Amplitude image obtained by arithmetic mean of the whole time series; (b) Map of change dynamics with non-significant noise due to the change analysis in pixel scale; (c) Map of change dynamics after the proposed regularization strategy.

6.2.3.2 With dual-polarization datasets

Dual-pol Sentinel-1 image time series over Chamonix Mont-Blanc test-site

Original time series:

Fig. 6.7 shows the change detection result when using a time series of dual-pol Sentinel-1 images with Wishart distance for the similarity test, and in Fig. 6.8, we have applied the same scenario but in a wavelet transform framework. The thresholding method used for the similarity test is KI method (section 5.3.1).

The map of change dynamics in Fig. 6.7 (a) is quite similar to the one in Fig. 6.5. However, the Wishart distance approach for dual-pol Sentinel-1 time series analyzes changes at pixel level with an analysis window of 3×3 pixels when using spatial information, whilst the KLD approach for VV Sentinel-1 time series uses an spatial analysis window of 32×32 pixels to derive the map of change dynamics (in Fig. 6.5) at feature/texture level. Indexes of change dynamics in Fig. 6.7 at pixel level are slightly lower at moving areas like on Mer-de-Glace and Argentière glaciers than those in Fig. 6.5. The reason is that texture of crevasse or debris covers which are changed in different images of the time series when observing in large window, however, it can be the same from one track to another track at pixel level (with the resolution of Sentinel-1 image).

The map of change dynamics in Fig. 6.5 looks more regularized than the one in Fig. 6.7 (a). The regularization strategy (cf. Section 6.2.2) is thus applied only for maps of change dynamics obtained at pixel level in order to have smoother maps (Fig. 6.7 (b)). This regularization improves the noisy results obtained from the original time series.

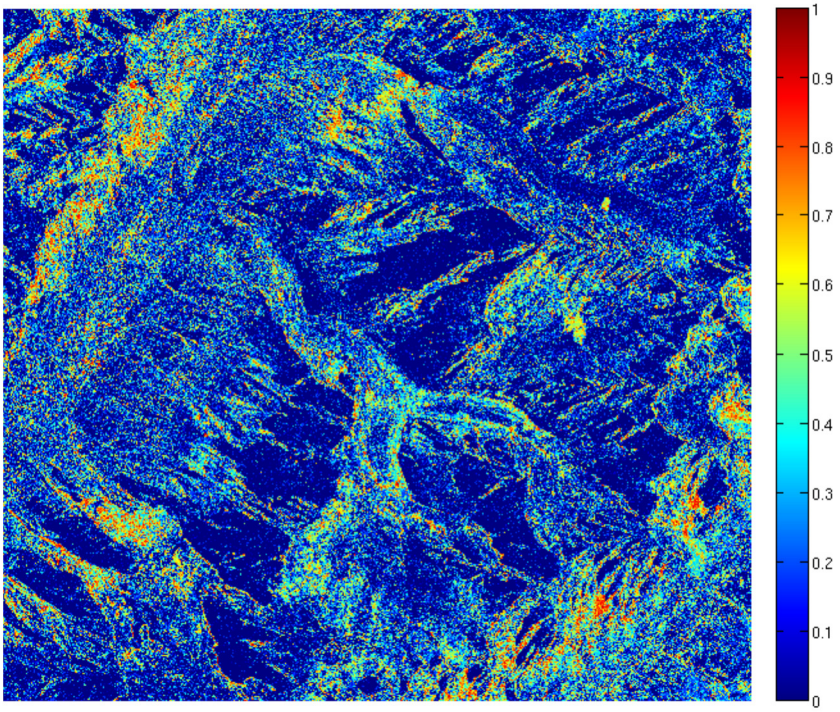

(a)

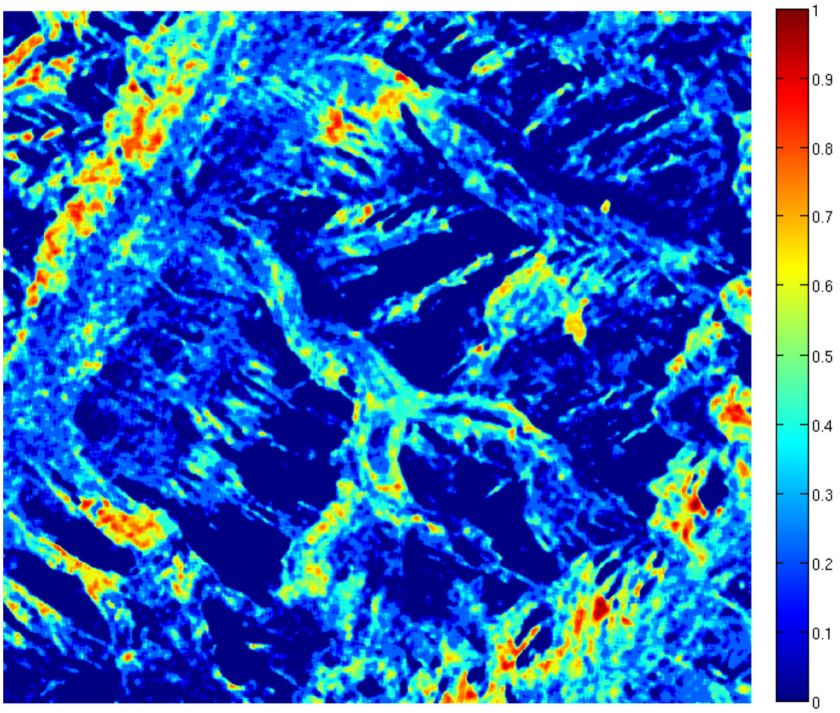

(b)

Figure 6.7: Map of change dynamics at Chamonix Mont-Blanc obtained with dualPol Sentinel-1 image time series using Wishart test; (a) Before and (b) after the proposed spatial filtering strategy.

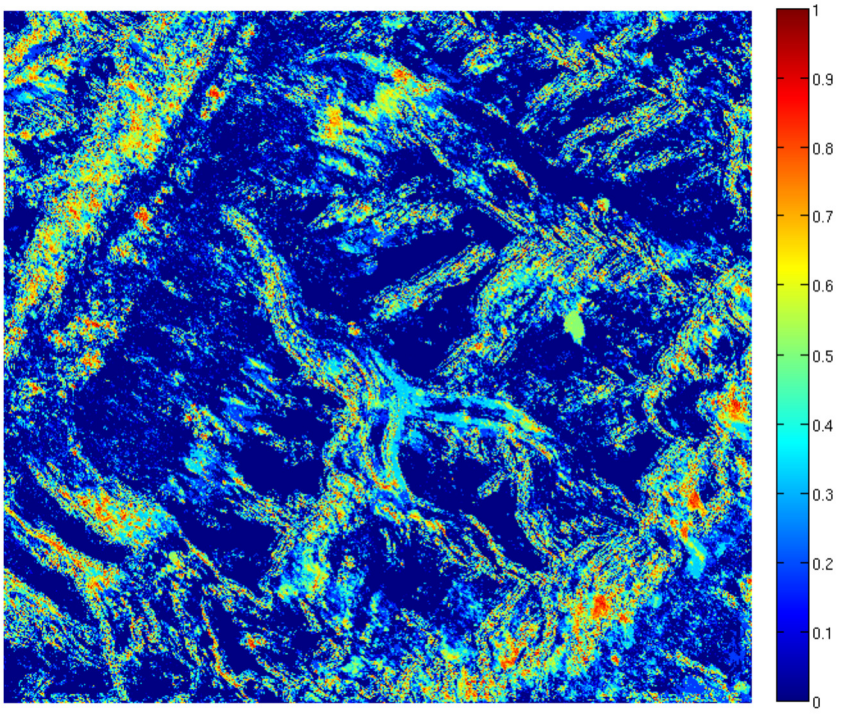

(a)

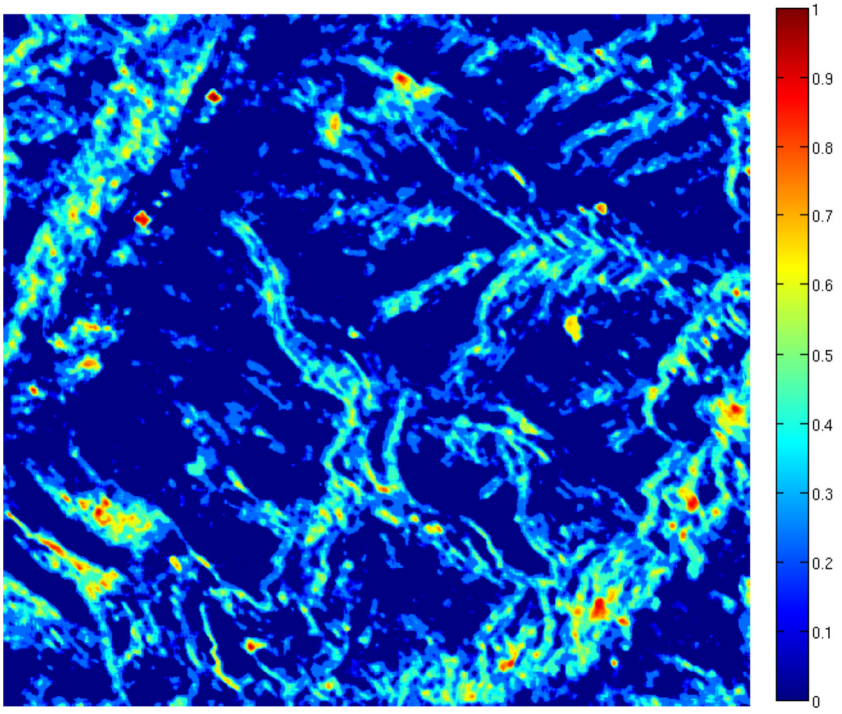

(b)

Figure 6.8: Map of change dynamics at Chamonix Mont-Blanc obtained with dualPol Sentinel-1 image time series using wavelet transform framework and Wishart test. (a) Before and (b) after the proposed spatial filtering strategy.

Wavelet decomposed time series: Another way to derive directly a sufficient regularization result and an analysis on multiresolution performed in addition is to use a wavelet framework as proposed in Section 5.3.1.1. Thanks to the wavelet decomposition, the result in Fig. 6.8 (a) is less noisy and the regularization strategy seems less useful (Fig. 6.8 (b)) in this case. Fig. 6.9 shows maps of change dynamics with

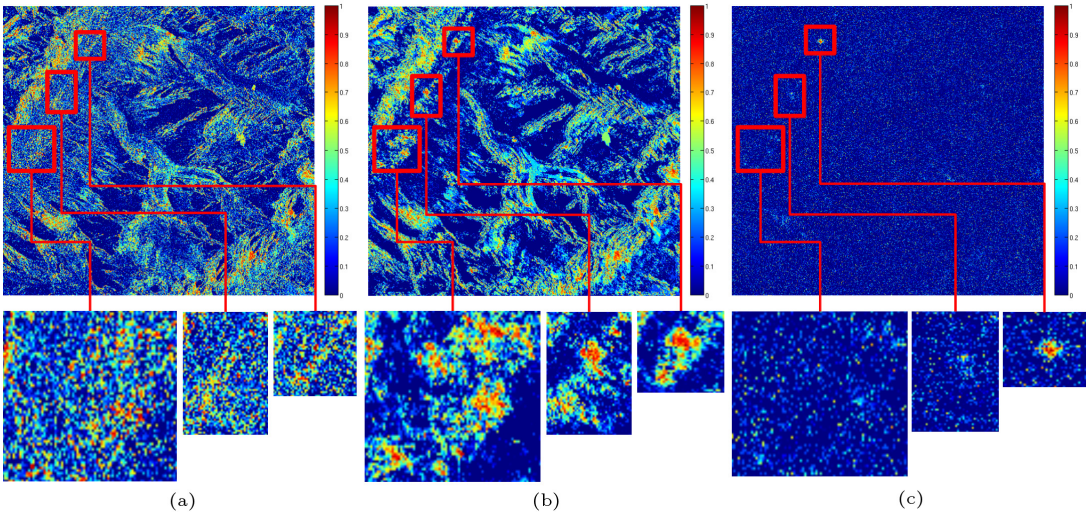

Figure 6.9: Map of change dynamics from ρ indexes over the dual-pol Sentinel-1 time series of the (a) original image time series, (b) the approximation subband time series and (c) the detail subband time series.

different subbands of wavelet decomposition. Indeed, in the case where similarity tests are performed on original time series (without SWT) (Fig. 6.9 (a)), the map of change dynamics presents all kind of changes in the time series, from important changes at dynamic change areas to small changes due to coregistration errors, lack of radiometric calibration, speckle, etc. However, indexes of change dynamics ρ computed at dynamic change areas are much higher than those of weak changes occurring sparsely in the time series (about 0.8 vs 0.4). When using the approximation subbands (Fig. 6.9 (b)), we can observe that non-significant changes have almost disappeared from the map of change dynamics. This map shows the changes of low spatial frequencies (trend changes). When using only detail subbands, maps of change dynamics in (Fig. 6.9 (c)) demonstrates sparsity of change information, the map shows the changes of high frequencies. This can be explained by the sparse synthesis of a high-frequency oscillatory texture: approximation images at J levels are decomposed into sparse wavelet representations. The use of the same similarity measure (the Wishart distance in this case) on approximation images and original images can give different change detection results. Looking at the zooms in Fig. 6.9, we can see that there are some villages, towns like Chamonix and Argentière structured and detected as dynamic change areas on the map obtained by wavelet decomposed images (both approximation images and detail images) with

high indexes ρ (about 0.8). Whilst, the map obtained by original images looks noisy and indexes ρ at these areas are lower ($\simeq 0.5$) with some points of high ρ.

Dual-pol ALOS-PALSAR image time series over Merapi volcano test-site

With ALOS-PALSAR dataset of Merapi volcano, the map of change dynamics (Fig. 6.10) is also relevant. In this time series, only two acquisitions relate to the eruption of the volcano. Index of change dynamics at eruptive deposits area is equal to 0.18. The interval between two consecutive acquisitions in the time series is not always 46 days, some intervals are even over 9 months and 1 year, so that it is not adapted for monitoring the progressive changes (at cultivated area, for instance) by this dataset. However, it has been recorded that indexes of change dynamics at the cropland (rice fields) are about 0.4, and the most dynamic area of this study region is the village area with indexes of change dynamics about 0.6 due to human activities.

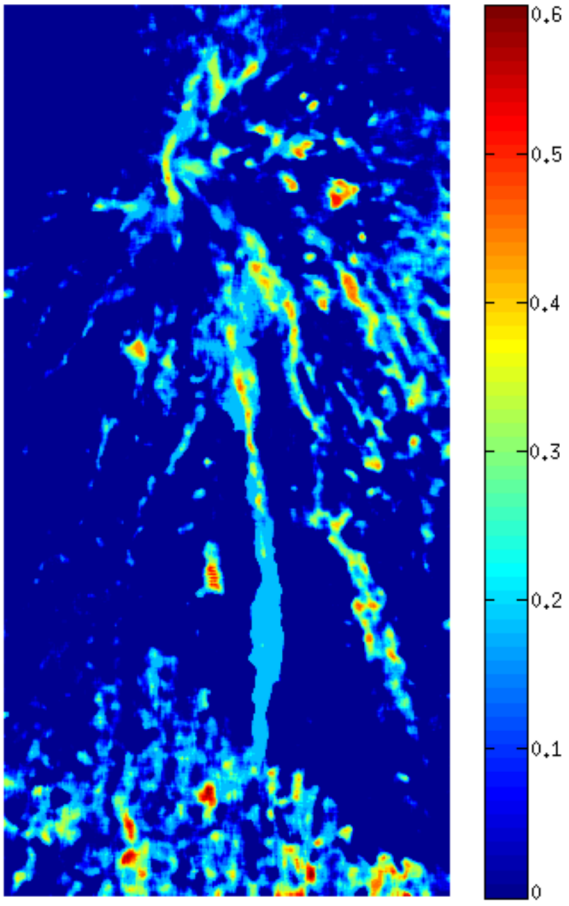

Figure 6.10: Map of change dynamics at Merapi volcano test-site obtained with dual-pol ALOS-PALSAR image time series.

It is worth noting that in our change analysis results derived with ALOS-PALSAR data, the map of change dynamics (Fig. 6.10) is sensitive to all kind of changes in all images of the time series. Therefore, abrupt changes appearing in short periods (e.g. eruptive deposits) as well as progressive changes in cultivated area occurring along the time series are presented with different level of change dynamics. Whilst the information brought by the 2-length change map (Fig. 6.4) relating to eleventh image is different and more specific. It allows the end user to discriminate specific changes due to the eruption of the volcano from other areas affected by regular evolution.

6.3 Conclusions

Spatio-tempral information in CDMs is exploited to perform two different tasks of change analysis in SAR image time series: multitemporal change detection with the possibility to focus on d-length changes of a specific date, and analysis of change dynamics of an area which reveals global changes occurring along the time series. Experimental results confirmed the effectiveness of the proposed approach.

The proposed approach for the detection of d-length change is relevant when changes affect a certain number of dates in the dataset. The high accuracy (90.09% with limited errors: 4.21% false alarms, 16.46% missed alarms and 9.91% overall errors) of change map obtained on an abrupt change due to volcanic eruption shows that the proposed combination of pair-wise change maps improves the performance of the final change map.

The index of change dynamics is computed on the change occurrence in the time series. The spatio-temporal map based on this index thus reflects reliable information for investigating the behavior and the trend of the feature evolutions on the region of interest. The maps of change dynamics obtained over the two test-sites are relevant, they reveal dynamic zones of large study areas. Then we can focus on zones where changes often occur. Over Chamonix Mont-Blanc test-site, in general, dynamic zones are the three glaciers, in particular at the serac fall and crevasses where textures vary in SAR images due to slope ruptures. Over Merapi volcano test-site, the indexes of change dynamics at eruptive deposits area (object of interest) reflect correspondingly the number of acquisition dates related to the eruption of the volcano (two dates in the ALOS-PALSAR time series). The most dynamic areas at this test-site are regions affected by human activities (villages, cropland, rice fields, etc.).

CDMs are constructed before the speckle removal in order to avoid smoothing change information in the time series. For other exploitation purposes of datasets that require the speckle reduction or for the visual interpretation of images, one can use CDMs to select samples for a multitemporal filtering process. A nonlocal temporal filter called CDM-based filter will be introduced in the next chapter.

Chapter 7

Nonlocal temporal filtering

Contents

Most multitemporal filtering methods use all pixels or consecutive sub-sequences of pixels at the same spatial coordinate of the time series to estimate filtered values [Quegan *et al.* 2000], [Coltuc *et al.* 2000], [Ciuc *et al.* 2001]. By this way, the presence of changes in the time series is not concisely taken into account in the filtering process and may lead to the spatial and temporal degradation of filtered values. Temporal neighborhoods identified in CDMs, can provide nonlocal temporal samples for the filtering process. Another application of CDM is dedicated to the multitemporal filtering of SAR/PolSAR image time series which can overcome the above problem of smoothing change information in filtering process. In this chapter, a temporal adaptive filtering based on CDM is proposed and its properties and effectiveness are then illustrated through the experimental results for both single- and multi- polarization SAR datasets (i.e., HH TerraSAR-X time series and quad-pol RADARSAT-2 time series).

7.1 Multitemporal filtering for SAR/PolSAR image time series

7.1.1 CDM-based filter

CDM2 provides for each pixel a spatio-temporal neighborhood involving unchanged pixels in each pixel pile. The CDM-based filter proposed hereafter aggregates the unchanged pixels by using the mean statistics to obtain filtered values, i.e.,

$$\hat{\mathcal{I}}_t(i,j) = \frac{1}{N_{\Psi_t(i,j)}} \sum_{k=1}^{N} \left(1 - \hat{M}_{t,k}^{w}(i,j)\right) \mathcal{I}_k(i,j) \tag{7.1}$$

where $N_{\Psi_t(i,j)}$ is the number of elements in the set $\Psi\left(\mathcal{I}_t(i,j)\right)$ selected from CDM 2 (defined in Eq. (5.3)).

Samples of neighborhoods provided by CDM2s for the filtering process are homogeneous (in CV tests) or similar (having low values of KLD or WD measure). Nonlocal temporal mean filter proposed in this thesis aims at removing speckle while preserving changes, details, texture, etc., by taking advantage of redundancy and similarity of these neighborhoods.

7.1.2 Filter properties

The estimator given by Eq. (7.1) has some notable properties.

1) $\hat{\mathcal{I}}_t(i,j)$ is the standard maximum likelihood estimator of the mean value applied to nonlocal temporal neighborhood, using only the selected pixels (pertaining to the unchanged class). In the context of PolSAR data, this is the estimator to obtain $N_{\Psi_t(i,j)}$-look complex covariance or coherency matrix from $N_{\Psi_t(i,j)}$ independent temporal 1-look samples.

2) It limits spatial and temporal degradation in the filtered images thanks to the consideration of changes in the area of interest in the filtering process (the estimator uses only the selected temporal information in the averaging process), therefore change information is not smoothed while filtering.

3) At observed pixel pile (i,j), if it is purely unchanged, then the filtered value $\hat{\mathcal{I}}_t(i,j)$ is equal to the temporal mean value of the pile. On the opposite, if a pixel in the pile (i,j) is totally different from all other pixels of the pile, then the filtered value $\hat{\mathcal{I}}_t(i,j)$ is equal to the original value $\mathcal{I}_t(i,j)$. This implies that there is no filtering effect for changed pixel, as expected, for preserving the change information.

4) Considering a time series including N uncorrelated SAR images of L-looks, the equivalent number of look (ENL) of the filtered image $\hat{\mathcal{I}}_t(i,j)$ is expected to reach $N_{\Psi_t(i,j)} \times L$-looks.

7.2 Multitemporal filtering results

To illustrate the proposed filter and the behavior of CDM in providing change information for the filtering process, experimental works are performed on two time series: a set of 25 single polarization TerraSAR-X images and a set of 7 quad-polarization RADARSAT-2 images.

7.2.1 Single polarization SAR image time series filtering

7.2.1.1 Filtering results

As described in Section 5.3, the selected similarity test for TerraSAR-X data is the CV test with a small analysis window when using spatial information, in order to

preserve the very high spatial resolution of the data.

For homogeneous regions such as grass, Fig. 7.1 (a) and (b) show that the proposed filtering operator can detect unchanged pixels in each pixel pile effectively. CDM 2 detects more unchanged pixels than CDM 1 does. The profiles of filtered time series using CDM 1 and CDM 2 in Fig. 7.1 (c) are quite correlated to the one of original time series but the dynamic range of amplitude pixel values in filtered time series are reduced due to the averaging process of the filter. It means that speckle noise is also reduced significantly.

In the case of isolated targets such as a car in the parking, there is only one date (one image) in which an object appears at a certain location. The pixel at the object location of that date is completely different from other pixels in the pixel pile. After filtering, the pixel value of the object is preserved as illustrated in Fig. 7.2.

Looking into Fig. 7.3, the reduction of speckle in filtered image helps us to see clearly details of the parking with small cars, which cannot be distinguished in the original image. Fig. 7.4 reveals another interesting point of this filter: it removes well speckle in unchanged areas but it almost avoids filtering moving areas. The filtering reduces the speckle in the stable rock area, whereas in the glacier area, original and filtered images look quite similar. In this area, glacier pixel values in the time series change from date to date, and each point on this surface moves more than one pixel between different acquisitions. Therefore, the filter which is based on averaging unchanged pixels detects very few unchanged samples for the averaging process.

7.2.1.2 Performance Assessment

The performance of a multitemporal filter is assessed through noise reduction, spatial information (texture, edge, feature, size, etc.) and temporal information (change) preservation. Histograms of CDMs at different characteristic regions in Fig. 7.5 illustrate that the proposed filter well preserves changes. To evaluate the size of temporal neighborhoods used in the CDM-based filtering, we compute the "histogram" of CDMs of an area that shows the averaged number of unchanged pixels provided by CDM2s over that area. At a stable grass area, almost all pixels in piles of this area are unchanged; on the average, the CDM2 histogram mode highlights that approximately 20 filtered values are temporal mean of the whole pixel piles. With the piles of forest area where pixels change seasonally leading to some radiometric changes (unfiltered) and some unchanged sequences in each pile, the mode of the number of unchanged pixels of piles is about 17. At a moving area, about 7 original pixels are unfiltered in general, and the mean values of small numbers of samples are calculated to derive the rest of the filtered values.

To assess speckle reduction and spatial information preservation, the proposed filter is compared with another multi-temporal filtering approach proposed by Quegan et al. [Quegan *et al.* 2000] by employing two image quality assessment metrics:

- equivalent number of look (ENL): this is the degree of averaging in SAR multilooking process;

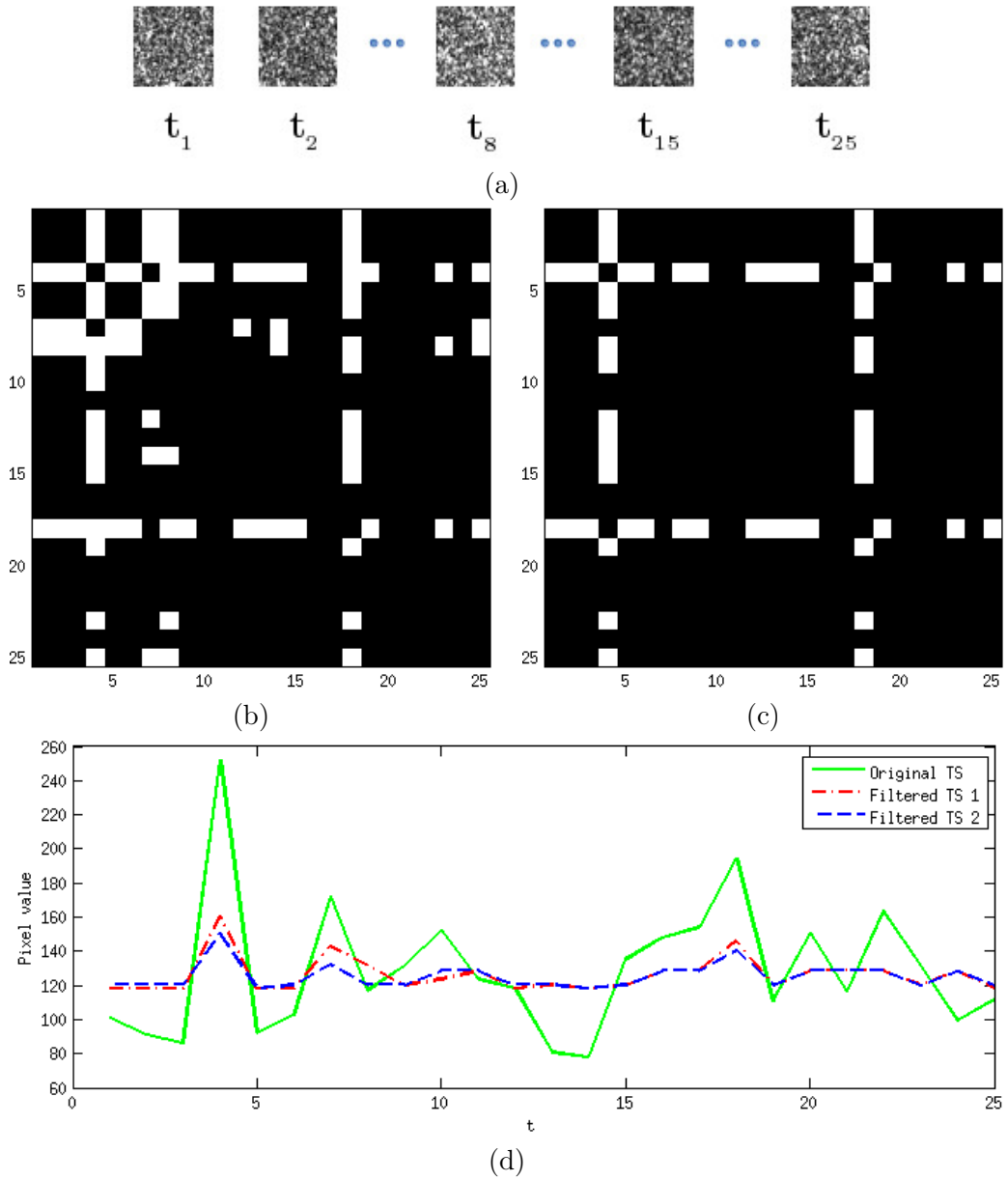

Figure 7.1: CDM-based filter speckle reduction at homogeneous region. (a) A pixel pile at grass (homogeneous region); (b) CDM 1; (c) CDM 2; (d) temporal profiles of original time series (TS) in solid line, filtered TS using CDM 1 (filtered TS 1) in dash-dot line and using CDM 2 (filtered TS 2) in dashed line.

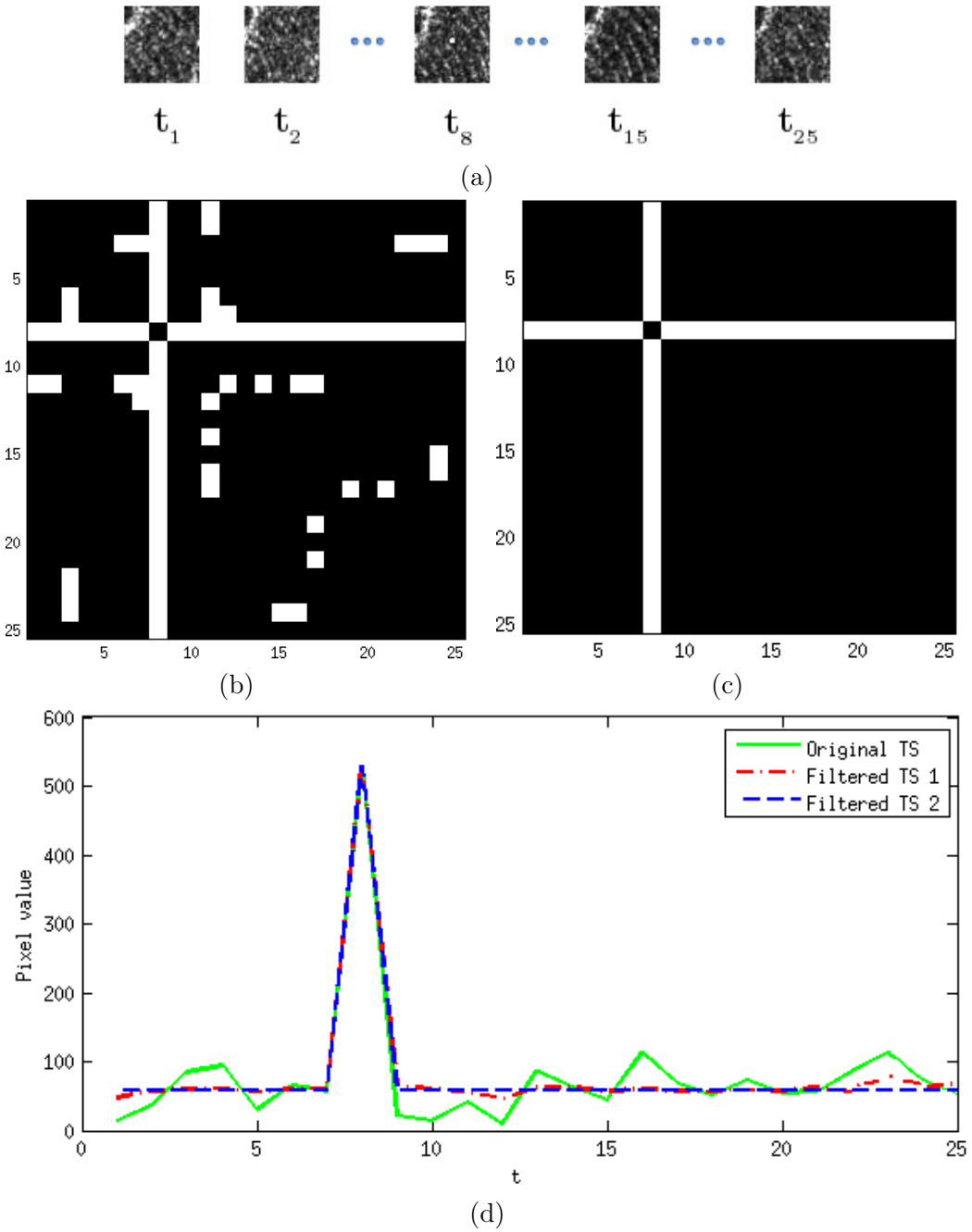

Figure 7.2: CDM-based filter change preservation of an isolated target. (a) A car appears in the parking on date 8; (b) CDM 1; (c) CDM 2; (c) temporal profiles of original time series (TS) in solid line, filtered TS using CDM 1 (filtered TS 1) in dash-dot line and using CDM 2 (filtered TS 2) in dashed line.

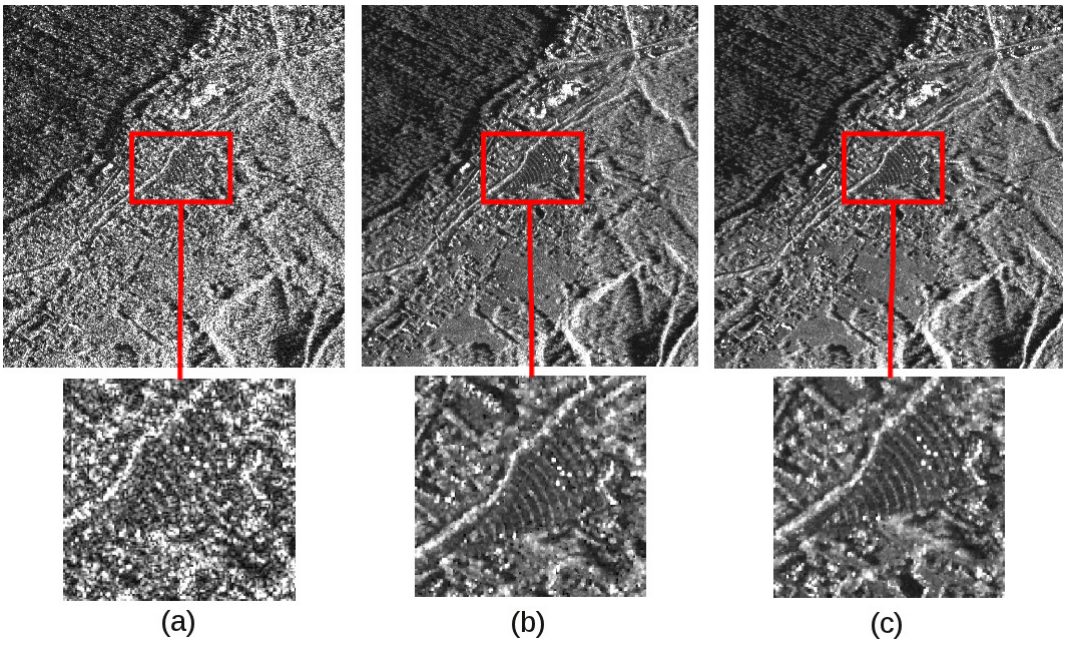

Figure 7.3: Filtering results at parking test-site. (a) Original image (08/27/2009); (b) Filtered image using CDM1 and (c) CDM2.

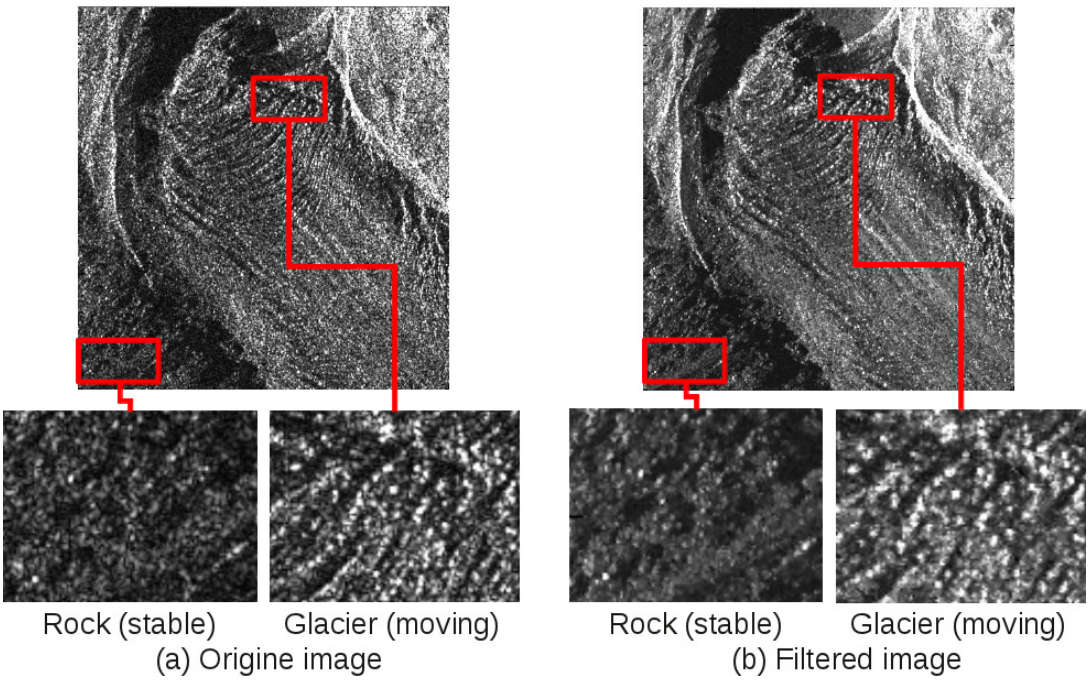

Figure 7.4: Filtering results at glacier test-site, image acquired on 09/03/2011.

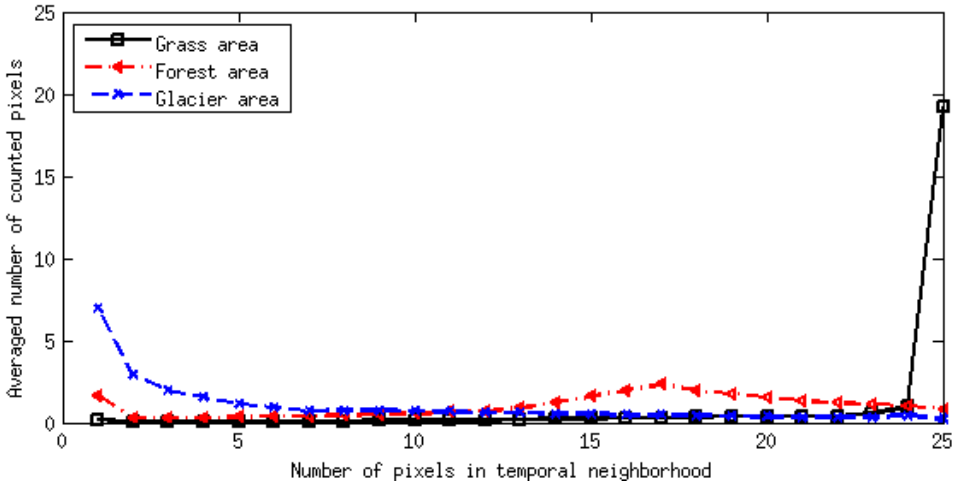

Figure 7.5: Histograms of CDM2s at different characteristic regions.

Table 7.1: Image quality indexes. Equivalent number of look (ENL) and blind/referenceless image spatial quality evaluator (BRISQUE) indexes between QF filter and CDM-based filter. (Image quality indexes of the proposed method are in italics and mean values are in bolds).

No	ENL			BRISQUE	
	Origin	QF	CDMF	QF	CDMF
1	0.93	2.71	*12.43*	34.32	*29.76*
2	0.89	2.80	*12.28*	33.51	*29.63*
3	0.87	2.78	*13.55*	36.12	*28.58*
4	0.88	2.64	*13.64*	34.21	*28.98*
5	0.85	2.39	*12.45*	34.31	*30.67*
6	0.95	3.04	*12.88*	34.59	*28.34*
7	0.91	2.67	*13.24*	33.69	*29.30*
8	0.93	2.70	*12.73*	33.80	*29.71*
9	0.84	2.36	*13.44*	34.17	*28.79*
10	0.93	2.88	*13.37*	34.98	*27.93*
11	0.94	3.00	*10.79*	35.27	*28.77*
12	0.87	2.56	*13.84*	33.31	*27.15*
13	0.92	2.78	*13.42*	34.23	*26.75*
14	0.93	2.71	*12.38*	35.28	*27.95*
15	0.98	3.12	*13.26*	35.73	*27.72*
16	1.00	3.07	*13.15*	34.49	*26.70*
17	0.97	3.03	*11.40*	33.70	*28.11*
18	0.92	2.91	*10.89*	32.80	*30.24*
19	0.96	2.99	*13.65*	35.11	*28.03*
20	0.97	3.08	*11.83*	35.61	*27.26*
21	0.94	2.74	*11.38*	34.24	*28.23*
22	0.91	2.86	*13.53*	35.16	*27.41*
23	0.94	2.87	*13.40*	34.37	*27.79*
24	1.02	3.27	*12.93*	35.59	*28.30*
25	0.88	2.68	*13.28*	33.65	*27.09*
Mean	**0.92**	**2.83**	***12.76***	**34.49**	***28.37***

- and blind/referenceless image spatial quality evaluator (BRISQUE) model [Mittal *et al.* 2012]. BRISQUE model quantifies possible losses of "naturalness" in the image due to the presence of distortions, and it has a value between 0 and 100 (0 represents the best quality).

Table 7.1 presents ENL and BRISQUE indexes of filtered time series obtained by Quegan's Filter (QF) and CDM-based Filter (CDMF). CDMF time series' ENLs increase significantly in comparison with ENLs of the original time series and are much higher than those of the QF time series. BRISQUE indexes of the CDMF time series are at good level and slightly better than those of the QF time series results.

7.2.2 Polarimetric SAR image time series filtering

7.2.2.1 Filtering results

The RADARSAT 2 data set is used to experiment CDMF on PolSAR image time series. The threshold selection of this data set is an empirical approach based on the Wishart distances of training samples of 4 classes which can be observed in the study region: homogeneous area (like grass), forested area, urban area and glacier area (cf. 5.3.1.2). For the comparison purpose, we use two adaptive spatial filters: refined Lee [Lee *et al.* 1999] and IDAN [Vasile *et al.* 2006] filters.

As in the single polarization case, Fig. 7.6 (a) shows that the profile of CDMF time series is correlated to the original time series' one but the fluctuation range of SPAN image pixel values is decreased, speckle is thus also reduced, while the two spatial filter seem to smooth original values. The profile at an isolated target (Fig. 7.6 (b)) shows that after filtering, the value of pixel where change appeared is preserved as keeping change information. At glacier area where the surface moves, just a few samples are detected as unchanged (see Fig. 5.14 (b)), so the temporal characteristic is preserved after the averaging process.

Filtered images in Fig. 7.7 illustrate that the proposed method reduces speckle significantly while preserving detail features of original images. A visual comparison with IDAN filter (Fig. 7.7 (b)) and refined Lee filter (Fig. 7.7 (c)) shows that these filters have some blurring effects, whereas CDM-based filtered image (Fig. 7.7 (d)) presents textures with small details which cannot be distinguished in the original image.

7.2.2.2 Performance Assessment

Table 7.2 provide a quantitative evaluation and comparison of the proposed approach with refined Lee and IDAN filter. ENL criterion on SPAN images (formed after covariance matrix filtering) is employed to assess noise reduction, and feature/texture preservation is assessed by BRISQUE model on the RGB images formed by the three amplitude images in the Pauli basis. According to the ENL indexes, it can be seen that the filtering level of the two spatial filters varies on each image whilst

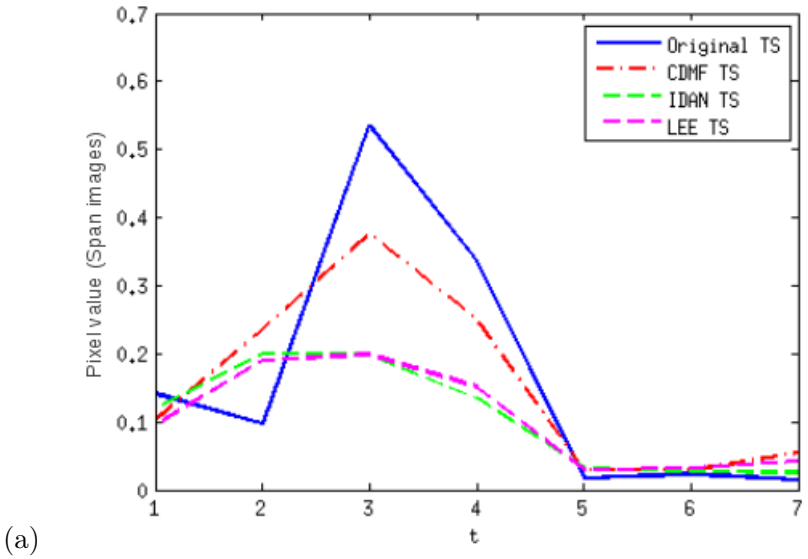

(a)

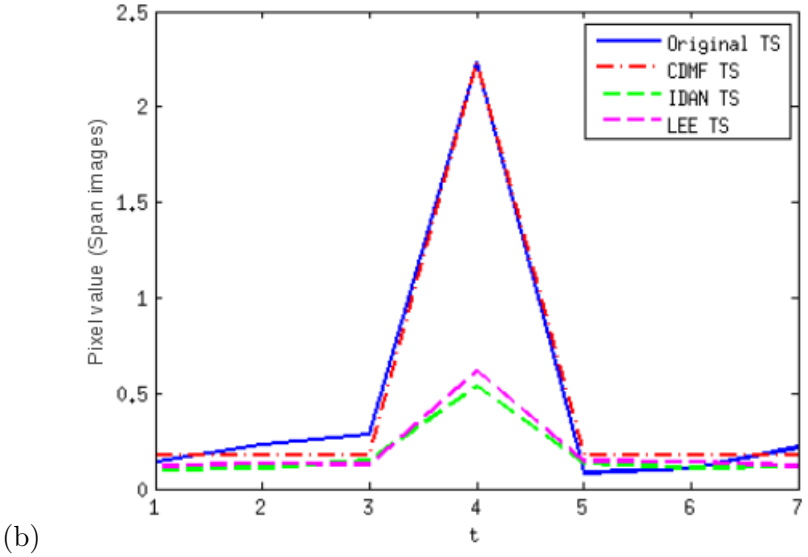

(b)

Figure 7.6: Time series' profiles of RADARSAT 2 SPAN image time series for different filtering. (a) at a homogeneous area, the profile of CDMF time series is correlated to the one of original time series but the fluctuation range of SPAN image pixel values is reduced; (b) at an isolated target, the value of pixel where change appeared is preserved after filtering.

CDMF results are quite stable over the time series. But CDMF's ENL mean value is slightly lower than the one obtained with the two spatial filters. On the other hand, CDMF preserves feature information well according to BRISQUE indexes, the closer this index to 0, the better filters preserve features.

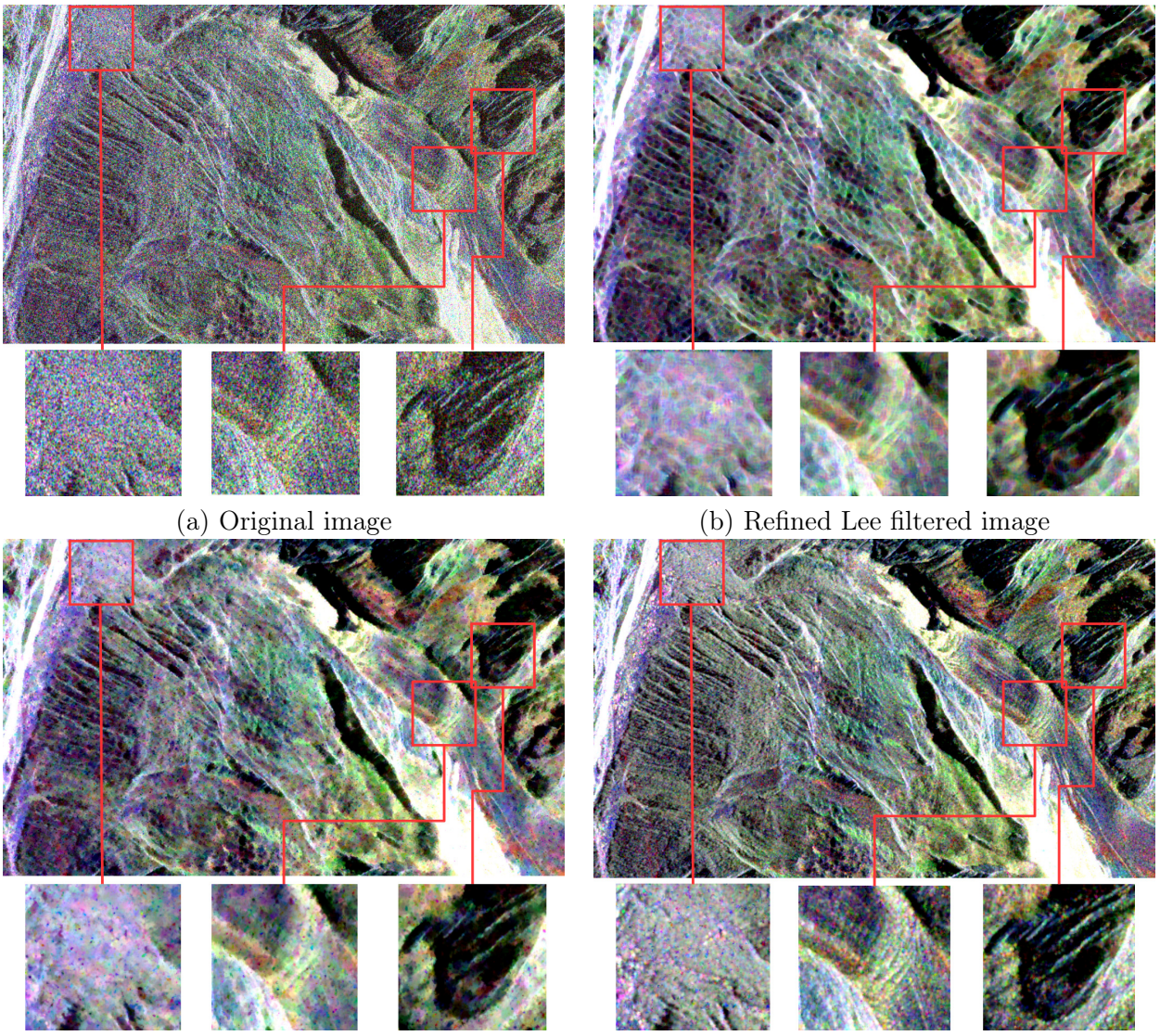

(a) Original image (b) Refined Lee filtered image

(c) IDAN filtered image (d) CDM-based filtered image

Figure 7.7: Filtering results of RADARSAT-2 image acquired on January 29, 2009 in the Pauli basis

7.3 Conclusions

The CDM is used as a preprocessing to identify changes and perform nonlocal temporal filtering that preserves sharp change transitions. The CDM-based filter exploits the determination of changed and unchanged pixels, aggregates only unchanged pixels for the averaging process. Indeed, for a heterogeneous scene composed of stable and dynamic areas, multitemporal filtering is not guaranteed to be performant if the information of change detection is not taken into account. This filter can work

Table 7.2: Image quality indexes. Equivalent number of look (ENL) and blind/referenceless image spatial quality evaluator (BRISQUE) indexes between refined Lee filter, IDAN filter and CDM-based filter. (Image quality indexes of the proposed method are in italics and mean values are in bolds).

No	**ENL (SPAN image)**				**BRISQUE (Pauli basis image)**		
	Origin	**LEE**	**IDAN**	**CDMF**	**LEE**	**IDAN**	**CDMF**
1	1.21	16.16	17.43	*7.67*	31.84	32.71	*22.72*
2	1.14	6.80	8.61	*7.21*	31.26	30.56	*22.88*
3	1.10	6.71	6.93	*7.95*	30.06	31.33	*21.08*
4	0.96	4.46	4.78	*6.65*	34.68	35.32	*24.07*
5	1.42	10.71	10.65	*9.25*	35.78	36.53	*23.75*
6	1.34	10.23	12.57	*9.75*	41.82	37.89	*27.57*
7	1.62	12.12	8.97	*9.98*	42.71	37.35	*27.96*
Mean	**1.26**	**9.60**	**9.99**	***8.35***	**35.45**	**34.53**	***24.29***

both with single polarization and multi-polarization time series. This is an essential application in the context where approaches of multitemporal filtering for PolSAR images are rare.

The experimental results have shown that the proposed approach reduces speckle significantly in comparison with other multitemporal filters while preserving detail features: edges and changes. With short time series, CDM-based filter reduces speckle less than spatial filters because when changes occur from date to date, less unchanged temporal samples are available for the filtering process. Spatial filters usually aggregate large numbers of spatial samples for the filtering. Thus they achieve stronger speckle reduction, but also have blurring effects and possible losses of information of original images. The proposed filter has very little impact on moving areas. This advantage allows images including stable and moving areas to be filtered without losing characteristics of moving areas, that are very important in monitoring their evolution and simultaneously reducing speckle at other areas of images. For instance, in the time series over the heterogeneous Chamonix Mont-Blanc test-site, details and change features such as cars in the parking (in very high resolution time series), serac fall and crevasses at glacier areas are preserved after filtering.

Chapter 8

Conclusions and perspectives

Contents

8.1 Summary

The thesis has addressed the problem of change information extraction and filtering of multitemporal SAR data. In general, with a large amount of available multitemporal SAR images, we have to deal with the selection of suitable work scale, spatial resolution of SAR data, the method to analyze the data and the complexity in processing SAR data.

In this thesis, we first presented the fundamental concepts for the analysis of SAR image time series, including the principles and characteristics of SAR and PolSAR images, the test of statistical model fit of several given distributions to SAR data. Then the state-of-the-art about the filtering and the change detection of SAR and PolSAR data was reviewed in order to provide a general view about techniques and the development trend of these works. Afterward, the study areas and the datasets used in the experimental works as well as some prepocessing steps of these data were introduced.

In the next parts of the thesis, we have proposed a framework based on Change Detection Matrix (CDM) for analyzing changes in SAR image time series. An original method is proposed for the construction of spatio-temporal information matrix containing changed and unchanged information of the time series. We then analyzed the properties of the proposed matrix in order to highlight the information provided by the matrix. After that, the proposed CDMs have been exploited to perform different tasks:

- multitemporal change detection with different kinds of changes by the combination of multitemporal pair-wise change maps to improve the performance of change detection result;
- analysis of change dynamics in the observed area, which allows the investigation of temporal evolution of objects of interest;

- nonlocal temporal filtering of SAR/PolSAR image time series, which allows the temporal adaptive filtering in order to avoid smoothing change information in the time series.

8.2 Contributions

In this thesis, we focused on the development of processing methods (change detection, multitemporal filtering) and the analysis of multitemporal changes occurring in SAR/PolSAR image time series. The main contributions of our works are:

1) The thesis has proposed and developed a framework for simplifying the change analysis of SAR image time series. The proposed CDM is built to determine changed and unchanged pixels in the time series. This approach can be used with many kinds of SAR data, such as amplitude/intensity SAR, dual-/quad-polarization SAR, etc. The CDMs provide useful information for different tasks: multitemporal change detection, analysis of change dynamics, multitemporal filtering.

2) We have demonstrated the potentials of the proposed approach on four datasets over two heterogeneous test-sites: Chamonix Mont-Blanc, France and Merapi volcano, Indonesia, with different types of changes (i.e., seasonal evolution, glaciers, volcanic eruption, etc.). Observations of these test-sites are acquired on four SAR images time series from single polarization to full polarization, from medium resolution to high, very high resolution: 25 ascending TerraSAR-X HH images, 7 descending RADARSAT-2 full polarization images and 11 descending dual-pol/VV Sentinel-1 images over Chamonix-MontBlanc, France, where the seasonal evolution of glaciers and mountains can be observed, and a time series of 11 ascending ALOS-PALSAR dual-pol images over Merapi volcano, Indonesia during a period including the 2010 eruption. The obtained experimental results have illustrated the relevancy of the proposed method.

3) The proposed CDM-based filter is a temporal adaptive filter that can overcome the difficulty of most multitemporal filtering approaches: they use all pixels or sub-sequences of consecutive pixels in pixel pile for the filtering process. The proposed filter based on the nonlocal temporal mean operator, aggregates only unchanged pixels for the averaging process to derived filtered value. This filter works with both single polarization and multi-polarization time series. With PolSAR data, this is the multilooking process using independent temporal/spatio-temporal samples to estimate multilook complex covariance or coherency matrix. This is an important advantage of the proposed method to preserve polarimetric information of backscattering targets while samples for the multilook process are often taken from boxcar spatial neighbors of the considered pixel. Experimental filtering results on Chamonix Mont-Blanc demonstrate that it operates effectively at heterogeneous areas, reduces signif-

icantly speckle while preserving detail features: edges and changes (no filtering effect at moving areas: crevasses, serac fall, etc.).

4) The appearance of CDM reveals the possible changes in time for each pixel in a pixel pile, this highlights changes for an easy interpretation. It can analyze and express several types of change (six hypotheses are arisen, cf. Section 5.3.2): temporal stability, dirac change, step change, ramp change, periodic change and chaotic change.

5) Multitemporal change maps (all possible pair-wise change maps of the time series) obtained from CDMs allow the fusion of change information to improve the change detection performance. The proposed combination for the detection of d-length change is relevant when changes affect a certain number of dates in the dataset. The experimental result shows high change detection accuracy of change map obtained on an abrupt change due to the eruption of Merapi volcano in 2010.

6) The proposed index of change dynamics is computed on the change occurrence in the time series. The map of change dynamics expresses all possible changes in the time series. This map allows the investigation of temporal evolution of objects of interest in the study area. The experimental results over the two test-sites show the relevancy of the proposed approach in change analysis of SAR image time series. Over the Chamonix Mont Blanc test-site, at first, we have investigated the whole test-site on the medium resolution Sentinel-1 dataset at feature level to detect dynamics zones. Then we have focused on zones where changes often occur using high resolution TerraSAR-X dataset at pixel level. On this test-site, dynamic zones are the main glaciers, in particular at the serac fall and crevasses. Over Merapi test-site, the indexes of change dynamics also reflect reasonably the temporal evolution of objects on the area.

8.3 Perspectives

The works presented in this thesis open several perspectives to improve the obtained results as well as perspectives to extend the CDM framework to perform other tasks.

1) In this thesis, we have used three thresholding approaches: adaptive threshold for the CV test, the KI threshold and the empirical threshold. The use of the KI and empirical approaches still present some limitations: high false alarm rate for the KI threshold, and time consuming, expensive cost (field work step) for the empirical one. For the regulation of the false alarm, thresholding methods like KI, CFAR detection, etc., can be applied to asymptotic PDFs for similarity measures which can be derived referring to [Salicru *et al.* 1994] (for KLD) and to [Frery *et al.* 2014] (for Wishart distance). Besides that, an automatic approach according to the expected false alarm rate also can be used to set the threshold.

2) We have proposed in this thesis the combination of pair-wise change maps related to a reference date. In perspective, among the methods proposed for the fusion of change information detected in CDM, we can cite the evidence theory of Dezert-Smarandache (DSmT) [Smarandache & Dezert 2004] or of Dempster-Shafer (DST) [Shafer 1976].

3) The obtained results when using SWT give the potential of applying wavelet transform in CDM approach. In this aspect, the application of geometric wavelets (sparse transform) to SAR images, where speckle can be seen as random fields in a multiplicative interaction environment, could reveal more interesting patterns in change analysis of SAR ITS.

4) The CDM analysis in Section 5.3.2 shows that many kinds of change can be detected in CDMs. In this thesis, we have obtained two different change analysis products from CDM: binary change map and map of change dynamics. We can also classify change types occurring in CDMs by giving a threshold value for each type of change and then derive a change classification map.

5) With the availability of InSAR and Pol-InSAR data, the proposed CDM method can be extended to these data in order to benefit the advantages of interferometry which characterizes the way of electromagnetic wave and of polarimetry which provides accurate information on the interactions between the radar wave and the target.

The new Sentinel mission has provided useful free access data to observe changes on the Earth's surface. The launch of Sentinel-1,-2 B (scheduled in 2016) together with the existing Sentinel-1,-2 A makes it possible to acquire very high temporal resolution image time series for both SAR and multispectral data. Long time series, thus, can be obtained to build large CDMs. This allows pattern analysis in CDM structure (blocks, periodicities, etc.) to better understand the temporal evolution of features of interest in long-term. This also allows the temporal information retrieval to ease search for a specific content from the diverse image database.

For the Earth observation, various types of remote-sensing images for a given region are available, i.e., data from optical, infrared, microwave sensors, etc. Each type of data has its advantages and limitations. The fusion of multisource remote sensing data can take advantages of these data for extracting information. In this thesis, we have addressed the issue of change analysis from single source image time series. A future research axis consists in using multitemporal data from complementary images/spectral bands of the same or different sensors for the same area to get more information and to enhance the quality of scene evolution interpretation. For instance, the fusion between descending and ascending SAR data can avoid the impact of layover effect, or the fusion between SAR and optical images, e.g., SAR, panchromatic and multispectral data (Sentinel-2), can extract useful information from these data to classify different types of change.

List of publications

International journal papers

[J1] **Lê, T. T.**, Atto, A. M., Trouve, E., Solikhin, A., Pinel, V., 2015. *Change detection matrix for multitemporal filtering and change analysis of SAR and PolSAR image time series.* ISPRS Journal of Photogrammetry and Remote Sensing, vol. 107, 64–76.

[J2] **Lê, T. T.**, Atto, A. M., Trouve, E., Nicolas, J.-M., 2014. *Adaptive multitemporal SAR image filtering based on the change detection matrix.* IEEE Geoscience and Remote Sensing Letters, vol. 11, no. 10, 1826–1830.

International conference papers

[C1] **Lê, T. T.**, Atto, A. M., Trouve, E., 2015. *Change analysis using multitemporal Sentinel-1 SAR images.* In proceedings of IEEE International Geoscience and Remote Sensing Symposium (IGARSS), Milan, Italy, 4145–4148.

[C2] **Lê, T. T.**, Atto, A. M., Trouve, E., 2015. *Change analysis of dual polarimetric Sentinel-1 SAR image time series using stationary wavelet transform and change detection matrix.* In proceedings of 8$^{\text{th}}$ International Workshop on the Analysis of Multitemporal Remote Sensing Images (Multitemp), Annecy, France.

[C3] **Lê, T. T.**, Atto, A. M., Trouve, E., 2014. *Adaptive multitemporal filtering of polarimetric SAR images.* In proceedings of IEEE International Geoscience and Remote Sensing Symposium (IGARSS), Quebec, Canada, 4560–4563.

[C4] **Lê, T. T.**, Atto, A. M., Trouve, E., Nicolas, J.-M., 2013. *Temporal adaptive filtering of SAR image time series based on the detection of stable and change areas.* In proceeding of 5$^{\text{th}}$ TerraSAR-X / 4$^{\text{th}}$ TanDEM-X Science Team Meeting, Oberpfaffenhofen, Germany.

[C5] **Lê, T. T.**, Atto, A. M., Trouve, E., 2013. *Schatten matrix norm based polarimetric SAR data regularization. Application over Chamonix Mont-Blanc.* In proceeding of International Workshop on Science and Applications of SAR Polarimetry and Polarimetric Interferometry (POLinSAR), Frascati, Italy.

[C6] Atto, A. M., Mercier, G., **Lê, T. T.**, Trouve, E., 2012. *Vector and matrix l_p norm in polarimetric radar filtering.* In proceedings of IEEE International Geoscience and Remote Sensing Symposium (IGARSS), Munich, Germany, 1441–1444.

Appendix A

Speckle SAR statistical model fit

A.1 Goodness of fit test

The χ^2 test of fit is employed to test the goodness of fit for all given distributions. Each sample distribution is divided into m classes, which are taken to be successive intervals in the range of the data. The probability of an observation coming from each class can be easily calculated from the assumed distribution function, and is denoted by p_{oi}, $i = 1, 2, ..., m$. The observed frequency in each class is given by n_i, with n total observations.

The χ^2 test statistics:

$$\chi^2 = \sum_{i=1}^{m} \frac{(n_i - np_{0i})^2}{np_{0i}} \tag{A.1}$$

follows approximately a χ^2 distribution with $(m - c - 1)$ degrees of freedom, where c is the number of estimated parameters. Lower χ^2 indicates a better fit.

A.2 The fit of specified distributions to experimental SAR data

This test aims at illustrating the fit of several standard probability distributions usually used for modeling SAR data (i.e., Rayleigh, Gamma, Nakagami), as well as Log-normal and Weibull distributions to SAR amplitude data. We consider ERS 1 (3 looks), TerraSAR X (single look) and Sentinel-1 (single look) images.

First, each image is divided into sub-images, then with each sub-image, maximum-likelihood estimation (MLE) is used to estimate parameters of several of above-mentioned distributions. Finally, the fit of each distribution to the given data is tested by χ^2 for each distribution.

The fits of given PDFs to the histograms of tested images are shown in Fig. 2.4, Fig. 2.6 and Fig. 2.7. Here, we provide the χ^2 statistics for the tested data.

Table A.1 indicates that the gamma distribution is the best fit to the experimental ERS 1 data. With the whole set of sub-images, Gamma and Log-normal can be selected as suitable distributions to model the observed SAR images. The Log-normal and Weibull have the χ^2 statistics which are quite similar, but the Log-normal's performance is better than Weibull's on modeling the data.

In the cases of TerraSAR-X and Sentinel-1 data, Gamma distribution fits well the histogram of homogeneous area but with heterogeneous area, Log-normal dis-

Number of sub-image	Gamma	Log-normal	Nakagami	Rayleigh	Weibull
1	567.7	1479.7	742.5	2889.2	4699.0
2	1106.7	6893.7	6297.1	45869.4	6089.4
3	493.0	5866.9	10812.7	46507.3	7227.6
4	98.8	3456.1	11156.4	40715.4	8574.4
5	144.5	4191.9	14027.4	37441.4	9576.6
6	357.5	2437.6	1540.5	1948.4	**12.0**
7	948.9	**1.3**	4480.0	132.9	13.2
8	96.8	1063.7	567.4	5438.8	548.3
9	258.1	4176.4	9570.6	40554.1	7434.4
10	113.2	3738.0	11173.5	37386.5	12888.4
11	**25.2**	388.7	67.7	2948.4	1032.9
12	83.0	1277.3	1767.9	4129.2	35.6
13	142.1	40.4	244986.5	24.2	201.7
14	371.3	5298.4	8802.1	46260.6	7601.5
15	290.8	4741.6	11612.6	42540.8	9668.9
16	570.6	5748.9	10083.0	47636.5	10203.0
17	1433.9	8298.3	12652.3	34217.6	8054.9
18	193.0	2623.1	3937.7	7383.7	1159.9
19	84.4	315.2	**20.6**	3797.6	1214.4
20	86.3	1652.4	2957.4	38403.2	3441.7
21	971.2	6154.5	15138.8	35743.9	10030.7
22	2596.1	11032.3	8237.4	27732.9	4266.2
23	3163.1	12495.0	7301.3	34907.9	5227.0
24	76.8	497.4	26.7	4412.5	659.2
25	38.8	1840.7	1079.4	2514.9	352.2
26	1046.7	4002.1	65143.2	19769.8	16198.3
27	201.8	2632.7	26668.1	9869.0	8684.7
28	808.1	7260.3	13963.1	833.3	1094.5
29	691.8	3638.2	2949.7	**6.8**	52.6
Mean	**588.3**	3904.9	17509.1	21448.8	5042.9

Table A.1: χ^2 statistics for each distribution of all sub-images of ERS 1 image

Number of sub-image	Gamma	Log-normal	Nakagami	Rayleigh	Weibull
1	1553.00	290.2	14546.5	48063.0	1836.3
2	360.2	389.7	86.3	763.7	**785.2**
3	1286.3	525.4	13828.4	19571.0	3691.4
4	4749.2	189.4	7396.4	13765.5	3756.0
5	2074.3	247.4	**11.0**	1200.1	1909.6
6	608.9	652.7	367.7	34487.1	1514.7
7	**117.9**	1648.4	10299.0	14104.4	779.9
8	4958.5	173.2	12668.8	28128.0	6233.5
9	9285.1	111.3	54049.2	3.5	5930.6
10	3482.1	298.5	15596.6	114657.2	1591.6
11	31769.1	718.7	63051.1	68.9	10335.1
12	1673.6	738.5	30.4	12.2	4389.6
13	10445.6	843.8	56635.8	**1.1**	18356.8
14	6216.6	63.4	19278.9	129124.5	3642.2
15	1879.5	299.9	45886.6	64.9	883.7
16	6836.9	**41.5**	46714.4	13.9	4087.7
Mean	5454.4	**452.0**	22527.9	25251.8	4357.7

Table A.2: χ^2 statistics for each distribution of all sub-images of TerraSAR-X image

Number of sub-image	Gamma	Log-normal	Nakagami	Rayleigh	Weibull
1	3370.1	200.0	55182.2	**26.2**	2762.3
2	1368.0	568.8	10719.6	6766.4	**1084.4**
3	**393.3**	3003.5	11783.9	3708.8	1822.0
4	732.3	2408.4	27729.3	9453.3	3405.6
5	11879.4	70.2	1091.5	11454.6	4399.9
6	12985.0	1271.4	16917.3	92728.9	8742.1
7	1014.4	434.4	9850.1	8510.7	3875.9
8	4641.5	562.0	18477.4	23410.9	1577.0
9	5474.2	**26.4**	**1.1**	1464.2	2697.8
10	10597.7	39.0	104493.9	510.3	5184.2
11	19329.5	326.4	21854.6	234388.8	8180.6
12	29232.9	1057.0	30.8	1606.8	17382.8
13	4666.6	114.6	22663.1	49679.3	7349.3
14	1048.6	250.9	52.6	620.0	1942.2
15	4930.9	2023.8	6430.2	64982.9	1886.1
16	2408.3	125.6	2123.2	10704.0	1833.8
Mean	7129.5	**780.1**	19337.5	32501.0	4632.9

Table A.3: χ^2 statistics for each distribution of all sub-images of Sentinel-1 image

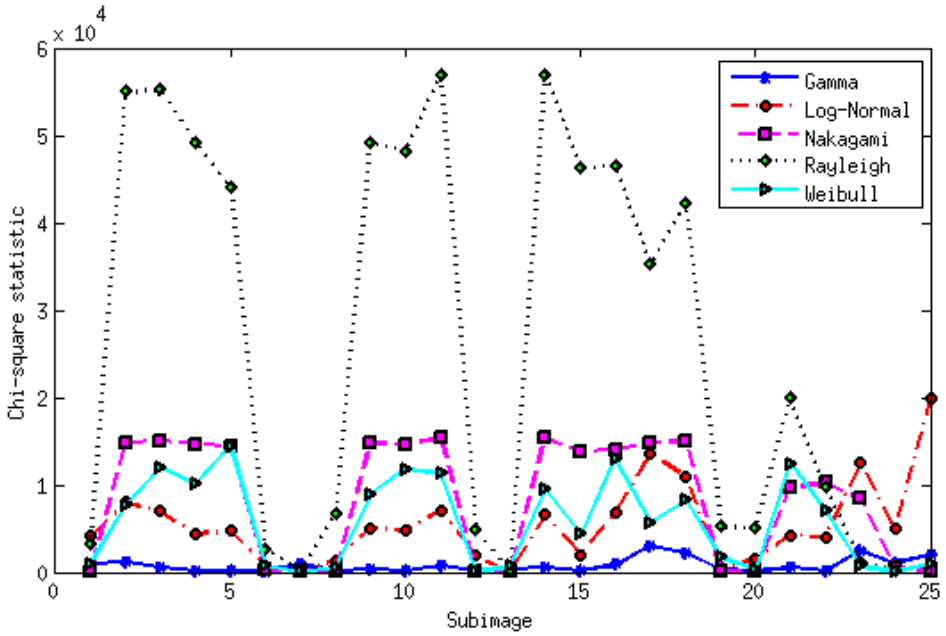

Figure A.1: χ^2 statistics of all sub images of ERS 1 image.

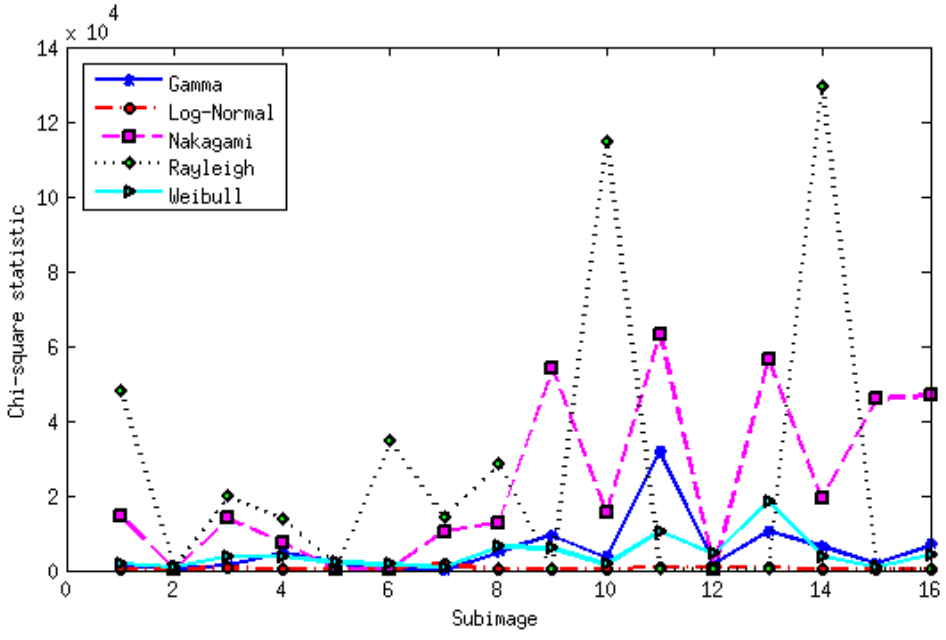

Figure A.2: χ^2 statistics of all sub images of TerraSAR-X image.

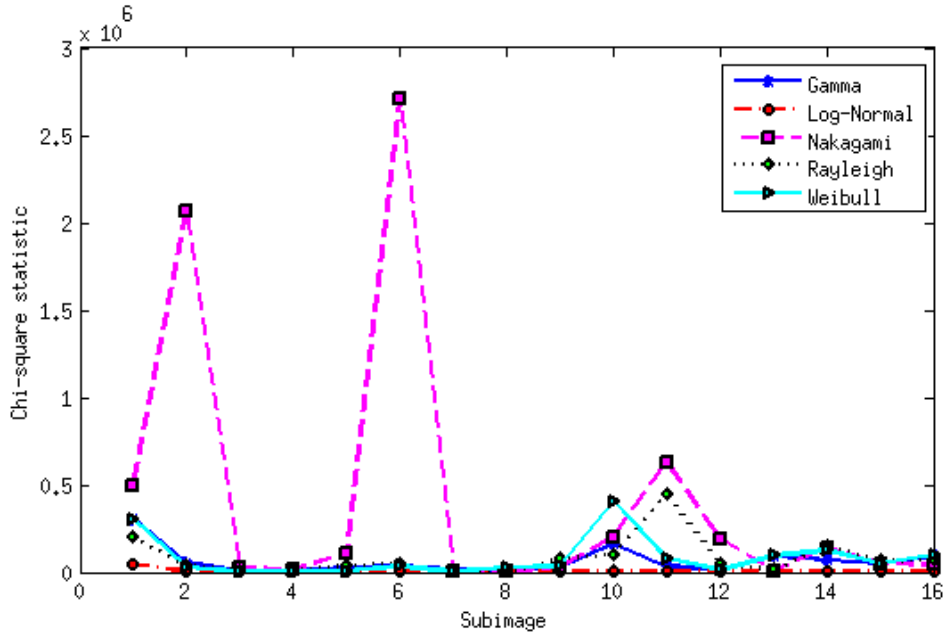

Figure A.3: χ^2 statistics of all sub images of Sentinel-1 image.

tribution is more suitable. Chamonix Mont-Blanc is a heterogeneous test-site with mountainous terrain and glacier on high mountains, therefore, among the tested distributions, the Log-normal is the most appropriate one for these data as Table A.2 and A.3, as well as Fig. A.2 and A.3 have demonstrated.

Appendix B

Résumé étendu

Contents

B.1 Introduction

B.1.1 Contexte et motivation

Le lancement de nombreux satellites imageurs Radar à Synthèse d'Ouverture (RSO ou SAR) permet d'observer régulièrement la surface de la Terre et d'obtenir des informations sur ses propriétés physiques. L'imagerie SAR est une modalité active d'imagerie basée sur les micro ondes électromagnétiques. De ce fait, cette modalité

est insensible à l'éclairement solaire et à la couverture nuageuse, avantage significatif par rapport aux techniques traditionnelles d'imagerie optique lorsqu'on souhaite avoir une série temporelle d'images régulièrement espacées et toutes exploitables. Par conséquent, les systèmes SAR sont appropriés pour la surveillance de structures terrestre en mode opérationnel.

Des années 1990s à nos jours, de nombreux systèmes ont été mis en orbite autour de la terre. Ces systèmes fournissent de longues séries temporelles d'images SAR de hautes ou très hautes résolutions spatiales sur des grandes régions de la surface de la Terre. De nombreuses applications ont été étudiées dans la littérature, en exploitant les informations contenues dans les séries d'images SAR. Parmi ces applications, on peut citer la classification des régions, la cartographie et la surveillance des cultures, la cartographie et l'analyse des caractéristiques naturelles de la forêt, la couverture neigeuse, le déplacement des glaciers, la surveillance des catastrophes naturelles comme les inondations, les dégâts de tsunami, etc.

Durant la période [1990, 2005], le lancement des satellites de première génération [ERS-1 en 1991 et ERS-2 en 1995 (ESA), JERS en 1992 (NASDA), RADARSAT-1 en 1995 (CSA) et ENVISAT en 2002 (ESA)] a rendu disponibles, des images SAR et InSAR (pour 'SAR interférométriques'), ces dernières permettant, par différentiation, d'obtenir des mesures d'élévations ou de déplacement.

L'exploitation d'images SAR polarimétriques (PolSAR) satellitaires a été rendu possible par le lancement des satellites SAR de nouvelle génération. Des systèmes satellitaires tels que ALOS en 2006 (NASDA), RADASAT-2 (CSA) et TerraSAR-X en 2007 (DLR), opérant en bandes L, C et X, respectivement, offrent ainsi des images SAR avec polarisations doubles (SAR dual-pol) ou quadruples (SAR quad-pol). La polarimétrie exploite différentes configurations des ondes électromagnétiques en émission (imagerie active) et réception (mesures du champ électromagnétique rétrodiffusé par la surface du sol) afin de caractériser les informations liées à la nature de la surface ou du volume des diffuseurs au sol. La combinaison des techniques polarimétriques et interférométriques permet alors des caractérisations d'élévations ou de déplacements surfaciques/volumiques de différentes structures terrestres, en prenant avantages des potentiels de ces 2 techniques.

Du fait des avancées récentes en sciences appliquées et en technologies des capteurs, les satellites SAR de la génération future devraient continuer à fournir des images SAR avec une résolution spatiale supérieure, une résolution temporelle plus fine, différentes bandes spectrales et de multiples polarisations, etc.

Les capteurs SAR disponibles actuellement offrent déjà plusieurs modes d'imagerie avec des caractéristiques différentes. Avec le mode ScanSAR (RADARSAT-2, TerraSAR-X, Sentinel-1), des données acquises peuvent couvrir de très grandes zones (jusqu'à 400 x 400 km possible). Cependant, lorsqu'on cherche à couvrir une très grande zone, la résolution spatiale est diminuée (contrainte de limitation de ressources telles que la puissance des processeurs et la mémoire embarquée). Au contraire, le mode d'acquisition Spotlight (TerraSAR-X, Cosmo-Skymed) offre des données à moins de 1 m de résolution mais à 10 km de couverture. Ces capteurs produisent fréquemment des images sur une même scène avec des cycles répétés de

courte durée, par exemple, 11 jours pour des images TerraSAR-X et 12 jours pour Sentinel-1A (lancé en 2014) (avec un passage à 6 jours lorsque Sentinel-1B sera lancé en 2016 pour former une constellation 1A-1B).

L'imagerie SAR est très pertinente aussi bien pour les structures à grande échelle (tectonique, zones affectées par des tremblements de terre, déplacement de glaciers, etc.) que pour les petites structures (applications urbaines caractérisées par une forte densité de petites structures complexes). Cependant, son exploitation nécessite de faire face aux problèmes de la diversité des données :

- en termes de modalité d'acquisition (SAR, interférométrie, polarimétrie, interférométrie polarimétrique, bandes multiples, etc.),
- en termes de conditions d'acquisition (orbites ascendantes et descendantes, différents angles de vue, etc.),

ainsi que la dimensionnalité (chaque image dans la base de données de grande taille, soit parce que la résolution est fine, soit parce que la structure terrestre observée est de grande dimension, soit les 2 en même temps). Dans ce contexte, comment extraire et exploiter efficacement les informations contenues par des images SAR ?

Dans cette thèse, nous nous intéressons à l'utilisation des images SAR multi-temporelles afin d'en extraire des informations spatiales et temporelles. Nous nous concentrerons sur le développement de méthodes de traitement exploitant l'axe temporel (détection de changement et le filtrage multi-temporel), et leur application aux séries d'images SAR mono-composantes et polarimétriques (multi-composantes).

B.1.2 Contenu principal de la thèse

Dans cette thèse, nous présentons tout d'abord les concepts fondamentaux de l'analyse des séries temporelles d'images SAR. Ces concepts comprenent les principes et les caractéristiques des images SAR et PolSAR, les distributions statistiques des données SAR et les tests d'évaluation. Puis, l'état de l'art sur le filtrage et la détection de changement dans les données SAR et PolSAR est proposé afin de fournir un aperçu global sur les techniques et les approches en cours de développement pour résoudre ces problèmes. Puis, les zones d'étude et les ensembles de données utilisés dans les travaux expérimentaux, ainsi que certaines étapes de pré-traitement de ces données sont introduites.

Ensuite, nous proposons un cadre d'analyse fondé sur la Matrice de Détection de Changements (CDM) pour analyser les changements dans les séries chronologiques d'images SAR. Une méthode originale est proposée pour la construction de matrice d'informations spatio-temporelle contenant des décisions sur la nature stable ou changeante des pixels de la série chronologique. Nous proposons une analyse des propriétés de la matrice CDM proposée pour mettre en évidence les informations fournies par la matrice. Après cela, les CDM proposées sont exploitées pour réaliser différentes tâches :

1) la détection de changement multitemporel avec différents types de changements,

2) l'analyse de la dynamicité de la zone observée,

3) le filtrage nonlocal temporel des séries chronologiques d'images SAR/PolSAR.

B.2 Outils fondamentaux d'images SAR/PolSAR

B.2.1 Principes et distributions SAR/PolSAR

Un système SAR transmet et reçoit de manière cohérente, des signaux électromagnétiques. Pour chaque échantillon de la donnée SAR, l'amplitude et la phase du signal d'écho sont représentées par une valeur complexe comprenant une partie réelle (en phase) et une partie imaginaire (en quadrature) de l'écho reçu. Le but de cette partie (cf. Chapitre 2) est de présenter les principaux éléments permettant la compréhension des principes généraux de l'imagerie SAR. Nous nous concentrons sur la formation des données SAR mono et multi-composantes et leurs propriétés statistiques.

La pertinence de plusieurs distributions de probabilité (Gamma, Rayleigh, Nakagami, Log-normale et Weibull) pour modéliser les données d'amplitude SAR (TerraSAR-X, Sentinel-1, ERS-1) est ainsi validée en utilisant les tests statistiques du χ^2 (cf. Appendix A). On montre ainsi que dans les zones homogènes, les données d'amplitude SAR issues de la génération actuelle de satellites sont le plus souvent caractérisées par des distributions non-Rayleigh (comme la Log-normale), contrairement aux données des générations précédentes. Pour les données PolSAR, nous retenons comme c'est le cas classiquement, la distribution de Wishart en raison de sa robustesse (elle est basée uniquement sur les statistiques du second ordre).

B.2.2 Bibliographie sur le filtrage et la détection de changements SAR/PolSAR

La détection de changements spécifiques dans un certain intervalle de temps en utilisant des données SAR doit prendre en compte le bruit de chatoiement qui rend l'exploitation de l'imagerie SAR difficile. Dans cette section, nous fournissons un aperçu général du filtrage de chatoiement et la détection de changements dans les séries chronologiques d'images SAR. En particulier, les mesures de similarité couramment utilisées pour les données SAR et PolSAR, ainsi que celles qui seront exploitées dans cette thèse sont également fournis (cf. Chapitre 3).

Dans la littérature, la plupart des approches de filtrage multitemporel proposées ne prend pas explicitement en compte la présence de changements dans la série temporelle. Par conséquent, les échantillons sélectionnés pour le processus de filtrage sont souvent des voisins spatio-temporelles locaux du pixel analysé. Cela est de nature à lisser les informations de changement et conduire à la dégradation radiométrique, spatiale et temporelle des valeurs filtrées. Dans les approches récentes de détection de changement et l'analyse des changements sur SAR ITS comme l'approche MDDM [Atto *et al.* 2013] et l'approche MIMOSA [Quin *et al.* 2014], certains auteurs se concentrent soit sur la localisation spatiale, soit sur la position

temporelle des changements. Dans l'approche MDDM, des changement sont détectées au niveau d'image (pour des images entières ou des imagettes de la série temporelle). La MDDM obtenue pour la série chronologique permet d'observer quand des changements se produisent globalement dans le domaine temporel. Mais on ne peut pas déterminer exactement où ils sont dans le domaine spatial. Alors que dans l'approche MIMOSA, l'utilisation des deux moyennes temporelles permet d'identifier où des changements se produisent, mais sans indiquer à quel moment dans la série. Nous proposons dans cette thèse un cadre pour l'analyse de changement de SAR ITS qui peut surmonter les limitations des filtrages multitemporels et les approches de détection de changements en cherchant à être le plus localisé possible au niveau spatial et temporel.

B.3 Ensembles de données et prétraitement

Pour illustrer l'approche proposée, nous utilisons deux sites d'étude et quatre ensembles de données. Les deux sites d'étude sont : Chamonix Mont-Blanc (France) et le volcan Merapi (Indonésie), avec différents types de changements observables par quatre ensembles de données : 25 images TerraSAR-X de polarisations HH de taille 600×600 pixels sur le parking de grands Montets et 500×500 pixels sur le glacier d'Argentière, 7 images quad-pol RADARSAT-2 de taille 700×1100 pixels, 11 image dual-pol Sentinel-1A (polarisations VV / VH) de taille 1300×1200 pixels, et 11 images dual-pol ALOS-PALSAR (polarisations HH / HV) de taille 1500×750 pixels. Certaines étapes de prétraitement exécutées avant l'extraction d'informations à partir de ces données sont indiquées dans le Chapitre 4.

Le site d'étude Chamonix Mont-Blanc est situé au cœur des Alpes françaises, dans le département de la Haute-Savoie et la région Rhône-Alpes, au sud-est de la France. Ce site test contient des zones hétérogènes, des zones forestières, une partie du Massif Mont-Blanc (zones à géométries variables et glaciers d'Argentière, Mer-de-Glace, Leschaux, Tacul, Bossons et Taconnaz) et la vallée de Chamonix (zone urbaine composée notamment des villages Praz et les Bossons, des villes comme Argentière et Chamonix), voir la figure 4.1 pour une appréciation des caractéristiques de la zone.

Le vocan Merapi est situé à $7°32'26''$S et $110°26'48''$ E, au nord de la ville de Yogyakarta, dans le centre de Java, en Indonésie (Figure 4.2). Il est connu comme étant l'un des volcans les plus dangereux au monde, en raison de son activité éruptive persistante et sa localisation dans des zones densément peuplées. La densité de population dépasse 1400 habitants par km^2 sur les pentes de l'ouest et du sud de ce volcan. Le Merapi est en activité volcanique depuis 1548, produisant régulièrement des coulées pyroclastiques périodiques et des écoulements de lave. De petites éruptions se produisent tous les deux ou trois ans et des éruptions plus importants ont lieu tous les dix à quinze ans et au moins dix-sept éruptions ont causé des décès. Du 26 Octobre au 23 Novembre 2010, la plus grande éruption depuis 1872 a eu lieu avec de nombreux écoulements pyroclastiques sur les pentes densément peuplées du vol-

can, ainsi que du sud-est au sud-ouest. Cette éruption violente a causé le plus grand impact volcanique à la vie humaine, avec plus de 200 décès directs, 2200 infrastructures endommagées, les bâtiments, les zones agricoles, etc., et plus de 400.000 personnes ont été évacuées de la zone affectée. Dans les travaux expérimentaux de la thèse, nous avons utilisé une série temporelle d'images ALOS-PALSAR avant et après certains changements brusques dus à l'éruption volcanique de 2010.

Les caractéristiques principales des quatre ensembles de données utilisées pour les tests sont présentées dans les tableaux 4.2, 4.5, 4.7, et 4.9. Les missions satellitaires et les caractéristiques des systèmes imageurs de chaque ensemble de données sont également présentés dans la Section 4.2.

Une série temporelle d'images SAR peut être acquise à partir d'observations variants avec différents paramètres d'enregistrement, ou à partir d'acquisitions orbites répétitives. Pour des images SAR qui sont très sensibles à l'angle d'incidence locale, nous préférons généralement analyser des séries temporelles acquises à partir des orbites répétitives. Afin d'avoir des images comparables dans une série temporelle, certaines étapes de prétraitement telles que la calibration radiométrique, le recalage et les corrections géométriques, etc., peuvent être effectuées avant de réaliser une analyse spécifique. Les images SAR utilisés dans la thèse sont prétraitées par les deux premières étapes (i.e., la calibration radiométrique par les fournisseurs des données et le recalage au cour de la thèse) qui sont suffusantes pour l'analyse des séries chronologiques. Les résultats expérimentaux peuvent être ensuite géocodées si on souhaite les intégrer ultérieurement dans un SIG (Système d'Information Geographique). Les figures qui illustrent cette thèse sont généralement en géométrie radar (range et azimut) sans subir d'orthorectification qui perturbe fortement l'échantillonage des images.

B.4 Matrice de détection de changement

Dans cette partie, nous présentons une méthodologie pour l'extraction d'informations de changement et le filtrage des données multitemporelles SAR. L'approche proposée vise à construire une matrice de détection de changement (CDM) en utilisant une stratégie comprenant deux étapes. La mise en œuvre de chacune de ces étapes est détaillée dans ci-dessous (voir aussi le Chapitre 5). De surcroît, les propriétés des CDM et leurs potentiels en détection des changements sont également analysés.

B.4.1 Construction de la CDM

Afin de déterminer des changements sur les pixels de la série temporelle d'images SAR, nous proposons de construire une matrice de détection de changement CDM contenant les réponses des tests de similarité croisés: l'élément (t, ℓ) de la matrice renseigne sur la présence de changement entre la date t et la date ℓ au pixel donné.

Pour une pile teporelle de pixels localisés spatialement à la même position donnée, la matrice de détection de changement proposée est construite selon une stratégie comprenant deux étapes (Figure 5.1) :

- La première étape est une analyse bidate : dans cette étape, des tests de similarité sont calculés entre deux dates quelconques de la série à l'aide de fenêtres spatiales, pour obtenir une matrice de détection de changement (CDM 1). Cette matrice contient toutes les réponses de la décision binaire *changement* ou *non-changement* entre chaque paire de dates à la position pixélique de référence.

- La deuxième étape est une analyse multidate : basée sur le résultat de la première étape, cette seconde étape consiste à supprimer les fausses alarmes en re-calculant les mesures de similarité, mais cette fois-ci après avoir construits des voisinages multidates associés à des états de 'non-changement' au sens de la CDM 1 (on remplace ainsi le voisinage spatial de la CDM 1 par un "voisinage" spatio-temporel plus représentatif du pixel car enrichi des valeurs détectées stables dans la pile). Cela nous donne une autre matrice de détection de changement (CDM 2) qui est plus précise et plus creuse que la CDM 1.

B.4.2 Calcul de CDM

Les points le plus critique pour la détermination de la CDM proposée est la sélection d'une mesure de similarité appropriée et celle d'un seuil. Cela dépend de plusieurs facteurs comme le type d'images SAR, leurs résolutions, les caractéristiques de la zone d'étude, *etc.*.

Dans nos travaux, nous avons collecté quatre ensembles de données de différentes caractéristiques sur deux sites tests.

Pour la région Chamonix Mont-Blanc, les données Sentinel-1A collectées ont une résolution de 3,5 m × 22 m (range × azimut). Les données à "haute" résolution, RADARSAT-2 (8 m) et des données à "très haute" résolution, TerraSAR-X (2 m) sont utilisées pour étudier deux zones spécifiques (voir la figure 5.4 et la figure 5.5) : une zone de stationnement (Grands Montets) et une zone de déplacement du glacier (la chute de sérac d'Argentière). Sur cette dernière zone, la surface se déplace d'environs 20 cm/jour (i.e. plus qu'un pixel entre deux dates consécutives dans la série temporelle TerraSAR-X à 11 jours).

Pour le site du volcan Merapi, seules des données ALOS-PALSAR sont disponibles pour l'étude des changements causés par l'éruption de 2010. Après recalage des données utilisées pour chaque tâche d'étude, nous considérons des mesures de similarité et des méthodes de seuilage appropriées pour déterminer les changements dans la série chronologique.

B.4.2.1 Choix de mesures de similarité

Pour la série temporelle d'amplitudes Sentinel-1 sur une zone non-homogène comme Chamonix Mont-Blanc, la distribution Log-normale est plus adaptée à la description des données, voir la section 2.1.3 pour l'analyse comparative de différents modèles statistiques pour les données SAR. Nous avons alors choisi comme mesure de similarité entre 2 lois Log-nomales, la distance de Kullback-Leibler (KLD). La fenêtre

d'analyse qui est retenue pour les tests est de 32×32 pixels après une étape de choix du voisinage.

Avec les données de "très haute" résolution TerraSAR-X, les changements peuvent être analysés au niveau du pixel. En particulier, en zone de déplacement où 1) la surface du glacier se caractérise par une grande différence entre deux acquisitions consécutives (11 jours), où 2) des changements urbains surviennent quotidiennement du fait de l'activité humaine, un petit voisinage spatial est préférable. Nous choisissons donc la fenêtre spatiale carrée d'analyse minimale (pixel central et ses quatre plus proches voisins). Sur un tel petit voisinage, l'utilisation de distribution de probabilité est exclu et nous considérons le Coefficient de Variation (CV) comme mesure robuste d'homogénéité (non-changement) versus hétérogénéité (changements), voir la Section 3.3.2.

Pour les séries quad-pol RADARSAT-2 et dual-pol ALOS-PALSAR, la distance de Wishart donnée dans l'equation (3.14) est retenue pour mesurer la similarité entre vecteurs de nombres complexes. La taille de la fenêtre d'analyse est 3×3 pixels pour les tests utilisant la distance de Wishart.

Pour la série temporelle dual-pol Sentinel-1A, nous appliquons une transformation en ondelettes avant le choix des attributs pixéliques afin de profiter du potentiel multi-résolutions de cette transformée.

B.4.2.2 Choix du seuil

La sélection d'un seuil est une étape cruciale pour discriminer les états "changement" et "non-changement". Sur des zones hétérogènes comme Chamonix Mont-Blanc et Merapi, les images sont plus ou moins affectées par leur relief accidenté. Dans cette thèse, nous adoptons les approches suivantes pour sélectionner le seuil :

- Un seuil adaptatif au nombre d'échantillons est utilisé pour l'analyse de la série temporelle TerraSAR-X dans le protocole de test par CV.
- Le seuil de Kittler-Illingworth (KI) appliqué sur les tests relatifs aux données ALOS-PALSAR et Sentinel-1A (données SAR d'amplitudes et dual pol).
- Un seuil empirique pour l'analyse de la série temporelle RADARSAT-2. Ce seuil est déterminé à partir d'échantillons d'apprentisage provenant du contenu du site d'étude.

B.4.3 Analyse d'une CDM

Pour chaque pile de pixels, nous obtenons une CDM 1 et une CDM 2. L'apparence d'une CDM (Figures 5.9 et 5.10) révèle les changements qui se sont produits sur l'axe temporel pour la localisation spatiale associée au pixel. L'apparence d'une CDM depend : 1) du choix des attributs (moyennes, variances, covariances, lois de probabilité, etc.), 2) du choix de la mesure de similarité entre ces attributs, 3)

du choix du seuil de décision et 4) du contenu de la scène. Nous pouvons cependant observer des formes caractéristiques de certains types de changements sous les hypothèses suivantes (Figure 5.11) :

- H_0 - La stabilité temporelle : pas de changement dans la pile temporelle. La CDM associée à la stabilité est de couleur noire (hypothèse 0, décision 0).

- H_1 - Le changement de type Dirac : un changement se produit dans la série temporelle sur une seule date. Ce genre survient quand le signal temporel radiométrique se comporte comme une impulsion, au bruit de speckle près. La CDM de ce changement résulte en une ligne et une colonne blanches à cette date (sauf sur l'élément diagonale qui vaut toujours 0 par définition). L'exemple dans la figure 5.12 (a) montre qu'une voiture stationne dans le parking des Grands Montets à une certaine date et l'absence de voiture aux autres dates.

- H_2 - Le changement de type échelon : la CDM montre deux bloc noirs, l'un pour l'état stable des d dates avant que le changement et l'autre pour l'état des $N - d$ dates après changement. Le changement est supposé progressif de même intensité. La figure 5.12 (b) montre l'éruption du volcan Merapi dans les deux dernière dates de la série temporelle acquise sous forme de changement échelon.

- H_3 - Le changement de type rampe : un changement progressif d'une magnitude croissante se produit à partir de la date t_k à la date t_ℓ ou à partir de la date t_k et se poursuit. Ce type de changement survient souvent sur des zones cultivées ou du fait de l'érosion du sol/côte (en raison de l'eau et le vent). La magnitude de changements augmente avec la croissance de la végétation ou le degré d'érosion. L'apparence de la CDM de ce changement devrait montrer des blocs noirs régulières correspondant à des périodes de développement de l'objet étudié.

- H_4 - Le changement périodique : un changement progressif de la même magnitude se produit dans une période de la date t_k à la date t_ℓ (stationnarité). La CDM est cyclostationnaire lorsqu'un ou plusieurs de ce type de changement se repète(nt) de manière cyclique. Cette hypothèse est le cas du changement saisonnier.

- H_5 - Le changement chaotique: des changements se produisent avec des magnitudes différentes sur l'axe temporelle. Ce genre de changement décrit souvent l'évolution rapide de la surface (zones de déplacement, par exemple). L'apparence des CDMs dans des zones de déplacement est désordonnée dans notre cas d'étude comme les glaciers avec des structures en mouvement.

Ces caractérisations sont fournies à titre illustratif, d'autres scénarii peuvent être considérés ultérieurement ou selon l'application.

B.5 Analyse de changements

Avec l'approche proposée, nous obtenons des CDMs qui montrent les variations des caractéristiques de chaque pile temporelle de pixel. Selon ces CDM, nous avons une vue générale sur les évolutions de structures (par exemple, des changements lents tels que l'érosion, l'évolution de la végétation, etc., ou des changements brusques comme les catastrophes naturelles : tsunami, tremblement de terre, etc.). L'exploitation de l'information CDM ne se limite pas à la détection temporelle de changements, elle peut en effet être utilisée pour le filtrage multitemporel, la classification, etc. Dans cette section, les informations spatio-temporelles de CDM extraites à partir des séries chronologiques d'images SAR sont d'abord exploitées pour effectuer une analyse de changement (Chapitre 6). Nous obtenons ainsi des cartes de changement binaires intrinsèques à l'état de la zone étudié. De plus, nous proposons un indice de la dynamicité basé sur les informations obtenues dans les CDMs, indice qui permet d'avoir une vue d'ensemble de la nature changeante ou stable de la région observée.

B.5.1 Détection de changement portant sur d-dates

À partir des CDMs d'une série de N images, nous obtenons des cartes de changements temporels entre deux dates de la série (Figure 6.1). Il y a différentes façons d'utiliser ces cartes afin d'avoir un meilleur résultat de la détection de changement. Par exemple, la diagonale offre les cartes de changement entre deux dates consécutives (t et $t+1$). Les colonnes ou les lignes donnent les cartes de changement entre une date de référence t et toutes les autres dates ℓ de la série temporelle, etc. La figure 6.2 (a) montre un changement qui apparaît sur les deux dernières dates de la série et la figure 6.2 (b) illustre un changement qui apparaît à la seizième date et cela, sur une durée de quatre dates.

Le test expérimental de détection de changements est effectué en utilisant les données ALOS-PALSAR. La figure 6.3 montre les cartes de changements entre la date 11 et les autres dates de la série chronologique. En prenant toutes ces informations de changement dans le test de l'équation (6.2), nous obtenons une seule carte contenant les informations de changement liées à l'éruption en date 11, avec $d = 2$.

L'évaluation quantitative du résultat de la détection de changement proposée est présentée dans le tableau 6.2 et le tableau 6.3 en utilisant des échantillons de vérité de terrain. Ils ont été extraits manuellement, sur la base de l'interprétation visuelle des images optique et en se référant aux données terrain par [Charbonnier *et al.* 2013], [Komorowski *et al.* 2013] et [Solikhin *et al.* 2014].

En comparant les résultats de la détection proposée avec les 5638 échantillons de vérité terrain, nous montrons des taux de performance intéressants pour la méthode proposée. Le résultat de détection de changement obtenu a une grande précision (90,09 % de bonnes détections) avec 4,21 % de fausse alarme et 16,46 % de non-détections. La combinaison de toutes les informations acquises dans la série temporelle (à la fois des informations de changement et de redondance) augmente la précision de la détection de changement (en comparaison avec la précision des

résultats de détection de changement entre la date 11 et les autres dates dans le tableau 6.1).

B.5.2 Analyse de dynamicité de changement

B.5.2.1 Indice de dynamicité

Les informations de changement fournies par les CDMs permettent l'étude de la dynamicité des zones observées pour comprendre les tendances d'évolution de la région. Cette dynamicité sera ordonnée des pixels stables (presque toujours au même état) aux pixels instables (en changements permanents ou chaotiques).

Étant donné une pile de pixels à une position spatiale (i, j), nous proposons de définir un indice de la dynamique de changement comme étant la probabilité $\rho(i, j)$ des réponses "changement/non-changement" issues des tests de similarité (voir l'équation (6.4)). L'indice ρ admet des valeurs allant de 0 (purement stable, aucun changement temporel ne se produit dans la série chronologique) à 1 (instabilité temporelle, les pixels associés à toute paire arbitraire de dates sont différents).

Les cartes des indices de dynamicité obtenues en pratique sont affectées par un bruit impulsionnel reflétant des changements non-significatifs, lorsque les CDMs sont construites à l'échelle pixellique comme c'est le cas dans cette thèse. Une étape de régularisation est donc nécessaire pour déduire une carte homogénéisée de la dynamicité de changement. Cette carte est obtenue par une stratégie de filtrages médians et modes récursifs (Les équations (6.5) et (6.6)), voir la figure 6.6 (b) avant régularisation et la figure 6.6 (c) pour le résultat régularisé obtenu.

B.5.2.2 Résultats d'analyse de la dynamicité de changement

Données monocomposantes sur le site Chamonix Mont-Blanc

La série temporelle d'images d'amplitude VV Sentinel-1

La figure 6.5 présente le résultat obtenu avec la série temporelle d'images d'amplitude VV Sentinel-1 par approche KL sur des attributs de lois Log-normale.

La carte de dynamicité représentée dans cette figure montre que les zones dynamiques du site d'étude sont les zones de déplacement de glaciers pour les trois glaciers : Argentière, Mer-de-Glace et Bosson. En particulier, la zone de chute de séracs et des zones de crevasse sont fortement dynamiques, du fait de la rupture de pente qui, conjuguée au déplacement, résulte en une zone presque chaotique.

Nous pouvons observer que la dynamicité varie sur les glaciers, en fonction de la forme et de la couverture de la surface de ce dernier :

- en présence de crevasses et séracs, elle atteint les valeurs maximales ($\rho \simeq 0.8$) là où le flux des glaciers est très rapides (1 m/jour pour les séracs de la Mer-de-Glace et environ 50 cm/jour pour les séracs d'Argentière) ;

- en présence de roches et de débris à la surface du glacier, elle atteint des valeurs moyennes ($\rho \simeq 0.5$) du fait des mouvements de ces différentes cibles

spatialement distribuées et du fait des propriétés de pénétration de l'onde radar (par exemple la neige sèche/humide) ;

- en présent du névé (sur la partie haute des glaciers, dans les zones d'accumulation), elle est généralement inférieure à 0.5 car ces zones sont plus stables.

Aux villages de la vallée de Chamonix, où de nombreuses activités ont eu lieu en Décembre et Janvier (pendant la saison touristique), les indices de la dynamicité sont d'environs 0,6.

Dans cette approche KL, nous avons utilisé une grande fenêtre d'analyse de 32 × 32 pixels. Avec cette grande fenêtre d'analyse, la stratégie de régularisation proposée dans la section 6.2.2 n'est pas appliquée car ce choix de grande fenêtre d'analyse intègre naturellement l'effet de régularisation.

La série temporelle d'images d'amplitude HH TerraSAR-X

Pour l'ensemble de données à "très haute" résolution TerraSAR-X, nous avons choisi une zone spécifique : la zone de chute de sérac du glacier d'Argentière pour l'analyse de la dynamicité au niveau pixelique.

Dans cette zone, les valeurs des pixels du glacier changent d'une date à une autre date, en particulier chaque pixel de cette surface se déplace de plus d'une position entre les différentes acquisitions. La taille de la fenêtre d'analyse spatiale au niveau pixelique comprend le pixel considéré et ses quatre plus proches voisins. Le test de similarité retenu, du fait de ce contexte pixélique d'exploitation, est le test d'homogénéité par CV (cf. 3.3.2.1).

La carte de dynamicité de changement de la zone de chutes de séracs d'Argentière est ainsi obtenue et affichée à la figure 6.6.

Données à 2 composantes

La série temporelle d'images dual-pol Sentinel-1 sur le site Chamonix Mont-Blanc

La figure 6.7 montre le résultat de détection de changement lors de l'utilisation de la série temporelle d'images dual-pol Sentinel-1A avec la distance de Wishart pour le test de similarité. Dans la figure 6.8, nous avons appliqué un scénario de détection différent (via transformation d'ondelettes) pour cette même série temporelle.

La carte de dynamicité de changement de la figure 6.7 (a) est assez similaire à celle de la figure 6.5. Cependant, la distribution de Wishart est utilisée pour le cas dual-pol Sentinel-1A (données vectorielles) à une échelle de traitement pixelique (fenêtre spatiale 3 × 3), tandis que la distribution Log-normale est considérée dans le contexte des données monovariées d'amplitude VV Sentinel-1A, en utilisant une fenêtre spatiale 32 ×32 pixels (niveau patch) pour dériver la carte de dynamicité (voir la figure 6.5).

Les indices de dynamicité de la figure 6.7 (niveau de pixel) sont légèrement inférieurs, dans les zones de déplacement de glaciers, que ceux de la figure 6.5 (niveau patch). La raison est la prise en compte supplémentaire des changements de texture des crevasses dans ce dernier cas.

Discrimination multi-échelle par décomposition en ondelettes :

Une autre stratégie pour éviter l'utilisation de grands patchs tout en étant sensible à la texture est la détection de changements par le biais de la transformée en ondelettes. Du fait de l'utilisation de cette transformée, les résultats présentés à la figure 6.8 (a) sont moins bruités et la stratégie de régularisation supplémentaire semble moins utile (voir la figure 6.8 (b)).

La figure 6.9 montre les cartes de dynamicité de changement avec différentes sous-bandes de décomposition d'ondelettes SWT. Les indices de dynamicité ρ calculés dans les zones dynamiques sont beaucoup plus hauts que ceux associés aux zones de faible dynamique (environs 0,8 versus 0,4).

L'autre avantage de cette transformée est qu'elle permet de discriminer différents types de changements. Dans les sous-bandes d'approximation de cette transformée (Figure 6.9 (b)), nous pouvons ainsi observer des changements de radiométrie moyenne, qui sont non-significatifs (du fait de l'alternance neige fraiche, neige humide, glace, sol nul, etc) si l'on veut étudier le déplacement tandis qu'ils le sont justement en caractérisation de radiométrie moyenne.

Dans les sous-bandes de détail de cette transformée, les cartes de dynamicité (Figure 6.9 (c)) montrent la parcimonie des informations de changement qui surviennent dans les hautes fréquences.

L'utilisation de la même mesure de similarité (la distance de Wishart dans ce cas) peut donc donner des résultats différents de détection de changement selon qu'on cherche des informations basses fréquences (approximations) ou hautes fréquences (détails).

En regardant les zooms dans la figure 6.9, nous pouvons voir qu'il y a des villages, des villes (e.g., Chamonix, Argentière) qui sont détectées comme zones très dynamiques dans les sous-bandes d'ondelettes, avec des indices ρ très élevés (environs 0,8).... alors que la carte de dynamicité obtenue sur les images originales est très bruitée pour permettre une réelle estimation des indices ρ.

Série temporelle d'images dual-pol ALOS-PALSAR sur le site d'étude du volcan Mérapi

Concernant les données ALOS-PALSAR du volcan Merapi, la carte de dynamicité obtenue est également pertinente (Figure 6.10). Dans cette série temporelle, seulement deux acquisitions concernent la période d'éruptions volcaniques. L'indice de dynamicité de changement de la zone éruptive (accumulation de dépôts) est égale à 0,18 (la zone est donc stable en dehors des périodes éruptives). Les indices de dynamicité des zones cultivées (champs de riz) sont d'environ 0,4. La zone la plus

dynamique de ce site est une zone habitée (village) avec des indices de dynamicité moyens de 0,6.

B.6 Filtrage temporel non local

La plupart des méthodes de filtrage multitemporel utilisent des voisinages spatio-temporels connexes pour estimer la valeur moyenne à affecter au pixel. De cette manière, la présence de changements dans la série temporelle n'est pas prise en compte efficacement et cela peut conduire à la dégradation spatiale et temporelle des valeurs filtrées.

Les classes temporelles de stabilité identifiées dans les CDM peuvent fournir des échantillons temporels non locaux à utiliser pour effectuer ce filtrage. C'est ce que nous proposons dans cette section (résumé du Chapitre 7). À parir de cs classes temporelles de stabilité, nous proposons un filtre multitemporel selon l'équation (7.1).

La pertinence de l'approche sera illustrée par les résultats expérimentaux sur deux ensembles de données mono- et multi-polarisation SAR (images d'amplitude HH TerraSAR-X et quad-polarisation RADARSAT 2).

B.6.1 Filtrage multitemporel non-local pour des séries chronologiques d'images SAR/PolSAR

Le filtre temporel non local donné par l'équation (7.1) vise à éliminer le chatoiement tout en conservant les changements, les détails, la texture, etc. La prise en compte de tous les pixels appartenant à une classe de stabilité (et cela même lorsqu'ils sont très éloignés du pixel courant) est justifié par le souci d'"exploiter la redondance pour améliorer les résultats du filtrage.

B.6.1.1 Propriétés du filtre

L'estimateur donné par l'équation (7.1) a certaines propriétés remarquables :

1) c'est l'estimateur du maximum de vraisemblance standard de la valeur moyenne de la classe de stabilité du pixel.

2) cet estimateur limite la dégradation spatiale et temporelle dans les images filtrées car les informations de stabilité/changement sont prises explicitement en compte dans le filtrage.

3) pour une localisation spatiale (i, j), si toute la pile temporelle $(\mathcal{I}_t(i,j))_t$ ne révèle aucun changement, alors la valeur filtrée à la date t : $\hat{\mathcal{I}}_t(i,j)$ est la valeur moyenne temporelle de la pile. À l'inverse, si le pixel $\mathcal{I}_t(i,j)$ est différent de tous les autres pixels de la pile, alors $\hat{\mathcal{I}}_t(i,j) = \mathcal{I}_t(i,j)$. Ceci implique qu'il n'y a pas d'effet négatif du filtrage sur ce pixel.

4) si l'on considère une série temporelle incluant N images SAR non corrélées de 1-vue chacune, le nombre équivalent de vue (ENL) de l'image filtrée $\hat{\mathcal{I}}_t(i,j)$ est variable entre [1, N] en fonction de la dynamicité de la zone considérée.

B.6.2 Résultats du filtrage multitemporel

B.6.2.1 Avec des séries temporelles d'images SAR monocomposantes

Résultats du filtrage

Pour les régions homogènes, qui sont ici de grandes surfaces couvertes de végétation, les figures 7.1 (a) et (b) montrent que le filtrage est très performant. La CDM2 détecte plus de pixels stables que la CDM1. Les profils des séries temporelles filtrées en utilisant les CDM1 et CDM2 sont donnés à la figure 7.1 (c). Ces profiles sont très corrélés à ceux de la série d'origine, mais la dynamique des amplitudes des pixels est réduite dans le résultat du filtrage : le bruit de chatoiement est donc réduit de manière significative.

Dans le cas d'une cible isolée comme une voiture dans le parking, il y a une seule date (une image) dans laquelle elle est visible. Le pixel correspondant à la position de la voiture dans le parking, à cette date, est complètement différent des autres pixels de la pile. Après le filtrage, la valeur du pixel associé à cette voiture est préservée, comme illustré sur la figure 7.2.

Dans la figure 7.3, la réduction du chatoiement dans l'image filtrée nous permet de voir clairement les détails du parking avec les emplacements occupés par les voitures (ce qui n'est pas le cas si l'on regarde la série temporelle originale).

La figure 7.4 révèle une autre qualité de ce filtre : il élimine du bruit de chatoiement dans les zones inchangées mais sans altérer les informations de déplacement du glacier. Le filtrage réduit le chatoiement dans la zone rocheuse stable, alors que dans la zone du glacier, les textures originales et filtrées ont l'air tout à fait similaire.

Évaluation de la performance du filtrage

La performance d'un filtre multitemporel est évaluée par la réduction du bruit, la préservation des informations spatiales (texture, bord, taille, etc.) et des informations temporelles (changement).

Les histogrammes de nombre de voisins temporels issus des CDMs sur différentes régions caractéristiques dans la figure 7.5 illustrent que le filtre proposé préserve bien les changements.

Pour évaluer quantitativement la réduction du chatoiement et la préservation des informations spatiales, le filtre proposé est comparé à une autre approche de filtrage multitemporel proposée par Quegan et al. [Quegan *et al.* 2000], en employant deux métriques d'évaluation de la qualité d'image :

- le nombre équivalent de vue (ENL, sur une zone homogène: plus il est grand plus le bruit est réduit),
- une mesure structurelle de qualité établie sans image référence (BRISQUE) [Mittal *et al.* 2012], qui quantifie les distorsions sur les structures de l'image. Cette mesure a une valeur comprise entre 0 et 100 (0 représente la meilleure qualité).

Le tableau 7.1 présente les indices d'ENL et de BRISQUE obtenus pour les séries temporelles filtrées par le filtre de Quegan (QF) et le filtre à base de CDM (CDMF). Les ENLs de la série CDMF sont beaucoup plus grands que ceux de la série originale. Ils sont également plus importants que ceux de la série filtrée QF. Les indices de BRISQUE de la série CDMF sont également meilleurs que ceux de la série QF.

B.6.2.2 Avec des séries temporelles d'images SAR multicomposantes

Résultats du filtrage

Les données RADARSAT 2 sont utilisées à des fins de comparaisons avec deux filtres spatiaux adaptatifs: le filtre de Lee raffiné [Lee *et al.* 1999] et l'IDAN [Vasile *et al.* 2006]

Comme dans le cas de la série monocomposante, la figure 7.6 (a) montre que le filtre CDMF diminue significativement le bruit de chatoiement, tandis que les deux filtres spatiaux semblent lisser les transitions. Le profil d'une cible isolée (Figure 7.6 (b)) montre que, après le filtrage, la valeur du pixel où le changement est apparu est préservée par CDMF. Dans les zone de glaciers, où la surface se déplace, seulement quelques échantillons sont détectés comme inchangés (Figure 5.14 (b)), donc la dynamique temporelle est préservée après filtrage CDMF.

Les images filtrées données à la figure 7.7 illustrent que la méthode proposée permet de réduire de façon significative le chatoiement tout en préservant les caractéristiques de détail des images originales. Une comparaison visuelle avec le filtre d'IDAN (Figure 7.7 (b)) et le filtre de Lee raffiné (Figure 7.7 (c)) montre que ces derniers filtres produisent des effets de flou, alors que les images filtrées à base de CDMF (Figure 7.7 (d)) mettent en évidence des transitions nettes, ainsi que la préservation des textures.

Évaluation de la performance du filtrage

Le tableau 7.2 fournit l'évaluation quantitative des performances CDMF, Lee raffiné et IDAN. Le critère ENL est utilisé pour évaluer la réduction du bruit. La préservation de texture est évaluée par le modèle de BRISQUE sur les images RVB formées par les trois images d'amplitudes dans la base de Pauli. Selon les indices ENLs, nous pouvons observer que le niveau de filtrage des deux filtres spatiaux varie sur chaque image tandis que les résultats de CDMF sont tout à fait stables le long de la série temporelle. Mais la valeur moyenne d'ENL du filtre CDMF est légèrement inférieure à celle obtenue avec les deux filtres spatiaux, du fait du filtrage moins agressif CDMF sur les bords et transitions. D'autre part, CDMF conduit, comme nous l'avons vu précédemment, à de bonnes performances selon l'index BRISQUE.

B.7 Conclusions and perspectives

B.7.1 Contributions de la thèse

Dans cette thèse, nous nous sommes concentrés sur l'analyse des changements, le suivi de la dynamique et le filtrage multitemporel à partir des séries chronologiques d'images SAR/PolSAR. Les principales contributions de nos travaux sont les suivantes :

- Nous avons proposé un cadre méthodologique pour l'analyse de changements dans les séries temporelles d'images SAR. Ce cadre est basée sur une matrice multidate de détection de changements (CDM) nécessitant des attributs statistiques et une mesure de similarité entre ces attributs. Ce cadre peut être utilisé avec :

  - différents attributs statistiques (moyennes, covariances, lois de probabilités, etc.),
  - différentes mesures de similarité (coefficient de variation, divergence de Kullback-Libler, etc.),
  - différents types d'images (données SAR en amplitude/intensité, polarisation duale ou quadruple, etc).

  Ce cadre fournit des informations pertinentes qui ont été exploitées pour résoudre différentes tâches : la détection de changements multitemporels, l'analyse de dynamicité et le filtrage multitemporel.

- Nous avons démontré les potentiels de l'approche proposé son application sur deux sites hétérogènes d'étude : Chamonix Mont-Blanc, France et le volcan Merapi, Indonésie, avec différents types de changements et quatre ensembles de données monocomposantes et multicomposantes de moyenne à haute et très haute résolution :

  - [site de Chamonix Mont-Blanc - 3 séries temporelles] 11 images descendantes Sentinel-1 VV et dual-pol VV+HV, 7 images descendantes RADARSAT-2 quad-pol, 25 images ascendantes d'amplitude HH TerraSAR-X (problématiques de suivi de l'évolution de la surface des glaciers),
  - [site du volcan Merapi - 1 série temporelle] 11 images ascendantes ALOS-PALSAR dual-pol acquises pendant une période comprenant l'éruption volcanique de 2010.

  Les résultats expérimentaux obtenus ont montré la pertinence de la méthode proposée pour :

  - détecter de petits objets (voiture sur le parking d'Argentière),
  - identifier des zones instables (chutes de séracs sur le glacier d'Argentière),
  - caractériser la dynamique de glaciers (Argentière et Mer de Glace),
  - établir les cartes de changements après éruption volcanique (Mérapi).

B.7.2 Perspectives

Les travaux présentés dans cette thèse ouvrent plusieurs perspectives pour améliorer les résultats obtenus, ainsi que pour étendre le cadre CDM à d'autres contexte d'analyse :

- Déterminer une méthode automatique de seuillage, qui soit robuste à la nature de la donnée, pour permettre une simplification du choix du seuil. On peut à cet effet citer des travaux récents sur le comportement asymptotique des mesures de similarité, voir [Salicru *et al.* 1994] et [Frery *et al.* 2014], travaux qui sont de nature à permettre le choix d'un seuil robuste. En effet, les 3 techniques de seuillage utilisées dans la thèse (seuil adaptatif pour le test de CV, seuils KI et empiriques pour la KL et la distance de Wishart) ont montré des limitations en pratique : ces méthodes de seuillage ne sont pas universelles au sens où elles sont très sensibles au type de données (taux important de fausses alarmes en général, surtout le seuil KI), en plus de présenter des coûts calculatoires élevés (approches empirique).

- Prendre en compte des stratégies de fusion avancée d'informations de changement dans la construction des CDMs, nous pouvons citer à cet effet la théorie d'évidence de Dezert-Smarandache (DSmT) [Smarandache & Dezert 2004] ou de Dempster-Shafer (DST) [Shafer 1976].

- Généraliser l'utilisation de la transformation d'ondelettes pour des applications où il est utile de discriminer différents types de changements.

- Trouver la (les) mesure(s) de similarité(s) appropriée(s) pour les mesures et suivi de déplacement volumiques à partir des futures données InSAR Sentinel et des données multitemporelles multisources (radar et radar ou radar et optique).

Bibliography

[Ai *et al.* 2010] J. Ai, X. Qi, W. Yu and Y. Deng. *Algorithm Based on 2-D Joint Log-Normal Distribution in SAR Images.* IEEE Geosci. Remote Sens. Lett., vol. 7, no.4, pages 806–810, 2010. (Cited on page 32).

[AirbusDS 2014a] AirbusDS. *TerraSAR-X Image Product Guide - Basic and Enhanced Radar Satellite Imagery.* Airbus Defence and Space - Geo-Intelligence ProgrammeLine, 2014. (Cited on page 45).

[AirbusDS 2014b] AirbusDS. *Radiometric calibration of TerraSAR-X data: Beta Naught and Sigma Naught Coefficient Calculation.* Rapport technique, Airbus Defence and Space, March, 2014. (Cited on page 55).

[Akaike 1974] H. Akaike. *A new look at the statistical model identification.* IEEE Trans. Automatic Control, vol. 19, no. 6, pages 716–723, 1974. (Cited on page 14).

[Akbari *et al.* 2014] V. Akbari, A. P. Doulgeris and T. Eltoft. *Monitoring Glacier Changes Using Multitemporal Multipolarization SAR Images.* IEEE Trans. Geosci. Remote Sens., vol. 52, no. 6, pages 3729–3741, 2014. (Cited on page 26).

[Alonso-Gonzalez *et al.* 2012] A. Alonso-Gonzalez, C. Lopez-Martinez and P. Salembier. *Filtering and Segmentation of Polarimetric SAR Data Based on Binary Partition Trees.* IEEE Trans. Geosci. Remote Sens., vol. 50, no. 2, pages 593–605, 2012. (Cited on page 30).

[Amitrano *et al.* 2015] D. Amitrano, F. Ciervo, P. Di Bianco, G. Di Martino, A. Iodice, F. Mitidieri, D. Riccio, G. Ruello, M. N.Papa and Y. Koussoube. *Monitoring Soil Erosion and Reservoir Sedimentation in Semi-arid Region Through Remote Sensed SAR Data: A Case Study in Yatenga Region, Burkina Faso.* Engineering Geology for Society and Territory, Springer link, vol. 3, pages 539–542, 2015. (Cited on page 26).

[Anfinsen & Eltoft 2011] S. N. Anfinsen and T. Eltoft. *Application of the matrix-variate Mellin transform to analysis of polarimetric radar images.* IEEE Trans. Geosci. Remote Sens., vol. 49, no.6, pages 2281–2295, 2011. (Cited on pages 22 and 23).

[Arsenault & Levesque 1984] H. H. Arsenault and M. Levesque. *Combined homomorphic and local statistics processing for restoration of images degraded by signal-dependent noise.* Appl. Opt., vol. 23n no. 6, pages 845–850, 1984. (Cited on page 28).

[Atto & Berthoumieu 2012] A. M. Atto and Y. Berthoumieu. *Wavelet packets of nonstationary random processes: Contributing factors for stationary and decorrelation.* IEEE Trans. Infor. Theory, vol. 58, no. 1, 2012. (Cited on page 33).

[Atto *et al.* 2012] A. M. Atto, G. Mercier, T. T. Le and E. Trouve. *Vector and matrix LP norms in polarimetric radar filtering.* in Proc. IGARSS Munich, Germany, pages 1441–1444, 2012. (Cited on page 28).

[Atto *et al.* 2013] A. M. Atto, E. Trouve, Y. Berthoumieu and G. Mercier. *Multidate divergence matrices for the analysis of SAR image time series.* IEEE Trans. Geosci. Remote Sens., vol. 51, no. 4, pages 1922–1938, 2013. (Cited on pages 33, 35, 37, 65 and 122).

[Baldassarre *et al.* 2011] G. Di Baldassarre, G. Schumann, L. Brandimarte and P. Bates. *Timely Low Resolution SAR Imagery To Support Floodplain Modelling: a Case Study Review.* Surveys in Geophysics, vol. 32, no. 3, pages 255–269, 2011. (Cited on page 64).

[Bamler & Hartl 1998] R. Bamler and P. Hartl. *Synthetic aperture radar interferometry.* Inverse Problems, vol. 14, pages 1–54, 1998. (Cited on pages 10 and 11).

[Bamler 2000] R. Bamler. *Principles of Synthetic aperture radar.* Surveys in Geophysics, vol. 21, pages 147–157, 2000. (Cited on page 10).

[Bazi *et al.* 2005] Y. Bazi, L. Bruzzone and F. M. Melgani. *An unsupervised approach based on the generalized gaussian model to automatic change detection in multitemporal SAR images.* IEEE Trans. Geosci. Remote Sens., vol. 43, no. 4, pages 874–887, 2005. (Cited on pages 31, 31 and 32).

[Berthier & Vincent 2012] E. Berthier and V. Vincent. *Relative contribution of surface mass balance and ice flux changes to the accelerated thinn ing of the Mer de Glace (Alps) over 1979-2008.* Journal of Glaciology, vol. 58, no. 209, pages 501–512., 2012. (Cited on page 41).

[Bhattacharyya 1943] A. Bhattacharyya. *On a measure of divergence between two statistical populations defined by their probability distributions.* Bulletin of the Calcutta Mathematical Society, vol. 35, pages 99–109, 1943. (Cited on page 35).

[Bombrun & Beaulieu 2008] L. Bombrun and J.-M Beaulieu. *Fisher distribution for texture modeling of polarimetric SAR data.* IEEE Geosci. Remote Sens. Lett., vol. 5, no.3, pages 512–516, 2008. (Cited on page 23).

[Bombrun *et al.* 2011a] L. Bombrun, S. Anfinsen and O. Harant. *A complete coverage of log-cumulant space in terms of distributions for polarimetric SAR data.* in. Proc. PolInSAR, 2011. (Cited on page 23).

[Bombrun *et al.* 2011b] L. Bombrun, V. Vasile, M. Gay and F. Totir. *Hierarichal segmentation of polarimetric SAR images using heterogeneous clutter models.* IEEE Trans. Geosci. Remote Sens., vol. 49, no.2, pages 726–737, 2011. (Cited on page 23).

[Bouvet *et al.* 2009] A. Bouvet, T. Le Toan and L. D. Nguyen. *Monitoring of the Rice Cropping System in the Mekong Delta Using ENVISAT/ASAR Dual Polarization Data.* IEEE Trans. Geosci. Remote Sens., vol. 47, no. 2, pages 517 – 526, 2009. (Cited on page 26).

[Bovolo & Bruzzone 2005] F. Bovolo and L. Bruzzone. *A detail-preserving scale-driven approach to change detection in multitemporal SAR images.* IEEE Trans. Geosci. Remote Sens., vol. 43, no. 12, pages 2963–2972, 2005. (Cited on page 33).

[Bovolo & Bruzzone 2007] F. Bovolo and L. Bruzzone. *A Split-Based Approach to Unsupervised Change Detection in Large-Size Multitemporal Images: Application to Tsunami-Damage Assessment.* IEEE Trans. Geosci. Remote Sens., vol. 45, no. 6, pages 1658–1670, 2007. (Cited on page 33).

[Bruniquel & Lopes 1997] J. Bruniquel and A. Lopes. *Multi-variate optimal speckle reduction in SAR imagery.* Int. J. Remote Sens., vol. 18, no. 3, pages 603–627, 1997. (Cited on page 28).

[Brunner *et al.* 2010] D. Brunner, G. Lemoine and L. Bruzzone. *Earthquake Damage Assessment of Buildings Using VHR Optical and SAR Imagery.* IEEE Trans. Geosci. Remote Sens, vol. 48, no. 5, pages 2403–2420, 2010. (Cited on page 26).

[Bruzzone *et al.* 2004] L. Bruzzone, M. Marconcini, U. Wegmuller and A. Weismann. *An advanced system for the automatic classification of multi-temporal SAR images.* IEEE Trans. Geosci. Remote Sens., vol. 42, no. 6, pages 1321–1334, 2004. (Cited on page 26).

[Buades *et al.* 2005] A. Buades, B. Coll and L. M. Morel. *A review of image denoising algorithms, with a new one.* SIAM Interdisc. J.: Multiscale Model. Simul., vol. 4, no. 2, pages 490–530, 2005. (Cited on page 27).

[Bujor *et al.* 2004] F. Bujor, E. Trouve, L. Valet, J-M.Nicolas and J-P. Rudant. *Application of Log-Cumulants to the detection of spatiotemporal discontinuities in multitemporal SAR images.* IEEE Trans. Geosci. Remote Sens., vol. 42, no. 10, pages 2073–2084, 2004. (Cited on page 31 and 31).

[Catherine & Andre 2007] B. Catherine and O. Andre. *The use of SAR interferometric coherence images to study sandy desertification in southeast Niger: Preliminary results.* in Proc. Envisat Symposium', Montreux, Switzerland (ESA SP-636), pages 23–27, 2007. (Cited on page 26).

[Champion *et al.* 2014] I. Champion, C. Germain, J. P. Da Costa, A. Alborini and P. Dubois-Fernandez. *Retrieval of Forest Stand Age From SAR Image Texture for Varying Distance and Orientation Values of the Gray Level Co-Occurrence Matrix.* IEEE Geosci. Remote Sens. Lett., vol. 11, no. 1, pages 5–9, 2014. (Cited on page 26).

[Charbonnier *et al.* 2013] S. J. Charbonnier, A. Germa, C. B. Connor, R. Gertisser, K. Preece, J.-C. Komorowski, F. Lavigne, T. Dixon and L. Connor. *Evaluation of the impact of the 2010 pyroclastic density currents at Merapi volcano from high-resolution satellite imagery, field investigations and numerical simulations.* Journal of Volcanology and Geothermal Research, vol. 261, pages 295–315, 2013. (Cited on pages 83 and 128).

[Chen & Sato 2013] S.-W. Chen and M. Sato. *Tsunami damage investigation of built-up areas using multitemporal spaceborne full polarimetric SAR images.* IEEE Trans. Geosci. Remote Sens., vol. 51, no., pages 1985–1997, 2013. (Cited on page 26).

[Ciuc *et al.* 2001] M. Ciuc, Ph. Bolon, E. Trouve, V. Buzuloiu and J-P. Rudant. *Adaptive-neighborhood speckle removal in multitemporal SAR images.* Appl. Opt., vol. 40, no. 32, pages 5954–5966, 2001. (Cited on pages 29, 60 and 95).

[Coifman & Donoho 1995] R. R. Coifman and D. N. Donoho. *Translation invariant denoising.* Lecture notes in statistics, vol. 103, pages 125–150, 1995. (Cited on page 33).

[Colesanti & Wasowski 2006] C. Colesanti and J. Wasowski. *Investigating landslides with space-borne Synthetic Aperture Radar (SAR)interferometry.* Engineer. Geology, vol. 88, pages 173–199, 2006. (Cited on page 26).

[Coltuc *et al.* 2000] D. Coltuc, E. Trouve, F. Bujor, N. Classeau and J. P. Rudant. *Time-space filtering of multitemporal SAR images.* in Proc. IGARSS Honolulu, USA, pages 2909–2911, 2000. (Cited on pages 29, 60 and 95).

[Cozzolino *et al.* 2013] D. Cozzolino, S. Parrilli, G. Scarpa, G. Poggi and L. Verdoliva. *Fast adaptive nonlocal SAR despeckling.* IEEE Geosci. Remote Sens. Lett., 2013. (Cited on page 28).

[Dabboor *et al.* 2013] M. Dabboor, M. J. Collins, V. Karathanassi and A. Braun. *An Unsupervised Classification Approach for Polarimetric SAR Data Based on the Chernoff Distance for Complex Wishart Distribution.* IEEE Trans. Geosci. Remote Sens., vol. 51, no. 7, pages 4200–4213, 2013. (Cited on page 36).

[Datcu *et al.* 1998] M. Datcu, K. Seidel and M. Walessa. *Spatial information retrieval from remote sensing images.* IEEE Trans. Geosci. Remote Sens., vol. 36, pages 1431–1445, 1998. (Cited on page 28 and 28).

[Daubechies 1992] Ingrid Daubechies. Ten lectures on wavelets. Society for Industrial and Applied Mathematics, 1992. (Cited on page 67).

[Deledalle *et al.* 2009] C.-A. Deledalle, L. Denis and F. Tupin. *Iterative weighted maximum likelihood denoising with probabilistic patch-based weights.* IEEE Trans. Geosci. Remote Sens., vol. 18, no. 12, pages 2661–2672, 2009. (Cited on pages 28, 28 and 30).

[Dellepiane & Angiati 2012] S.G. Dellepiane and E. Angiati. *A new method for cross-normalization and multitemporal visualization of SAR images for the detection of flooded areas.* IEEE Trans. Geosci. Remote Sens., vol. 50 , no. 7, pages 2765–2779, 2012. (Cited on page 26).

[DeVore & O'Sullivan 2001] M. D. DeVore and J. A. O'Sullivan. *Statistical Assessment of Model Fit for Synthetic Aperture Radar Data.* in Proc. SPIE, vol. 4382, pages 379–388, 2001. (Cited on page 14).

[Dierking & Skriver 2002] W. Dierking and H. Skriver. *Change detection for thematic mapping by means of airborne multitemporal polarimetric SAR imagery.* IEEE Trans. Geosci. Remote Sens., vol. 40, no. 3, pages 618–636, 2002. (Cited on page 31).

[Elachi & vanZyl 2006] C. Elachi and J. vanZyl. Introduction to the physics and techniques of remote sensing. John Wiley & Sons, Inc., Hoboken, New Jersey, 2006. (Cited on pages 5 and 6).

[Engeset *et al.* 2002] R. V. Engeset, J. Kohler, K. Melvold and B. Lundén. *Change detection and monitoring of glacier mass balance and facies using ERS SAR winter images over Svalbard.* Int. J. Remote Sens., vol. 23, no. 10, pages 2023–2050, 2002. (Cited on page 26).

[ESA 2015] ESA. *Sentinel-1 SAR User Guide (https://sentinel.esa.int/web/sentinel/user-guides/sentinel-1-sar)*, 2015. (Cited on page 53).

[Fallourd 2012] R. Fallourd. *Suivi des glaciers alpins par combinaison d'informations hétérogènes : images SAR Haute Résolution et mesures terrain.* PhD thesis, Université de Savoie, 2012. (Cited on page 56).

[Formont *et al.* 2011] P. Formont, F. Pascal, G. Vasile, J.-P. Ovarlez and L. Ferro-Famil. *Statistical Classification for Heterogeneous Polarimetric SAR Images.* IEEE J. Sel. Topics in Signal Process., vol. 5, no. 3, pages 567–576, 2011. (Cited on page 37).

[Freeman & Durden 1998] A. Freeman and S. L. Durden. *A three-component scattering model for polarimetric SAR data.* IEEE Trans. Geosci. Remote Sens., vol. 36, no. 3, pages 963–973, 1998. (Cited on page 30).

[Freitas *et al.* 2005] C. C. Freitas, A. C. Frery and A. H. Correia. *The polarimetric G distribution for SAR data analysis.* Environmetrics, vol. 16, pages 13–31, 2005. (Cited on page 22).

[Frery *et al.* 1997] A. C. Frery, H.-J. Muller, C. C. F. Yanasse and S. J. S. Sant'Anna. *A model for extremely heterogeneous clutter.* IEEE Trans. Geosci. Remote Sens., vol. 35, no.3, pages 648–659, 1997. (Cited on page 22).

[Frery *et al.* 2014] A. C. Frery, A. D. C. Nascimento and R. J. Cintra. *Analytic Expressions for Stochastic Distances Between Relaxed Complex Wishart Distributions.* IEEE Trans. Geosci. Remote Sens., vol. 52, no. 2, pages 1213–1226, 2014. (Cited on pages 35, 36, 109 and 136).

[Frost *et al.* 1982] V. S. Frost, J. A. Stiles, K. S. Shanmugan and J. C. Holtzman. *A model for radar images and its application to adaptive digital filtering of multiplicative noise.* IEEE Trans. Pattern Anal. Machine Intell, vol. 4, pages 157–165, 1982. (Cited on pages 27 and 28).

[Gar-OnYeh & Qi 2015] A. Gar-OnYeh and Z. Qi. Space-time integration in geography and giscience. Chapter 19: Short-interval monitoring of land use and land cover change using a time series of RADARSAT-2 polarimetric SAR images. Springer Link, 2015. (Cited on page 26 and 26).

[Gomez-Chovaa *et al.* 2006] L. Gomez-Chovaa, D. Fernández-Prietob, J. Calpea, E. Soriaa and G. Camps-Vallsa. *Urban monitoring using multi-temporal SAR and multi-spectral data.* PRRS Patte. Recogni. Lett., vol. 27, no. 4, pages 234–243, 2006. (Cited on page 26).

[Goodman 1963] N. R. Goodman. *Statistical analysis based on a certain multivariate complex Gaussian distribution (an introduction).* The Annals of Mathematical Statistics, vol. 34, pages 152–177, 1963. (Cited on page 21).

[Goodman 1976] J. W. Goodman. *Some fundamental properties of speckle.* J. Opt. Soc. Amer., vol. 53, pages 1145–1149, 1976. (Cited on pages 12 and 21).

[HandBooks] HandBooks. *https://earth.esa.int/handbooks/asar/CNTR5-2.htm.* (Cited on page 6).

[Hillion & Boucher 1988] A. Hillion and J-M. Boucher. *A new non linear filtering algorithm with application to radar images.* in Proc. RADAR-88, pages 177–181, 1988. (Cited on page 28).

[Horgan 1998] G. Horgan. *Wavelets for SAR Image Smoothing.* Photogramm. Engineer. Remote Sens., vol. 64, no. 12, pages 1171–1177, 1998. (Cited on page 32).

[Inglada & Mercier 2007] J. Inglada and G. Mercier. *A new statistical similarity measure for change detection in multitemporal SAR images and its extension*

to multiscale change analysis. IEEE Trans. Geosci. Remote Sens., vol. 45, no. 5, pages 1432–1445, 2007. (Cited on pages 32 and 35).

[Inglada 2003] J. Inglada. *Change detection on SAR images by using a parametric estimation of the Kullback-Leibler.* in Proc. IGARSS, Toulouse France, pages 4104–4106, 2003. (Cited on page 32).

[J-SS 2012] J-SS. *PALSARReference Guide.* Japan Space Systems, 6th édition, 2012. (Cited on page 50).

[Jiao *et al.* 2014] X. Jiao, J. M. Kovacs, J. Shang, H. McNairn, D. Walters, B. Ma and X. Geng. *Object-oriented crop mapping and monitoring using multi-temporal polarimetric RADARSAT-2 data.* ISPRS J. Photogramm. Remote Sens., vol. 96, pages 38–46, 2014. (Cited on page 26).

[Justel *et al.* 1997] A. Justel, D. Penab and R. Zamarc. *A multivariate Kolmogorov-Smirnov test of goodness of fit.* Stat. Probabil. Lett., vol. 35, no. 3, pages 251–259, 1997. (Cited on page 14).

[Kerbaol & Collard 2005] V. Kerbaol and F. Collard. *SAR-Derived coastal and marine applications: from research to operational products.* IEEE Oceanic Engineer., vol. 30, no. 3, pages 472–486, 2005. (Cited on page 26).

[Kersten *et al.* 2005] P. R. Kersten, J. S. Lee and T. L. Ainsworth. *Unsupervised Classification of Polarimetric Synthetic Aperture Radar Images Using Fuzzy Clustering and EM Clustering.* IEEE Trans. Geosci. Remote Sens., vol. 43, no. 3, pages 519–527, 2005. (Cited on page 36).

[Kittler & Illingworth 1986] J. Kittler and J. Illingworth. *Minimum error thresholding.* Patten Recognition, vol. 19, No. 1, pages 41–47, 1986. (Cited on pages 32 and 68).

[Komorowski *et al.* 2013] J.-C. Komorowski, S. Jenkins, P. J. Baxter, A. Picquout, F. Lavigne, S. Charbonnier, R. Gertisser, K. Preece, N. Cholik, A. Budi-Santoso and Surono. *Paroxysmal dome explosion during the Merapi 2010 eruption: Processes and facies relationships of associated high-energy pyroclastic density currents.* Journal of Volcanology and Geothermal Research, vol. 261, pages 260–294, 2013. (Cited on pages 41, 83 and 128).

[Kuan *et al.* 1987] D. T. Kuan, A. A. Sawchuk, T. C. Strand and P. Chavel. *Adaptive restoration of images with speckle.* IEEE Trans. Acoust., Speech and Sign. Process., vol. 35, pages 373–383, 1987. (Cited on pages 27 and 28).

[Kuiper 1960] N. H. Kuiper. *Tests concerning random points on a circle.* in Proc. Koninklijke Nederlandse Akademie van Wetenschappen, Series A, vol. 63, pages 38–47, 1960. (Cited on page 14).

[Kullback & Leibler 1951] S. Kullback and R. A. Leibler. *On Information and Sufficiency*. Ann. Math. Statist., vol. 22, no. 1, pages 79–86, 1951. (Cited on page 34).

[Lardeux *et al.* 2011] C. Lardeux, P.-L. Frison, C. Tison, J.-C. Souyris, B. Stoll, B. Fruneau and J.-P. Rudant. *Classification of Tropical Vegetation Using Multifrequency Partial SAR Polarimetry*. IEEE Geosci. Remote Sens. Lett., vol. 8, no. 1, pages 133–137, 2011. (Cited on page 26).

[Lavalle & Wright 2009] M. Lavalle and T. Wright. *Absolute radiometric and polarimetric calibration of ALOS PALSAR products generated within ADEN*. Rapport technique, Issue 1, Revision 3, 2009. (Cited on page 55).

[Le *et al.* 2013] T. T. Le, A. M. Atto and E. Trouve. *Schatten matrix norm based polarimetric SAR data regularization. Application over Chamonix - Montblanc*. in Proc. PolInSAR, 2013. (Cited on page 28).

[Le *et al.* 2015a] T. T. Le, A. M. Atto and E. Trouve. *Change analysis using multitemporal SENTINEL-1 SAR images*. in Proc. IGARSS Milan, Italy, pages 4145–4148, 2015. (Cited on page 64).

[Le *et al.* 2015b] T. T. Le, A. M. Atto, E. Trouve, A. Solikhin and V. Pinel. *Change detection matrix for multitemporal filtering and change analysis of SAR and PolSAR image time series*. ISPRS J. Photogramm. Remote Sens., vol. 107, pages 64–76, 2015. (Cited on page 26).

[Le-Toan 2007] T. Le-Toan. *Lecture: Advanced Training Course on Land Remote Sensing*, 2007. (Cited on page 10).

[Leberl 1990] F. Leberl. Radargrammetric image processing. Artech House, Norwood, 1990. (Cited on page 12).

[Leblon *et al.* 2002] B. Leblon, E. Ksischke, M. Alexander, M. Doyle and M. Abbott. *Fire Danger Monitoring Using ERS-1 SAR Images in the Case of Northern Boreal Forests*. Natural Hazards, Kluwer Academic Publishers., vol. 27, pages 231–255, 2002. (Cited on page 26).

[Lee & Pottier 2009] J.-S. Lee and E. Pottier. Polarimetric radar imaging. From basics to applications. Taylor and Francis Group, 2009. (Cited on pages 5, 19, 20 and 22).

[Lee *et al.* 1991] J. S. Lee, M. R. Grunes and S. A. Mango. *Speckle reduction in multipolarization and multifrequency SAR imagery*. IEEE Trans. Geosci. Remote Sens., vol. 29, no. 4, pages 535–544, 1991. (Cited on page 30).

[Lee *et al.* 1994a] J. S. Lee, M. R. Grunes and R. Kwok. *Classification of multilook polarimetric SAR imagery based on the complex Wishart distribution*. Int. J. Remote Sens., vol. 15, no. 11, pages 2299–2311, 1994. (Cited on page 36).

[Lee *et al.* 1994b] J. S. Lee, D. L. Schuler, R. H. Lang and K. J. Ranson. *K-distribution for multi-look processed polarimetric SAR imagery.* in Proc. IGARSS Pasadena, CA, vol. 4, pages 2179–2181, Aug. 1994. (Cited on page 22).

[Lee *et al.* 1999] J. S. Lee, M. R. Grunes and G. De Grandi. *Polarimetric SAR speckle filtering and its implication for classification.* IEEE Trans. Geosci. Remote Sens., vol. 37, no. 5, pages 2363–2373, 1999. (Cited on pages 102 and 134).

[Lee *et al.* 2003] J. S. Lee, S. Cloude, K. Papathanassiou and I.H. Woodhouse. *Speckle filtering and coherence estimation of polarimetric SAR interferometric data for forest applications.* IEEE Trans. Geosci. Remote Sens., vol. 41, no. 10, pages 2254–2293, 2003. (Cited on page 28).

[Lee *et al.* 2006] J. S. Lee, M. R. Grunes, D. L. Schuler, E. Pottier and L. Ferro-Famil. *Scattering-model-based speckle filtering of polarimetric SAR data.* IEEE Trans. Geosci. Remote Sens., vol. 44, no. 1, pages 176–187, 2006. (Cited on page 30).

[Lee 1980] J. S. Lee. *Digital image enhancement and filtering by use of local statistics.* IEEE Trans. Pattern Anal. Mechine Intell., vol. 7(2), pages 165–168, 1980. (Cited on pages 27 and 28).

[Lee 1981] J. S. Lee. *Refined filtering of image noise using local statistic.* Compt. Graph. Image Process, vol. 15, pages 380–389, 1981. (Cited on page 27).

[Lee 1983] J. S. Lee. *DigDigi noise smoothing and the sigma filter.* Comput. Graph. Image Process., vol. 24, pages 255–269, 1983. (Cited on page 29).

[Lehtiranta *et al.* 2015] J. Lehtiranta, S. Siiria and J. Karvonen. *Comparing C- and L-band SAR images for sea ice motion estimation.* The Cryosphere, vol. 9, pages 357–366, 2015. (Cited on page 26).

[Li *et al.* 2011] H.-C. Li, W. Hong, Y.-R. Wu and P.-Z. Fan. *On the Empirical-Statistical Modeling of SAR Images With Generalized Gamma Distribution.* IEEE J. Sel. Topics Signal Process., vol. 5, no. 3, pages 386–397, 2011. (Cited on page 14).

[Li *et al.* 2013] G.-T. Li, C.-L. Wang, P.-P. Huang and W.-D. Wu. *SAR image despeckling using a space-domain filter with alterable window.* IEEE Geosci. Remote Sens. Lett., vol. 10, no. 2, pages 263–267, 2013. (Cited on page 28).

[Liu & Zhong 2014] G. Liu and H. Zhong. *Nonlocal Means Filter for Polarimetric SAR Despeckling Based on Discriminative Similarity Measure.* IEEE Geosci. Remote Sens. Lett., vol. 11, no. 2, pages 514–518, 2014. (Cited on page 31).

[Lombardo & Olivier 2001] P. Lombardo and C. J. Olivier. *Maximum likelihood approach to the detection of changes between multitemporal SAR images.* IEEE Proc. Radar, Sonar Navig, vol. 148, no. 4, 2001. (Cited on page 31 and 31).

[Lopes & Sery 1997] A. Lopes and F. Sery. *Optimal speckle reduction for the product model in multilook polarimetric SAR imagery and the Wishart distribution.* IEEE Trans. Geosci. Remote Sens., vol. 35, no. 3, pages 632–647, 1997. (Cited on page 30).

[Lopes *et al.* 1993] A. Lopes, E. Nezry, R. Touzi and H. Laur. *Structure detection and statistical adaptive speckle filtering in SAR images.* Int. J. Remote Sens., vol. 14, no. 9, pages 1735–1758, 1993. (Cited on pages 28, 28 and 34).

[Marin *et al.* 2015] C. Marin, F. Bovolo and L. Bruzzone. *Building Change Detection in Multitemporal Very High Resolution SAR Images.* IEEE Trans. Geosci. Remote Sens., vol. 53, no. 5, pages 2664–2682, 2015. (Cited on pages 33 and 64).

[Massonnet & Feigl 1998] D. Massonnet and K. L. Feigl. *Radar Interferometry and its applications to changes in the Earth's surface.* Rev. Geophys., vol. 36, no. 4, pages 441–500, 1998. (Cited on page 26).

[Massonnet & Souyris 2008] D. Massonnet and J.-C Souyris. Imaging with synthetic aperture radar. EPFL Press, Raleigh, USA, 1st edition, 2008. (Cited on page 5).

[McCandless & Jackson 2004] S. W. McCandless and C. R. Jackson. *Chapter 1: Principles of Synthetic Aperture Radar, SAR Marine User's Manual*, 2004. Note: The "Synthetic Aperture Radar Marine User's Manual," by Christopher R. Jackson and John R. Apel was sponsored by NOAA/NESDIS and published in 2004. (Cited on page 8).

[McCandless 1989] S. W. McCandless. SAR in space - The theory, design, engineering and application of a space-based SAR system. Space based radar handbook. Artech House, 1989. (Cited on page 8).

[MDA 2014] MDA. *RADARSAT-2 Product Description.* MacDonald Dettwiler Associates Ltd., 2014. (Cited on pages xv, 47 and 48).

[Miranda & Meadows 2015] N. Miranda and P. J. Meadows. *Radiometric Calibration of S-1 Level-1 Products Generated by the S-1 IPF.* Technical note, European Space Agency, May 21, 2015. (Cited on page 55).

[Mittal *et al.* 2012] A. Mittal, A. K. Moorthy and A. C. Bovik. *No-reference image quality assessment in the spatial domain.* IEEE Trans. Image Process, vol. 21, no. 12, pages 4695–4708, 2012. (Cited on pages 102 and 133).

[Morio *et al.* 2008] J. Morio, P. Refregier, F. Goudail, P. C. Dubois-Fernandez and X. Dupuis. *Information theory-based approach for contrast analysis in polarimetric and/or interferometric SAR images.* IEEE Trans. Geosci. Remote Sens., vol. 46, no. 8, pages 2196–2185, 2008. (Cited on page 35).

[Morio *et al.* 2009] J. Morio, P. Refregier, F. Goudail, P. C. Dubois-Fernandez and X. Dupuis. *A Characterization of Shannon Entropy and Bhattacharyya Measure of Contrast in Polarimetric and Interferometric SAR Image.* IEEE Proc. Journal, vol. 96, no. 6, pages 1097–1108, 2009. (Cited on page 35).

[Moser & Serpico 2006] G. Moser and S. B. Serpico. *Generalized Minimum-Error Thresholding for Unsupervised Change Detection From SAR Amplitude Imagery.* IEEE Trans. Geosci. Remote Sens., vol. 44, no. 10, pages 2972–2982, 2006. (Cited on pages 31, 31 and 32).

[Nicolas *et al.* 2001] J.-M. Nicolas, F. Tupin and H. Maître. *Smoothing speckled SAR images by using maximum homogeneous region filters: An improved approach.* in Proc. IGARSS Sydney, Australia, vol. III, pages 1503–1505, 2001. (Cited on page 27).

[Nicolas 2002] J.-M. Nicolas. *Introduction aux Statistiques de deuxième espèce : applications des Logs-moments et des Logs-cumulants à l'analyse des lois d'images radar.* Trait. Signal, vol. 19, no. 3, pages 139–167, 2002. (Cited on page 13).

[Novak & Burl 1990] L.M. Novak and M.C. Burl. *Optimal speckle reduction in polarimetric SAR imagery.* IEEE Trans. Aerosp. Electron. Syst., vol. 26, no. 2, pages 293–350, 1990. (Cited on page 30).

[Oliver & Quegan 2004] C. Oliver and S. Quegan. Understanding synthetic aperture radar images. SciTech Publishing, Raleigh, USA, 2004. (Cited on pages 5 and 22).

[Oliver 1984] C. Oliver. *A model for nonrayleigh scattering statistics.* Opt. Acta, vol. 31, no. 6, pages 701–722, 1984. (Cited on page 13).

[Otsu 1979] N. Otsu. *A threshold selection method from gray level histograms.* IEEE Trans. Systems, Man, Cybernetics, vol. 9, no. 1, pages 62–66, 1979. (Cited on page 32).

[Paes *et al.* 2010] R. L. Paes, J. A. Lorenzzetti and D. F. M. Gherardi. *Ship Detection Using TerraSAR-X Images in the Campos Basin (Brazil).* IEEE Geosci. Remote Sens. Lett., vol. 7, no. 3, pages 545–548, 2010. (Cited on page 32).

[Pantze *et al.* 2010] A. Pantze, J. E. S. Fransson and M. Santoro. *Forest change detection from L-band satellite SAR images using iterative histogram matching and thresholding together with data fusion.* in Proc. IGARSS Honolulu, HI, pages 1226–1229, 2010. (Cited on page 26).

[Park *et al.* 1999] J.-M. Park, W. J. Song and W. A. Pearlman. *Speckle filtering of SAR images based on adaptive windowing.* IEE Proc Vis. Image Sign. Process, vol. 146, no. 4, pages 191–197, 1999. (Cited on page 34 and 34).

[Parrilli *et al.* 2012] S. Parrilli, M. Poderico, C. V. Angelino and L. Verdoliva. *A nonlocal SAR image denoising algorithm based on LLMMSE wavelet Shrinkage.* IEEE Trans. Geosci. Remote Sens., vol. 50, no. 2, pages 606–616, 2012. (Cited on page 28).

[Pearson 1931] E. S. Pearson. *Note on Tests for Normality.* Biometrika, vol. 22, no. 3/4, pages 423–424, 1931. (Cited on page 14).

[Petillot 2008] I. Petillot. *Combinaison d'informations hétérogènes: intégration d'images RSO pour la surveillance des glaciers alpins.* PhD thesis, Université de Savoie, 2008. (Cited on page 56).

[Pham 2015] H. T. Pham. *Analyse de "Time Lapse" optiques stéréo et d'images radar satellitaires : application à la mesure du déplacement des glaciers.* PhD thesis, Université Savoie Mont Blanc, 2015. (Cited on page 41).

[Plackett 1983] R. L. Plackett. *Karl Pearson and the Chi-Squared Test.* Int. Stat. Review, vol. 51, no. 1, pages 59–72, 1983. (Cited on page 14).

[Pun 1980] T. Pun. *A new method for grey-level picture thresholding using the entropy of the histogram.* Signal Process., vol. 2, pages 223–237, 1980. (Cited on page 32).

[Qin *et al.* 2013] X. Qin, S. Zhou, H. Zou and G. Gao. *A CFAR Detection Algorithm for Generalized Gamma Distributed Background in High-Resolution SAR Images.* IEEE Geosci. Remote Sens. Lett., vol. 10, no. 4, pages 806–810, 2013. (Cited on page 32).

[Quegan & Yu 2001] S. Quegan and J. J. Yu. *Filtering of multichannel SAR images.* IEEE Trans. Geosci. Remote Sens., vol. 39, no. 11, pages 2373–2379, 2001. (Cited on page 29).

[Quegan *et al.* 2000] S. Quegan, T. Le Toan, J. J. Yu. Jiong, F. Ribbes and N. Floury. *Multitemporal ERS SAR analysis applied to forest mapping.* IEEE Trans. Geosci. Remote Sens., vol. 38 , no. 2, pages 741–753, 2000. (Cited on pages 26, 29, 60, 95, 97 and 133).

[Quin *et al.* 2014] G. Quin, B. Pinel-Puyssegur, J.-M. Nicolas and P. Loreaux. *MIMOSA: An Automatic Change Detection Method for SAR Time Series.* IEEE Trans. Geosci. Remote Sens, vol. 52, no. 9, pages 5349–5363, 2014. (Cited on pages 31, 37 and 122).

[RADARSAT 2004] RADARSAT. *RADARSAT-1 Data Products Specifications.* Rapport technique, RSI-GS-026, Revision 3/0, August 19, 2004. (Cited on page 55).

[Rangayyan *et al.* 1998] R. M. Rangayyan, M. Ciuc and F. Faghih. *Adaptive-neighborhood filtering of images corrupted by signal-dependent noise.* Appl. Opt., vol. 37, no. 20, pages 4477–4487, 1998. (Cited on page 27).

[Refice *et al.* 2014] A. Refice, D. Capolongo, G. Pasquariello, A. D'Addabbo, F. Bovenga, R. Nutricato, F. P. Lovergine and L. Pietranera. *SAR and InSAR for Flood Monitoring: Examples With COSMO-SkyMed Data.* IEEE J. Sel. Topics Appl. Earth Observations Remote Sens., vol. 7, no. 7, pages 2711–2722, 2014. (Cited on page 26).

[Rignot & vanZyl 1993] E. J. M. Rignot and J. J. vanZyl. *Change detection techniques for ERS 1 SAR data.* IEEE Trans. Geosci. Remote Sens., vol. 31, no. 4, pages 896–906, 1993. (Cited on page 31).

[Salicru *et al.* 1994] M. Salicru, D. Morales and M. N. Menendez. *On the application of divergence type measures in testing statistical hypotheses.* J. Multivar. Anal., vol. 51, pages 372–391, 1994. (Cited on pages 109 and 136).

[Schellenberger *et al.* 2012] T. Schellenberger, B. Ventura, M. Zebisch and C. Notarnicola. *Wet snow cover mapping agorithm based on multitemporal COSMO-SkyMed X-band SAR images.* IEEE J. Sel. Topics Appl. Earth Observations Remote Sens., vol. 5, no. 3, pages 1045–1053, 2012. (Cited on page 26).

[Schowengerdt 2007] R. A. Schowengerdt. Chapter 7: Correction and Calibration - Remote Sensing: models and methods for image processing. Amsterdam: Elsevier; Burlington: Academic Press, 3rd édition, 2007. (Cited on page 56).

[Schubert *et al.* 2013] A. Schubert, A. Faes, A. Kaab and E. Meier. *Glacier surface velocity estimation using repeat TerraSAR-X images: Wavelet- vs. correlation-based image matching.* ISPRS J. Photogramm. Remote Sens., vol. 82, pages 49–62, 2013. (Cited on page 26).

[Shafer 1976] G. Shafer. A mathematical theory of evidence. Princeton University Press, 1976. (Cited on pages 110 and 136).

[Smarandache & Dezert 2004] F. Smarandache and J. Dezert. Advances and applications of dsmt for information fusion (collected works). American Research Press, 2004. (Cited on pages 110 and 136).

[Solikhin *et al.* 2014] A. Solikhin, J. C. Thouret, S. C. Liew, A. Gupta, D. S. Sayudi, J. F. Oehler and Z. Kassouk. *High-spatial resolution imagery helps map the deposits of the large (VEI 4) 2010 Merapi Volcano eruption and their impact.* Bulletin of Volcanology, revised and re-submitted September 29, 2014., 2014. (Cited on pages 83 and 128).

[Solikhin *et al.* 2015] A. Solikhin, V. Pinel, J. Vandemeulebrouck, J.-C. Thouret and M. Hendrasto. *Mapping the 2010 Merapi pyroclastic deposits using dual-polarization Synthetic Aperture Radar (SAR) data.* Remote Sens. Environ., vol. 158, pages 180–192, 2015. (Cited on page 41).

[Su *et al.* 2014] X. Su, C. Deledalle, F. Tupin and H. Sun. *Two-Step Multitemporal Nonlocal Means for Synthetic Aperture Radar Images.* IEEE Trans. Geosci. Remote Sens., vol. 52, no. 10, pages 6181–6196, 2014. (Cited on page 30).

[Surono *et al.* 2012] Surono, P. Jousset, J. Pallister, M. Boichu, M. F. Buongiorno, A. Budisantoso, F. Costa, S. Andreastuti, F. Prata, D. Schneider, L. Clarisse, H. Humaida, S. Sumarti, C. Bignami andJ. Griswold, S. Carn, C. Oppenheimer and F. Lavigne. *The 2010 explosive eruption of Java's Merapi volcano - A '100-year' event.* Journal of Volcanology and Geothermal Research., vol. 241–242, pages 121–135, 2012. (Cited on page 41).

[Tison *et al.* 2004] C. Tison, J.-M. Nicolas, F. Tupin and H. Maitre. *A new statistical model for markovian classification of urban areas in high-resolution sar images.* IEEE Trans. Geosci. Remote Sens., vol. 42, no. 10, pages 2046–2057, 2004. (Cited on pages 12 and 13).

[Touzi *et al.* 1988] R. Touzi, A. Lopes and P. Bousquet. *A Statistical and Geometrical Edge Detector for SAR Images.* IEEE Trans. Geosci. Remote Sens., vol. 26, no. 6, pages 764–773, 1988. (Cited on page 31).

[Touzi 2002] R. Touzi. *A review of speckle filtering in the context of estimation theory.* IEEE Trans. Geosci. Remote Sens., vol. 40, no. 11, pages 2392–2404, 2002. (Cited on page 28).

[Trouve *et al.* 2003] E. Trouve, Y. Chambenoit, N. Classeau and Ph. Bolon. *Statistical and Operational Performance Assessment of Multitemporal SAR Image Filtering.* IEEE Trans. Geosci. Remote Sens., vol. 41, no. 11, pages 2519–2530, 2003. (Cited on page 28).

[Trouve 2011] N. Trouve. *Comparaison des outils optique et radar en polarimétrie bistatique.* PhD thesis, École Polytechnique - Palaiseau, 2011. (Cited on page 37).

[Tupin *et al.* 2014] F. Tupin, J.-M. Nicolas and J. Inglada. Imagerie de télédétection. Lavoisier, 2014. (Cited on page 55).

[Vasile *et al.* 2006] G. Vasile, E. Trouve, J. S. Lee and V. Buzuloiu. *Intensity-driven adaptive-neighborhood technique for polarimetric and interferometric SAR parameters estimation.* IEEE Trans. Geosci. Remote Sens., vol. 44, no. 6, pages 1609–1621, 2006. (Cited on pages 27, 28, 30, 102 and 134).

[Vasile *et al.* 2010] G. Vasile, J.-P. Ovarlez, F. Pascal and C. Tison. *Coherency Matrix Estimation of Heterogeneous Clutter in High-Resolution Polarimetric*

SAR Images. IEEE Trans. Geosci. Remote Sens., vol. 48, no. 4, pages 1809–1826, 2010. (Cited on pages 22, 36 and 37).

[Vincent *et al.* 2014] C. Vincent, M. Harter, A. Gilbert, E. Berthier and D. Six. *Future fluctuations of the Mer de Glace (French Alps) assessed using a parameterized model calibrated with past thickness changes*. Annals of Glaciology, vol. 55, no. 66, pages 15–24, 2014. (Cited on page 41).

[Waske & Braun 2009] B. Waske and M. Braun. *Classifier ensembles for land cover mapping using multitemporal SAR imagery*. ISPRS J. Photogramm. Remote Sens., vol. 64, pages 450–457, 2009. (Cited on page 26).

[Wiley 1954] C. Wiley. *Pulsed doppler radar methods and apparatus*. US Patent, vol. 3,196,436, 1954. (Cited on page 8).

[Wu & Maitre 1992] Y. Wu and H. Maitre. *Smoothing speckled synthetic aperture radar images by using maximum homogeneous region filters*. Opt. Eng, vol. 31, no. 8, pages 1782–1792, 1992. (Cited on page 27).

[Yang *et al.* 2015] W. Yang, H. Song, G.-S. Xia and C. Lopez-Martinez. *Dissimilarity measurements for processing ans analyzing PolSAR data: A survey*. in Proc. IGARSS Milan, Italy, pages 1562–1565, 2015. (Cited on page 37).

[Zhong *et al.* 2011] H. Zhong, Y. Li and L. Jiao. *SAR image despeckling using bayesian nonlocal means filter with sigma preselection*. IEEE Geosci. Remote Sens. Lett., vol. 8, no. 4, pages 809–813, 2011. (Cited on page 28).